TESIS DOCTORAL

COMPORTAMIENTO DE GELES DE CARBÓN CON DIFERENTE FÍSICA Y QUÍMICA SUPERFICIAL COMO ELECTRODOS DE SUPERCONDENSADORES Y SOPORTES DE CATALIZADORES DE Pt

Marta B. Dawidziuk

Editor: Editorial de la Universidad de Granada
Autor: Marta B. Dawidziuk
D.L.: GR 776-2012
ISBN: 978-84-694-6674-2

COMPORTAMIENTO DE GELES DE CARBÓN CON DIFERENTE FÍSICA Y QUÍMICA SUPERFICIAL COMO ELECTRODOS DE SUPERCONDENSADORES Y SOPORTES DE CATALIZADORES DE Pt

Por

Marta B. Dawidziuk

Memoria presentada para aspirar la grado de Doctor por la Universidad de Granada

Fdo. Marta B. Dawidziuk

Los Directores de la Tesis

Dr. Carlos Moreno Castilla
Catedrático de Química Inorgánica
de la Universidad de Granada

Dr. Francisco Carrasco Marín
Catedrático de Química Inorgánica
de la Universidad de Granada

Carlos Moreno Castilla y Francisco Carrasco Marín, Catedráticos de Química Inorgánica

CERTIFICAN QUE,

Marta B. Dawidziuk, Licenciada en Ciencias Químicas, ha realizado la Tesis Doctoral titulada "Comportamiento de geles de carbón con diferente física y química superficial como electrodos de supercondensadores y soportes de catalizadores de Pt" en el Departamento de Química Inorgánica de la Facultad de Ciencias para aspirar al grado de Doctor por la Universidad de Granada, reuniendo las condiciones necesarias para ser presentada y defendida ante el tribunal correspondiente.

Y para que conste a los efectos oportunos, en cumplimiento de la legislación vigente, firmamos el presente certificado en Granada, a 8 de junio de 2011.

Dr. Carlos Moreno Castilla
Catedrático de Química Inorgánica
de la Universidad de Granada

Dr. Francisco Carrasco Marín
Catedrático de Química Inorgánica
de la Universidad de Granada

Esta Tesis Doctoral ha sido realizada gracias a la concesión de una beca predoctoral de la Junta de Andalucía.

El trabajo recogido en esta memoria ha sido financiado por los proyectos: “Eliminación de contaminantes en fase acuosa y gaseosa mediante procesos de adsorción y catálisis usando materiales avanzados de carbón” proyecto de Excelencia de la Junta de Andalucía, RNM547 (2006-2009) y “Nuevos aerogeles de carbón como soportes de catalizadores para reacciones de hidrogenación, oxidación de COVs y como electrocatalizadores en pilas de combustible” financiado por el Ministerio de Educación y Ciencia, Fondos FEDER, CTQ2007-61324 (2007-2010).

INDICE

INTRODUCCIÓN

En la presente Memoria se recogen una serie de trabajos llevados a cabo sobre la síntesis y caracterización de geles de carbón para su uso como: i) Electrodos de supercondensadores para el almacenamiento de energía electroquímica; ii) Como soportes de catalizadores de Pt y su uso en las reacciones de hidrogenolisis e isomerización de n-butano.

El trabajo recogido en esta Memoria se enmarca dentro de los proyectos de investigación que se han desarrollado en el Grupo de Investigación en Materiales de Carbón de la Universidad de Granada. Estos proyectos han sido: "Eliminación de contaminantes en fase acuosa y gaseosa mediante procesos de adsorción y catálisis usando materiales avanzados de carbón", proyecto de Excelencia de la Junta de Andalucía, RNM547 (2006-2009), y "Nuevos aerogeles de carbón como soportes de catalizadores para reacciones de hidrogenación, oxidación de COV's y como electrocatalizadores en pilas de combustible", financiado por el Ministerio de Educación y Ciencia, Fondos FEDER, CTQ2007-61324 (2007-2010).

Los Capítulos de esta Memoria están escritos en inglés y constituyen trabajos independientes que se han publicado, están en prensa o se van a enviar a publicar próximamente. Un resumen de estos capítulos se recoge a continuación.

Capítulo I: Características superficiales y capacidad electroquímica de aerogeles de carbón obtenidos a partir de resorcinol y pirocatecol empleando ácidos bórico y oxálico como catalizadores de polimerización.

Los aerogeles de carbón se prepararon por carbonización de aerogeles orgánicos obtenidos mediante la reacción de polimerización de resorcinol y/o pirocatecol con formaldehído empleando ácidos bórico y oxálico como catalizadores de polimerización. Las muestras preparadas se caracterizaron mediante diferentes técnicas con objeto de determinar su composición, química y física superficial, morfología y sus capacidades electroquímicas en medio ácido. El uso de pirocatecol produjo aerogeles de carbón que son micro-mesoporosos, con isotermas de adsorción de N_2 Tipo IV con ciclos de histéresis Tipo H2. El volumen y el tamaño de mesoporos dependió del catalizador ácido utilizado y de la temperatura a la cual el aerogel de carbón se obtuvo. Por el contrario, la muestra preparada con resorcinol y ácido bórico como catalizador fue micro-macroporosa y la que se obtiene con una mezcla de resorcinol-pirocatecol fue micro-mesoporosa pero con mesoporos de mayores dimensiones. La mayor parte del ácido bórico utilizado se eliminó durante el intercambio de agua por acetona en los hidrogeles orgánicos previo a su secado con CO_2 supercrítico. Los aerogeles de carbón preparados con ácido bórico como catalizador de polimerización y carbonizados a 900 °C presentan capacidades comprendidas entre 17 y 24 $\mu F/cm^2$. El boro influyó en la capacidad, ya que provocó un aumento en el contenido de oxígeno. La muestra sintetizada utilizando pirocatecol, formaldehído y ácido oxálico, y sometida a tratamiento térmico a 900 °C presentó la capacidad más alta, 34 $\mu F/cm^2$. Este

Capítulo está en prensa en la revista Carbon, **http://dx.doi.org/10.1016/j.carbon.2011.05.013**

Capítulo II: Comportamiento como electrodos de supercondensadores de geles de carbón con diferente química y física superficial.

En este Capítulo se describe el comportamiento, como supercondensadores, de xerogeles de carbón dopados con nitrógeno en forma de microesferas y aerogeles de carbón con diferentes porosidades y complejos superficiales de oxígeno. La capacidad interfacial de los xerogeles de carbón dopados con nitrógeno disminuyó al incrementar la superficie microporosa determinada mediante adsorción de N_2 a -196 ºC. Por otra parte se encontró una buena correlación entre la capacidad interfacial y la concentración por unidad de superficie de N_{XPS}, obteniéndose la mejor correlación con la concentración específica de funcionalidades tipo piridina. La capacidad gravimétrica disminuyó al aumentar el diámetro de las microesferas de xerogel. La capacidad interfacial de los aerogeles de carbón se incrementó al aumentar el porcentaje de porosidad determinada a partir de la densidad de partícula y la densidad real. La capacidad interfacial presentó una relación lineal con la concentración específica de oxígeno y con las concentraciones específicas de grupos superficiales que evolucionaron como CO y CO_2.

Capítulo III: Influencia de la porosidad del soporte y del contenido en Pt de catalizadores Pt/aerogel de carbón en la dispersión metálica y en la formación de nanoestructuras híbridas Pt-carbón autoensambladas.

Tres aerogeles de carbón con diferente retículo meso-macroporoso se emplearon como soportes de catalizadores de Pt usando como sal precursora $[Pt(NH_3)_4]Cl_2$. Los resultados obtenidos mostraron que el volumen y el tamaño medio de los mesoporos son los parámetros que controlaron el tamaño de las partículas de Pt y su dispersión en catalizadores con un contenido del 2% de Pt. El aerogel de carbón que presentó la porosidad más adecuada para obtener la mayor dipersión se usó para preparar catalizadores con un contenido de hasta el 20% en Pt. El tamaño medio de las partículas de Pt solo se incrementó de 1 a 2 nm lo cual puso de manifiesto la gran importancia de una adecuada mesoporosidad para obtener elevadas dispersiones cuando se emplean elevados contenidos de metal. Los tamaños medios de las partículas metálicas obtenidos mediante microscopía electrónica de transmisión fueron, en todos los casos inferiores, a los determinados mediante quimisorción de hidrógeno dado que las partículas de Pt no se encuentraron totalmente reducidas, como se puso de manifiesto mediante espectroscopía de fotoemisión de rayos-X. Finalmente, la observación mediante microscopía electrónica de transmisón de los catalizadores con contenidos en metal entre 8-20 % antes del pretratamiento mostró la formación de nanoestructuras híbridas Pt-carbón autoensambladas en forma de varillas y alambres. Tras una exhaustiva revisión bibliográfica se puede afirmar que esta es la primera vez que se ha observado este fenómeno en catalizadores Pt/C. Este trabajo está publicado en Carbon con la referencia Carbon, 2009; 47:2679-87.

Capítulo IV: Hidrogenolisis e isomerización de n-butano catalizadas por Pt soportado sobre aerogeles de carbón y carbón activado.

En este trabajo se estudiaron las reacciones de hidrogenolisis e isomerización de n-butano sobre catalizadores de Pt soportados sobre aerogeles de carbón y carbón activado. La frecuencia turnover (TOF) para la hidrogenolisis estuvo influenciada por el soporte. Esto puede deberse al grado de aromatización del soporte o al desarrollo de superficies de Pt con diferentes índices. Las reacciones de hidrogenolisis e isomerización se relacionaron con el tamaño medio de las partículas de Pt soportado en los aerogeles de carbón que fueron carbonizados a 900-950 °C. Por otra parte se observó un efecto de compensación entre la energía de activación y el factor preeexponencial el cual fue común para la hidrogenolisis y la isomerización. Esto indica que ambas reacciones transcurrieron a través del mismo intermedio de reacción, el cual fue el alcano deshidrogenado quimisorbido sobre el catalizador.

CHAPTER I

SURFACE CHARACTERISTICS AND ELECTROCHEMICAL CAPACITANCES OF CARBON AEROGELS OBTAINED FROM RESORCINOL AND PYROCATECHOL USING BORIC AND OXALIC ACIDS AS POLYMERIZATION CATALYSTS

1. ABSTRACT

Carbon aerogels were prepared by carbonizing (at 500–1500 ºC) organic aerogels obtained from the polymerization reaction of resorcinol and/or pyrocatechol with formaldehyde using boric and oxalic acids as polymerization catalysts. Prepared samples were characterized by different techniques to ascertain their composition, surface chemistry, morphology, and surface physics, determining their electrochemical capacitances in acidic medium. The use of pyrocatechol yielded carbon aerogels that were micro-mesoporous, showing Type IV N_2 adsorption isotherms with Type H2 hysteresis cycles. The volume and size of mesopores depended on the acid catalyst used and the temperature at which the carbon aerogel was obtained. Conversely, the sample prepared with resorcinol and boric acid as catalyst was micro-macroporous and that obtained with a resorcinol-pyrocatechol mixture was micro-mesoporous but with large mesopores. Most of the boric acid used was lost during the exchange of water with acetone in the organic hydrogels before their supercritical CO_2 drying. Carbon aerogels obtained at 900 ºC and using boric acid as polymerization catalyst showed a capacitance between 17 and 24 $\mu F/cm^2$. Boron influenced the capacitance because it increased the oxygen content. Sample synthesized using pyrocatechol, formaldehyde, and oxalic acid and heat-treated at 900 ºC had the highest capacitance, 34 $\mu F/cm^2$.

2. INTRODUCTION

Carbon gels are nanostructured materials [1], given that their structure and porous texture can be designed and controlled at nanometer scale. They are produced by carbonization of organic gels prepared by the sol-gel polymerization of phenolic compounds with formaldehyde [2], using either basic or acidic catalysts. The potential benefits of sol-gel processing include the purity, homogeneity, and controlled porosity of the materials obtained.

Besides their well-developed and controlled micro and mesoporosity, carbon gels can be prepared in the form of monoliths, beads, powders, or thin films [3]. These properties make them good materials for applications in adsorption and catalysis and for use as electrodes for energy storage in electric double-layer capacitors (EDLC), among other uses [3-12].

An important feature of these materials is that they can be readily doped with different metallic and non-metallic elements, which can change their adsorptive and catalytic properties, electrical conductivity, and capacitance. One doping method is to add the dopant to the initial mixture, so that it remains trapped in the carbon gel matrix after gelation and carbonization. The preparation of different doped carbon gels has been reported in the literature [3].

Carbon aerogels in the present work were prepared by the carbonization of polymers formed between resorcinol and pyrocatechol with formaldehyde, using boric and oxalic acids as polymerization catalysts, with the aim of studying the

changes introduced into their morphology, surface chemistry, and physics, and determining their electrochemical performance as electrode materials in EDLC.

Most carbon gels reported in the literature were prepared with resorcinol as carbon source, and pyrocatechol has been little used. It is well known [13] that boric acid can be readily chelated by organic compounds containing neighboring hydroxyl groups, which also enhances its acidity. Accordingly, the use of pyrocatechol instead of resorcinol can introduce differences in the gelation process, resulting in variations in the surface characteristics of the final carbon gels obtained.

In addition, the use of boric acid as polymerization catalyst could enable doping with boron in the final carbon gel. This could be of interest, because boron-doped carbon gels can exhibit improved catalytic [14,15] and electrochemical energy storage properties [16].

3. EXPERIMENTAL

3.1. Sample preparation

Monolithic organic aerogels were prepared by the sol-gel polymerization reaction of phenolic compounds with formaldehyde (F) in water (W) using boric or oxalic acids as catalysts (C), according to the recipes in Table 1. The phenolic compounds (PC) used were resorcinol, pyrocatechol, and a mixture of both. Molar ratios were PC/F = 0.5, PC/W = 0.075, and PC/C = 16.2, 5.3 and 560. Mixtures were stirred to obtain a homogeneous solution that was cast into glass

moulds (45 cm length x 0.5 cm i.d.). Glass moulds were sealed and the mixture was cured for five days at different temperatures up to 80 ºC.

Table 1.- Organic aerogel recipes (Formaldehyde, 0.224 mol; Total water, 26.7 mL)

Sample	Resorcinol (mol)	Pyrocatechol (mol)	Catalyst precursor (mol)	Initial pH	Color after curing
R1	0.112	-	H_3BO_3 6.9×10^{-3}	3.3	Deep orange
RP1	0.100	0.012	H_3BO_3 6.9×10^{-3}	3.0	Deep brown
P1	-	0.112	H_3BO_3 6.9×10^{-3}	1.6	Black
P3	-	0.112	H_3BO_3 2.1×10^{-2}	1.5	Black
POX	-	0.112	H_3BO_3 2.0×10^{-4}	2.1	Deep orange

After the curing cycle, the gel rods were cut into 5 mm pellets and placed in acetone to exchange water. Impregnated acetone pellets were dried with supercritical CO_2 using a model CPD7501 critical point dryer from VG Microtech. Pyrolysis was carried out in N_2 flow at 100 cm^3/min, heating to 500 or 900 ºC at a heating rate of 1.5 ºC/min and soaking time of 5 h. Carbon aerogels so obtained

will be designated henceforth by appending the heat treatment temperature to the names of the organic aerogels that appear in Table 1.

Portions of carbon aerogels P3-900 and POX-900 were further heat treated to 1500º C in Ar flow (60 cm^3/min). For this purpose, both samples were heated to the final temperature with the following program: up to 400 ºC at 2 ºC/min, from 400 to 900 ºC at 10 ºC/min, and from 900 to 1500 ºC at 2 ºC/min, holding this temperature for 2 h. Then, the samples were cooled to 400 ºC at 5 ºC/min and from 400 to 25 ºC at 2 ºC/min. Some of these steps were imposed for a correct use of the furnace. Samples treated in this way will be designated P3-1500 and POX-1500, respectively.

3.2. Characterization methods

A battery of techniques was used to determine the composition and surface chemistry, morphology, and surface physics. Composition and surface chemistry was studied by nuclear reaction analysis (NRA), X-ray photoelectron spectroscopy (XPS), and temperature programmed desorption (TPD) coupled with mass spectrometry. Morphology was studied by scanning electron microscopy (SEM). Surface physics was studied by N_2 and CO_2 adsorption (at -196 and 0 ºC, respectively), mercury porosimetry, and immersion calorimetry.

NRA was used to measure the B content of carbon aerogels, bombarding samples with 717 keV protons from a 3 MeV Tandem Pelletron accelerator at the Spanish National Accelerator Center (CNA, Seville, Spain). Scattered particles

were detected with a PIPS type detector placed at 150º to the beam direction in 300 mm^2 IBM geometry without filter. The nuclear reaction $^{11}B(p,\alpha)2\alpha$ was used for boron analysis.

XPS was performed with an Escalab 200R system (VG Scientific Co.) equipped with MgKα x-ray source (hγ = 1253.6 eV) and hemispherical electron analyzer. Samples were evacuated at high vacuum and introduced into the analysis chamber. A base pressure of 10-9 mbar was maintained during data acquisition. Survey and multi-region spectra were recorded at C1s, O1s, and B1s photoelectron peaks. Each spectral region of photoelectron interest was scanned several times to obtain good signal-to-noise ratios. The spectra obtained after background signal correction were fitted to Lorentzian and Gaussian curves, using the C_{1s} peak at 284.6 eV as internal standard, in order to obtain the number of components, position of the peaks, and peak areas.

TPD was carried out by heating the samples to 1000 ºC at 50 ºC/min and analyzing the CO and CO_2 evolved by means of a model Prisma mass spectrometer from Pfeiffer. The oxygen content, O_{TPD}, was calculated from the amount of CO and CO_2. SEM was done with a Zeiss DSM950 (30kV) microscope. Adsorption isotherms were measured with an Autosorb 1 from Quantachrome after outgassing samples overnight at 110 ºC under high vacuum (10^{-6} mbar). N_2 adsorption isotherms were analyzed by BET equation, from which the surface area, S_{BET}, was obtained. The volume of nitrogen adsorbed at a relative pressure of 0.95, $V_{0.95}$, was also obtained from these isotherms, which, according to Gurvitch's rule, is equivalent to the addition of the micro- and mesopore volumes.

The Barrett-Joyner-Halenda (BJH) method was applied to the adsorption branch of Type IV N_2 adsorption-desorption isotherms in the IUPAC classification [17] in order to determine mesopore size distributions. The mean size and volume and surface area of mesopores, d_{BJH}, V_{BJH} and S_{BJH}, respectively, were obtained from these distributions. The Dubinin-Radushkevich (DR) equation was applied to N_2 and CO_2 adsorption isotherms at -196 and 0 ºC, respectively, yielding the micropore volume, W_0, and the characteristic adsorption energy, E_0. The mean micropore width, L_0, was obtained by applying the Stoeckli equation (1) [18].

$$L_0\,(\mathrm{nm}) = \frac{10.8}{E_0 - 11.4\,(\mathrm{kJ/mol})} \qquad (1)$$

This equation is valid for E_0 values between 42 and 20 kJ/mol, which correspond to pore widths between 0.35 and 1.3 nm. The micropore surface area, S_{mic}, was calculated by the well-known equation (2) given by Stoeckli [18], which is valid for slit-shaped micropores.

$$S_{mic}\,(\mathrm{m^2/g}) = \frac{2000 \times W_0\,(\mathrm{cm^3/g})}{L_0\,(\mathrm{nm})} \qquad (2)$$

N_2-obtained W_0 and L_0 values were used instead of those obtained with CO_2, because the former yield the total volume of micropores and their mean width, respectively, if there are no micropore constrictions at their entrance or very narrow micropores [4].

Some samples were also studied by mercury porosimetry up to a pressure of 4200 kg/cm^2 using Quantachrome Autoscan 60 equipment, yielding the following parameters: the volume of pores with a diameter between 3.7 and 50 nm, V_{meso},

referred to as mesopore volume (note that the mesopore volume range is classically defined as 2 - 50 nm) [19]; the volume of pores with a diameter >50 nm, macropore volume, Vmacro; mean meso- and macropore size, dP; and apparent particle density, ρ.

Immersion enthalpy into benzene, $\Delta_i H(C_6H_6)$, was determined by using a model C80-D Setaram calorimeter. Samples were previously outgassed overnight under a dynamic vacuum of 10^{-6} mbar at 120 ºC. Measurements were carried out at 30 ºC and at least twice for each sample. The enthalpy of immersion into benzene was converted into a surface area value following the method proposed by Denoyel et al. [20] and used by other authors [21-23]. A surface area value, S_{imm}, was obtained by taking account of the enthalpy of immersion into benzene of a non-porous graphitized carbon black [20], -0.114 J/m^2.

3.3. Electrochemical measurements

Electrochemical measurements were carried out in a model VPM3 multichannel potentiostat from Biologic at room temperatures using a 1 M H_2SO_4 solution as electrolyte. Working electrode was prepared by mixing the finely ground carbon gel, acetylene black (Denki Kagaku Kogyo Co., Japan), and binder (polytetrafluoroethylene, PTFE) at a weight ratio of 80:10:10. The mixture so obtained was pasted on graphite paper. The as-prepared electrodes were investigated with a typical three-electrode configuration using Ag/AgCl (SCE) as reference electrode and a Pt wire as counter electrode.

Cyclic voltammograms were obtained within the potential window of -0.3 to 0.6 V at scan rates of 0.5, 1 and 5 mV/s. The gravimetric capacitance of carbon gels, C_{CV} (F/g), was obtained from these curves by equation (3)

$$C_{CV} = \frac{\sum |I| \Delta t}{2m \times \Delta V} \qquad (3)$$

where $\Sigma |I| \Delta t$ is the area of the current (A) against time (s) curve, m the mass of active material in the electrode (g), and ΔV the voltage window (V). Chronopotentiograms were performed under a constant current density of 100 mA/g in a voltage range of 0-0.7 V. Gravimetric capacitance from these measurements, C_{CP} (F/g) was obtained by equation (4).

$$C_{CP} = \frac{I_d \times \Delta t}{m \times \Delta V} \qquad (4)$$

where I_d is the discharge current (A), Δt the discharge time (s), and ΔV the voltage (V).

4. RESULTS AND DISCUSSION

4.1. Composition and surface chemistry

Boric and oxalic acids were used as acid catalysts for the polymerization reaction of the phenolic compounds with formaldehyde. Boric acid is a weak monobasic acid [13] that acts exclusively by hydroxyl-ion acceptance rather than

proton donation. In addition, it is chelated with polyhydric alcohols, which enhances its acidity [13].

Most carbon gel synthesis procedures in the literature [24-26] use the polymerization reaction of resorcinol with formaldehyde either in basic or acid medium, while there are scant data on the use of pyrocatechol. The position of the two hydroxyl groups in the orto isomer enables the chelation of boric acid, which is not feasible with the meta isomer.

Results given in Table 1 show that the initial pH values of samples P1 and P3 were much lower than those of samples R1 and RP1, indicating that boric acid chelation took place when pyrocatechol was used. The low initial pHs of samples P1 and P3 also influenced the gelation time, which was shorter than for the other samples, with effects on the final colour of the organic gel after curing.

Weight loss (WL) during carbonization is given in Table 2. The WL obtained after heating at 500 and 900 ºC was 36-40% and 44-50%, respectively. Hence, the highest WL was produced after heating at 500 ºC, as previously reported [27]. The WL of samples heated at 1500 ºC was low because these samples were previously heated at 900 ºC. Pellet diameter of organic aerogels (see Table 2) prepared with pyrocatechol, samples P1, P3 and POX, was smaller than that of aerogels prepared with resorcinol, samples R1 and RP1. The aerogels underwent shrinkage during heat treatments, as evidenced by their reduced diameter. This shrinkage increased with higher temperature.

The B content of samples is displayed in Table 3. B_{NRA} and B_{XPS} data can be taken as the total and surface B content, respectively, because the depth of NRA analysis is 3-4 μm. Results show that $B_{NRA} < B_{XPS}$ in samples obtained at 500 ºC, indicating a surface segregation of B in these samples. However, B_{NRA} was similar or very close to B_{XPS} in most samples obtained at 900 ºC, indicating a B redistribution with increasing temperature that leads to a more homogeneous B distribution.

Table 2.- Weight loss and pellet diameter after heating the organic aerogels at different temperatures

Sample	Weight loss (%)	Diameter (mm)	Sample	Weight loss (%)	Diameter (mm)
R1	---	4.2	P3	---	3.9
R1-500	36	3.6	P3-500	36	3.3
R1-900	50	3.3	P3-900	44	3.1
RP	---	4.3	P3-1500	5*	3.1
RP1-500	37	3.8	POX	---	3.6
RP1-900	48	3.3	POX-500	40	3.1
P1	---	4.0	POX-900	47	2.9
P1-500	36	3.3	POX-1500	4*	2.8
P1-900	44	3.1	---	---	---

* This weight loss corresponds to samples heated to 1500º C that were previously heated to 900º C.

The total B content of the B-doped carbon aerogels was much lower than expected given the amount of boric acid in their recipes (around 1 and 3% for

$6.9x10^{-3}$ and $2.1x10^{-2}$ H_3BO_3 moles, respectively). Therefore, part of the boric acid was lost during preparation of the carbon aerogels, and it was found that this occurred during the exchange of water with acetone in the hydrogels before their supercritical drying.

Table 3.- Amounts of CO and CO_2 evolved up to 1000º C from TPD and oxygen and boron contents (% mass) from TPD, XPS and NRA

Sample	CO (µmol/g)	CO_2 (µmol/g)	O_{TPD} (%)	O_{XPS} (%)	B_{XPS} (%)	B_{NRA} (%)
R1	nd	nd	nd	25.50	0.13	nd
R1-500	4.06	0.85	9.23	14.32	0.20	0.07
R1-900	0.48	0.16	1.28	8.00	0.20	0.15
RP1	nd	nd	nd	29.27	0.10	nd
RP1-500	3.59	0.91	8.66	10.46	0.14	0.09
RP1-900	0.47	0.12	1.12	4.18	0.11	0.21
P1	nd	nd	nd	29.55	0.14	nd
P1-500	3.61	1.79	9.48	11.52	0.18	0.08
P1-900	0.74	0.29	2.11	5.60	0.20	0.21
P3	nd	nd	nd	27.48	0.23	nd
P3-500	3.63	2.32	11.48	13.23	0.33	0.22
P3-900	0.80	0.40	2.56	6.75	0.32	0.30
P3-1500	0.02	0.04	0.18	6.17	0.86	nd
POX-500	3.69	1.41	10.42	nd	nil	nil
POX-900	0.27	0.24	1.18	nd	nil	nil
POX-1500	0.00	0.04	0.13	nd	nil	nil

nd: not determined

TPDs of samples are displayed in Appendix I, Figures A.I.1 to A.I.5. The amounts of CO and CO_2 evolved up to 1000 ºC are compiled in Table 3. Before analyzing these results, it should be taken into account that these samples, except for the POX series, should not have surface oxygen complexes evolving as CO_2 because the ingredients used to prepare the organic aerogels do not contain any group that gives rise to carboxyl or lactone groups (responsible for CO_2 evolution) during the polymerization and subsequent carbonization. Therefore, these groups were fixed on the carbon surface after the exposure to air of the newly prepared carbonized samples.

Samples heat treated to 500 and 900 ºC should not have any CO_2-evolving groups below these temperatures but this was not the case, as shown in Figures A.I.1 to A.I.5. Hence, CO_2-evolving groups that appear below 500 and 900 ºC derive, as above, from the oxygen chemisorbed after exposing these heat-treated samples to the atmosphere. The same is true, although to a lesser extent, for CO-evolving groups that appear below 500 and 900 ºC in heat-treated samples.

It is noteworthy that the samples heat-treated at 1500 ºC, P3-1500, and POX-1500, show practically no CO_2- or CO-evolving groups. This indicates that the surface active sites created in heat-treated samples at lower temperatures were eliminated at this annealing temperature, so that the samples did not chemisorb oxygen after air exposure.

The CO_2-evolving profiles were fairly similar among samples, with two maxima in the regions of 300-400 ºC and 550-600 ºC. The maximum at lower temperatures could correspond to carboxyl groups and the maximum at higher

temperatures to lactone or anhydride groups [28]. The CO_2-evolving profiles of carbon aerogels obtained at 900 ºC only showed the maximum at lower temperatures.

The CO-evolving profiles of carbon aerogels obtained at 500 ºC show a clear maximum between 650 and 700 ºC, which could correspond to ether and/or phenol groups. This would be in agreement with the groups present in the ingredients and those formed during their polymerization. Samples obtained at 900 ºC show a wide maximum between 850-950 ºC in their CO-evolving profiles, likely due to quinone groups [28].

The total oxygen content, O_{TPD}, decreased when heat-treatment temperature increased, and its value was always smaller than the XPS-determined oxygen content, O_{XPS} (see Table 3). O_{XPS} gives the surface oxygen content, because the depth of XPS analysis is around 2-3 nm. Differences between O_{TPD} and O_{XPS} are found in most carbon materials, because exposure to air produces preferential oxygen chemisorption on the more external surface.

The increase in B_{XPS} content in the series of samples obtained at 500 and 900 ºC, except in RP1 series, also increased the O_{XPS} and O_{TPD}. This has been observed with others carbon materials doped with boron in low concentrations [16,29].

The C_{1s} XP spectra of samples from P3 series are shown, as an example, in Figure A.I.6. The full width at the half maximum (FWHM) of the C_{1s} graphite peak at 284.6 eV was determined for all samples and their values are compiled in

Table 4. The FWHM of the graphite peak has been used [30] as a measurement of graphene layer homogeneity, with narrower XPS peaks corresponding to more homogeneous graphene layers. Results obtained show that FWHM decreased as heat-treatment temperature increased from 500 to 1500 ºC, due to the loss of oxygen atoms and to a certain ordering of the aromatic structures that constitute the graphene layers.

Table 4. Full width at the half maximum (FWHM) of the C_{1s} peak at 284.6 eV

Sample	FWHM C_{1s} (eV)	Sample	FWHM C_{1s} (eV)
R1	2.34	P1	2.63
R1-500	1.87	P1-500	1.42
R1-900	1.31	P1-900	1.25
RP1	2.64	P3	2.51
RP1-500	1.68	P3-500	1.45
RP1-900	1.24	P3-900	1.33
		P3-1500	1.23

The B_{1s} XP spectra of samples from P1 series are depicted, as an example, in Figure 1 and for the rest of samples are given in Figures A.I.7 to A.I.9 of the Appendix I. Deconvolution was difficult due to the low B content of these samples. However, all original organic aerogels (R1, RP1, P1, and P3) had only one peak at 192 eV, which can be assigned to boric acid or boric oxide [31]. Carbon aerogels obtained at 500 °C showed different peaks in the region between 190.6 and 193.8 eV, which can be assigned to B-O bonds in boron oxycarbide moieties and boron oxides [31-34]. Carbon aerogels obtained at 900

and 1500 ºC also showed an additional peak at 189.3-189.5 eV, which is assigned in the literature to a boron carbide, BC_3 [34,35].

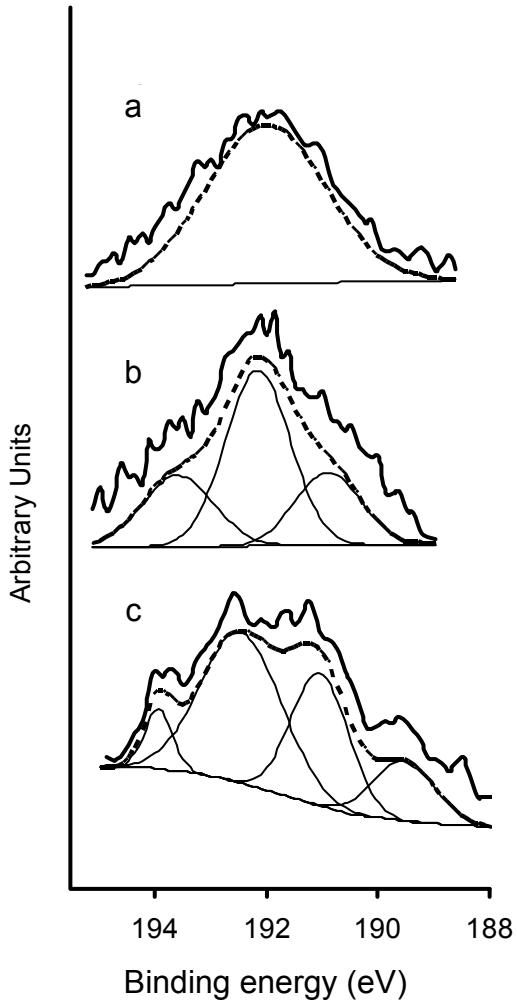

Figure 1. X-ray photoelectron spectroscopy profiles of the B1s region for samples: (a) P1, (b) P1-500, (c) P1-900.

4.2. Morphology and surface physics

SEM images of samples heat-treated to 900º C are shown in Figure 2. Images obtained at 500 and 1500 ºC are similar to those obtained at 900 ºC. Sample R1-900, prepared with resorcinol and formaldehyde, shows a very open structure similar to foam, in which the primary particles cannot be distinguished. The surface morphology was very different when pyrocatechol was used together with resorcinol in the formulation of the aerogel (sample RP1): the foam structure seen in sample R1 disappears, and primary particles with microbead shapes are fused into a continuous network. Finally, samples P1-900, P3-900 and POX-900, prepared with pyrocatechol, show a tendency for the microbead particles to overlap due to coalescence in the sol-gel state, giving rise to a more compact surface morphology.

N_2 adsorption-desorption isotherms at -196 ºC are depicted in Figure 3. CO_2 adsorption isotherms at 0 ºC are shown in Figure A.I.10 of the Appendix I. N_2 adsorption isotherms on samples R1-500 and R1-900 belong to Type I of the IUPAC classification [17], which is typical of microporous solids. These isotherms showed a small low-pressure hysteresis cycle, which is frequent in microporous adsorbents.

In samples from RP1 series, N_2 adsorption isotherms show Type I behavior at low relative pressure and an increase in uptake at high relative pressure, although without the limiting adsorption observed in Type IV isotherms. They are therefore similar to Type II isotherms, indicating that these samples contain

macropores or wide mesopores at the macropore limit. These isotherms show a Type H3 hysteresis loop [17].

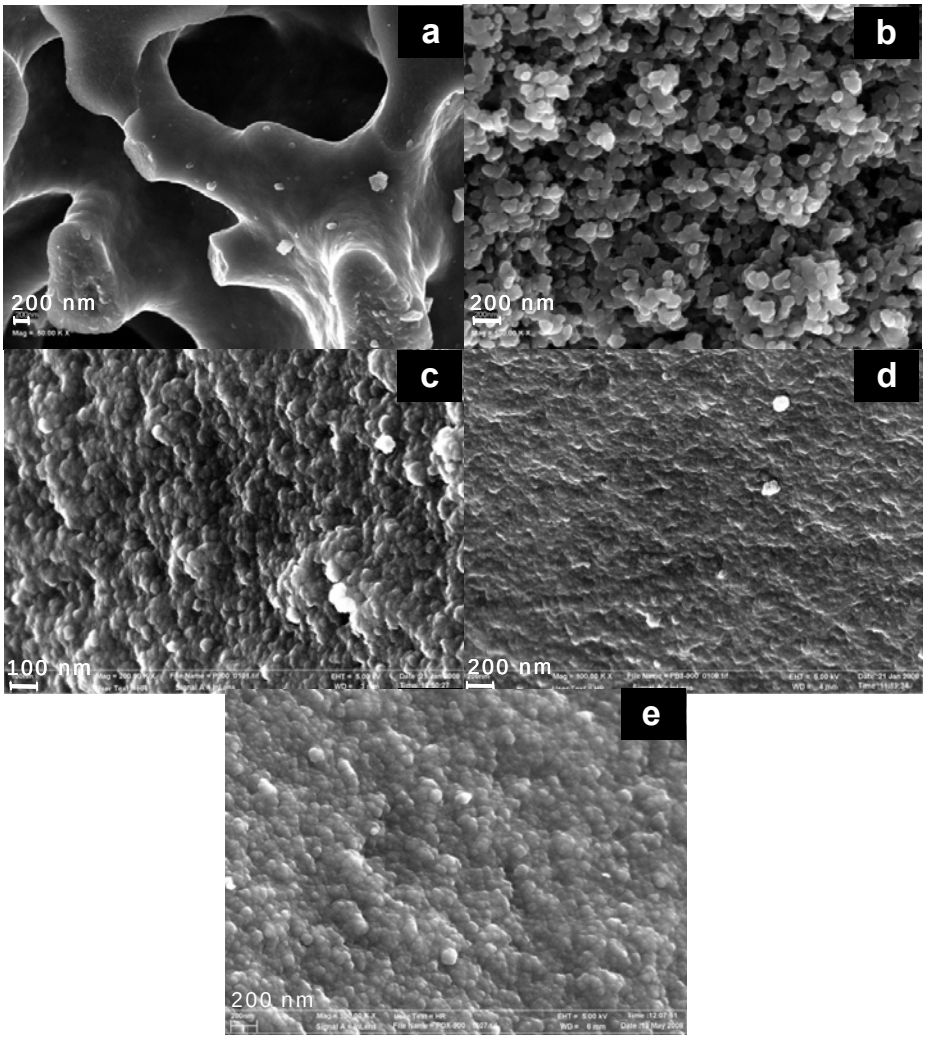

Figure 2. Transmission electron microscopy images of samples: (a) R1-900, (b) RP1-900, (c) P1-900, (d) P3-900, (e) POX-900.

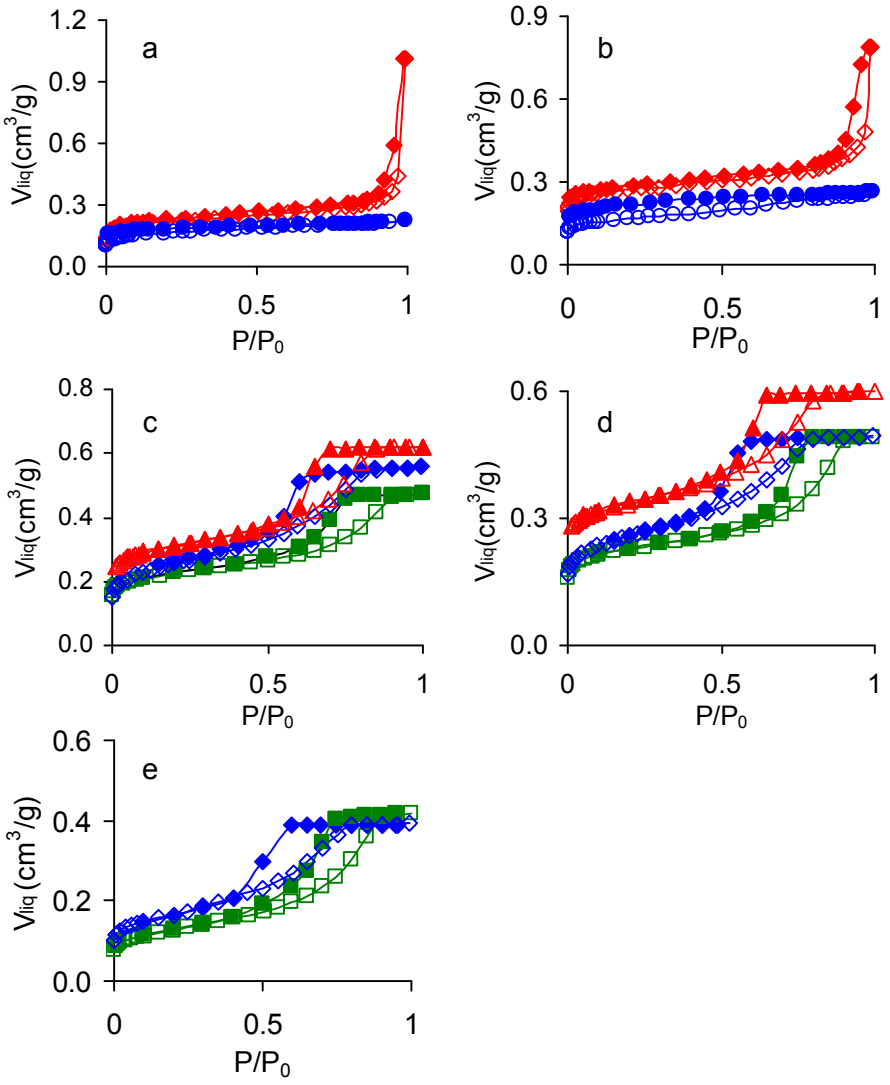

Figure 3. N_2 adsorption-desorption isotherms at -196º C on samples: (a) ○ R1-500 and ◊ RP1-500; (b) ○ R1-900 and ◊ RP1-900; (c) △ P1-500, ◊ P3-500 and □ POX-500; (d) △ P1-900, ◊ P3-900 and □ POX-900; (e) ◊ P3-1500 and □ POX-1500.Adsorption, open symbols and desorption, closed symbols.

N_2 isotherms for samples from P1, P3, and POX series belong to Type IV and are very different from those for the above carbon aerogels [17]. Characteristic features of these isotherms are their hysteresis loop, due to capillary condensation in mesopores, and the limiting uptake over a range of high relative pressures. The initial part of these isotherms at low relative pressures can be attributed to micropore filling in these samples. At high relative pressures, the amount adsorbed increases steeply due to capillary condensation. Then, when the high-pressure plateau of the isotherms is reached, the amount adsorbed should be equal to the sum of the micro- and mesopore volumes. The hysteresis loop of these samples is classified as Type H2 according to the IUPAC [17]. Importantly, the use of pyrocatechol instead of resorcinol produces a change in the N_2 adsorption isotherm because it gives rise to micro-mesoporous carbon aerogels.

4.2.1. Surface area and porosity of carbon aerogels from R1 and RP1 series.

Table 5 shows the results of applying the BET equation to N_2 isotherms and the DR equation to N_2 and CO_2 adsorption isotherms and the immersion enthalpy into benzene, from which the surface area accessible to benzene is obtained. The micropore volume $W_0(CO_2)$ yields the volume of narrow micropores (width < around 0.7 nm), while the micropore volume $W_0(N_2)$ yields the total micropore volume if there are not pore constrictions at their entrance [36]. Results obtained with R1 and RP1 samples show that $W_0(N_2) < W_0(CO_2)$, indicating that their microporosity is very narrow or with constrictions, so that all of the microposity cannot be measured by N_2 adsorption at -196 ºC [37]. Both micropore volumes increased with higher carbonization temperature.

Table 5. Porosity and surface area from adsorption isotherms and immersion enthalpy into benzene, and particle density for samples from R1 and RP1 series

	R1-500	R1-900	RP1-500	RP1-900
Porosity				
$W_0(N_2)$ (cm^3/g)	0.14	0.16	0.21	0.28
$W_0(CO_2)$ (cm^3/g)	0.21	0.28	0.31	0.33
$L_0(N_2)$ (nm)	0.58	0.80	1.10	0.71
$L_0(CO_2)$ (nm)	0.59	0.57	0.60	0.59
$V_{0.95}$ (cm^3/g)	0.23	0.25	0.37	0.43
ρ (g/cm^3)	0.73	0.81	0.71	0.76
Surface area				
S_{BET} (m^2/g)	387	401	525	670
$-\Delta_i(C_6H_6)$ J/g	65.8	95.5	70.8	86.9
S_{imm} (m^2/g)	577	839	622	762

The $V_{0.95}$ value for samples from R1 series was close to $W_0(CO_2)$, indicating that most of the micropores were filled with N_2 at the relative pressure of 0.95, which is high enough to overcome the diffusional limitations inside micropores. $V_{0.95}$ was somewhat higher than $W_0(CO_2)$ in samples from RP1 series, likely because there was also adsorption in meso- or macropores in addition to the filling of micropores, as evidenced by the shape of the N_2 adsorption isotherms in these samples (see Figures 3a and b). The low-pressure hysteresis of samples from R1 and RP1 series was due to diffusional limitations inside their micropores for N_2 molecules at -196 ºC, because they cannot desorb the adsorbate at low relative pressures once they have been filled at high relative pressures. Particle density increased with higher carbonization temperature.

These samples were analyzed by mercury porosimetry to determine the macroporosity of the samples and because the BJH method did not yield adequate mesoporosity results. The mercury intrusion-extrusion curves obtained are depicted in Figure A.I.11 of the Appendix I, and the quantitative results derived from them are compiled in Table 6. These curves show that there was no volume variation during depressurization.

Table 6. Porosity data from mercury porosimetry

Sample	V_{meso} (cm^3/g)	V_{macro} (cm^3/g)	V_{extr} (cm^3/g)	d_P (nm)
R1-500	0.00	0.54	0.53	702
R1-900	0.00	0.50	0.50	880
RP1-500	0.71	0.00	0.69	40
RP1-900	0.75	0.00	0.75	38

The shape of mercury intrusion curves may indicate that carbon aerogels were densified under the application of isostatic pressure. To test this possibility, it is recommended [38] to weigh the samples before and after the mercury porosimetry run in order to determine the mercury remaining within the pore network after depressurization. This volume, V_{extr}, was equal to the total pore volume (V_{meso} + V_{macro}) obtained from the intrusion curves (see Table 6). Therefore, the mercury porosimetry data corresponds to irreversible intrusion of Hg into the meso- and macropores and not to compression of the material under isostatic pressure.

Table 6 shows that samples from R1 series contain large macropores and no mesopores, in agreement with SEM observations of their morphology. In contrast, samples from RP1 series contained only large mesopores with a width, d_P, of around 40 nm, close to the upper limit of mesoporosity. These large mesopores were responsible for the shape of the N_2 adsorption-desorption isotherms of these samples (see Figure 3a and b).

Surface area values, S_{BET} and S_{imm}, are displayed in Table 5. The S_{mic} of these samples was not obtained, due to the N_2 diffusional limitations of their microporosity. The minimal dimension of N_2 (0.36 nm) and benzene (0.37 nm) are almost identical [23]; therefore, both molecules should have access to a similar slit-shaped micropore range. However, the S_{BET} can be underestimated with respect to the S_{imm} due to the restricted diffusion of N_2 at -196 ºC in very narrow micropores or in micropores with constrictions at their entrance, whereas benzene molecules can access all micropores due to the much higher temperature (30º C) at which immersion takes place.

In addition, narrow micropores do not allow a single molecular layer of N_2 to be accommodated on each micropore wall, whereas benzene molecules interact with both micropore walls in the immersion method, yielding a higher S_{imm} value. In micropores that are narrow or have restricted entrances, the BET method will yield an unrealistic value of the surface area. Samples from R1 and RP1 series have the S_{imm} value higher than the S_{BET} one, due to N_2 diffusion limitations of the micropores. Therefore, S_{imm} gives a more realistic value of the surface area of these carbon aerogels. In both series of samples, the S_{imm} increases with higher carbonization temperature.

4.2.2. Surface area and porosity of carbon aerogels from P1, P3 and POX series.

Table 7 shows results obtained from applying the BET equation to N_2 adsorption isotherms, the DR equation to N_2 and CO_2 adsorption isotherms, and the BJH method to the adsorption branch of N_2 adsorption isotherms and the outcomes of immersion enthalpy into benzene. Mesopore size distributions from BJH are shown in Figure A.I.12 of the Appendix I. In these samples, $W_0(N_2)$ was similar to or higher than $W_0(CO_2)$, and both increased up to a carbonization temperature of 900 ºC. A further carbonization to 1500 ºC decreased the micropore volumes due to the shrinkage of the carbon matrix. Mean micropore width ranged from 0.97 to 1.22 nm. According to these results, when pyrocatechol is used as the sole phenolic compound in the initial mixture, the carbon aerogels obtained after carbonization at 500-1500 ºC have a microporosity that is fully accessible to N_2 molecules at -196 ºC.

The mesopore volume, V_{BJH}, ranged from 0.3 to 0.4 cm^3/g and the mean mesopore size from 6.5 to 12.4 nm, depending on the recipe. The lower sizes correspond to carbon aerogels prepared with boric acid as catalyst, in which the increase in carbonization temperatures reduced the d_{BJH} value, which was not observed in samples from POX series. The $V_{0.95}$ value was similar or very close to the sum of $W_0(N_2)$ and V_{BJH}, indicating the goodness of the DR and BJH methods used to analyze the micro- and mesoporosity, respectively.

Table 7. Porosity and surface area from adsorption isotherms and immersion enthalpy into benzene, and particle density for samples from P1, P3 and POX series

	P1-500	P1-900	P3-500	P3-900	P3-1500	POX-500	POX-900	POX-1500
Porosity								
$W_0(N_2)$ (cm^3/g)	0.29	0.32	0.22	0.23	0.15	0.21	0.23	0.11
$W_0(CO_2)$ (cm^3/g)	0.19	0.29	0.18	0.23	0.09	0.20	0.24	0.10
$L_0(N_2)$ (nm)	1.17	1.10	1.21	1.20	1.22	0.97	1.05	1.09
$L_0(CO_2)$ (nm)	0.58	0.59	0.56	0.58	0.69	0.57	0.58	0.70
V_{BJH} (cm^3/g)	0.39	0.33	0.38	0.30	0.30	0.29	0.31	0.35
d_{BJH} (nm)	9.5	7.7	7.8	6.5	6.5	12.4	12.4	12.3
$V_{0.95}$ (cm^3/g)	0.62	0.60	0.55	0.49	0.39	0.47	0.49	0.42
$W_0(N_2)+V_{BJH}$ (cm^3/g)	0.68	0.65	0.60	0.53	0.45	0.50	0.54	0.46
ρ (g/cm^3)	0.91	1.04	0.94	1.01	1.03	0.96	1.01	1.02
Surface area								
S_{BET} (m^2/g)	738	800	590	598	373	514	519	285
$-\Delta_i(C_6H_6)$ J/g	81.2	90.6	62.1	67.9	43.0	59.2	59.7	30.9
S_{imm} (m^2/g)	712	795	545	595	377	519	523	271
S_{mic} (m^2/g)	496	582	364	383	246	433	438	202
S_{BJH} (m^2/g)	214	202	237	202	216	132	131	160
$S_{mic}+ S_{BJH}$ (m^2/g)	710	784	601	585	462	565	569	362

Apparent particle density was between 0.91 and 1.04 g/cm^3, higher than that obtained with carbon aerogels prepared from resorcinol or a resorcinol-pyrocatechol mixture. In addition, the particle density increased with carbonization temperature, as found with the other carbon aerogels.

S_{BET} was equal to S_{imm} in carbon aerogels from these series. In addition, both surface area values were also identical or very close to the S_{mic} + S_{BJH} values except in samples P3-1500 and POX-1500, where these values were fairly close. The agreement among the three surface area values in samples from P1, P3 and POX series is due to their wider $L_0(N_2)$ value in comparison to samples from R1 and RP1 series. Thus, Stoeckli et al. [39] reported that a reasonable agreement among S_{imm}, S_{BET} and S_{mic} + S_{ext} (S_{mic} + S_{BJH}, in our case) can be expected for carbons with $L_0(N_2)$ of approximately 0.8-1.1 nm.

4.3. Electrochemical capacitances

Figure 4 depicts cyclic voltammograms of different samples at a constant scan rate of 0.5 mV/s. These curves were used to obtain the gravimetric capacitances according to equation (3), which are displayed in Table 8. Carbon aerogels obtained at 900 and 1500 ºC, except P3-900 and POX-900, show cyclic voltammograms with no significant peaks attributed to redox processes on the carbon surface, and they have the quasi-rectangular shape expected for capacitors, in which the main contribution to the capacitance is the charge-discharge of the double-layer [7,8,11].

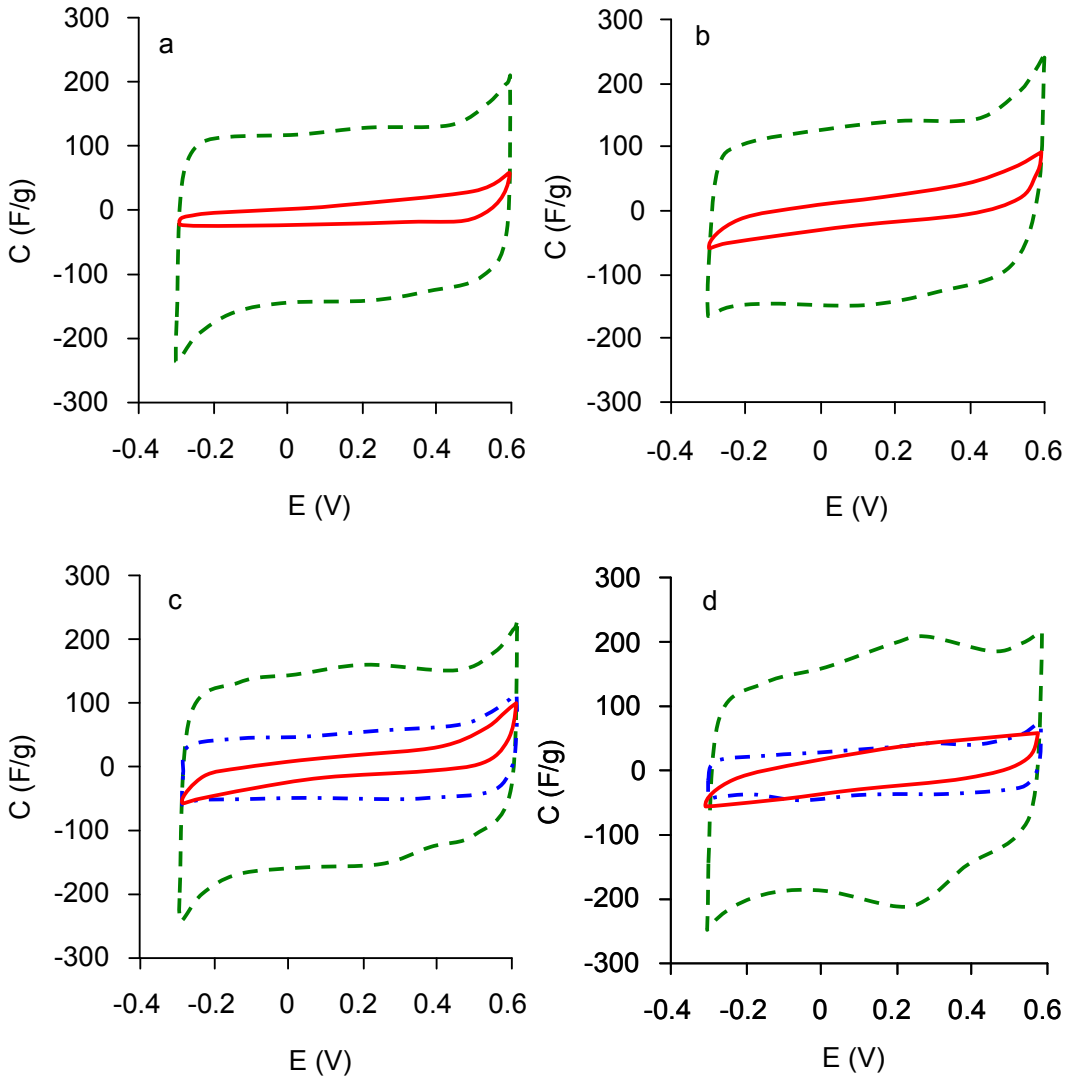

Figure 4. Cyclic voltammograms of carbon aerogels at a scan rate of 0.5 mV/s in 1M H_2SO_4: (a) RP1, (b) P1, (c) P3 and (d) POX. Samples obtained at 500 ºC (——) at 900 ºC (- - - -) and 1500 ºC (- · - · -).

Table 8. Gravimetric capacitances of carbon aerogels from cyclic voltammetry (C_{CV}) at different scan rates and chronopotentiometry (C_{CP}) at 100 mA/g, extrapolated capacitances at zero (C_0) and infinite (C_∞) scan rates, and interfacial capacitance (IC_{CP})

Sample	C_{CV} (F/g)			C_0 (F/g)	C_∞ (F/g)	C_{CP} (F/g)	IC_{CP} (μF/cm^2)*
	0.5 mV/s	1 mV/s	5 mV/s				
RP1-500	15	13	10	19	8	8	2
RP1-900	134	128	106	153	95	144	21
P1-500	28	22	15	40	9	25	3
P1-900	132	128	109	145	101	137	17
P3-500	22	16	11	34	5	10	2
P3-900	146	133	120	156	108	146	24
P3-1500	50	48	41	55	38	48	13
POX-500	30	24	17	42	11	40	8
POX-900	172	167	142	183	143	175	34
POX-1500	36	35	31	39	29	35	12

* IC_{CP} values were obtained from C_{CP} and S_{BET}

Cyclic voltammograms of POX-900 and P3-900 deviate from the rectangular shape and show a more or less broad wave with a maximum at ca. 0.3 V (SCE), due to a quinone/hydroquinone redox process [10,12,40]. Therefore, the interfacial capacitance in these carbon aerogels is composed of double-layer and pseudofaradaic capacitance.

Carbon aerogels obtained at 500 ºC showed lower C_{CV} values than those obtained at 900 ºC, although the surface area and pore texture of samples from the same series treated at these temperatures were quite close in some cases (see Table 7). Cyclic voltammograms of some samples obtained at 500 ºC, especially P3-500 and POX-500, are not symmetric, and the capacitance increased with an increase in potential within the potential window used. The shape of the cyclic voltammograms and the C_{CV} values of samples obtained at 500 ºC indicate a higher electrical resistance in comparison to those obtained at 900 ºC. This is due to a lower level of aromatization of the former, already evidenced by the variation in the FWHM of the C_{1s} peak in the XP spectra with different temperature treatments (see above). Similar variations in capacitance and cyclic voltammogram shape were reported in activated carbons with different degrees of aromatization [41,42].

C_{CV} decreased when the scan rate increased because the capacitance of porous electrodes depends on this rate [11,43]. Ions can reach both inner and

external surfaces of porous carbon materials at low scan rates, whereas only the exterior surface is accessible at high rates [44]. Hence, ion diffusion through the solid porosity controls the charging process [8,11], producing a similarity between the capacitance of a porous solid and reactions controlled by diffusion.

In this case, the capacitance would be a linear function of $s^{-½}$, and the inverse of capacitance would also be a linear function of $s^{½}$ [8]. Plots obtained are shown in Figure A.I.13 of the Appendix I. When $s^{-½}$ is extrapolated to zero in the C vs. $s^{-½}$ plot, the value of the capacitance obtained, C_∞, corresponds to the more readily available pores, i.e., the wider pores. Likewise, when $s^{½}$ is extrapolated to zero in the 1/C vs. $s^{½}$ plot, the capacitance value obtained, C_0, corresponds to the value observed when equilibrium is reached in all pores available to the electrolyte. C_0 and C_∞ values are compiled in Table 8.

Figure 5 depicts the chronopotentiometric curves obtained with the above samples at a constant current density of 100 mA/g. These curves have a quasi-triangular shape for samples obtained at 900 and 1500 ºC, whereas those obtained at 500 ºC show a deviation of the triangular shape due to their higher electrical resistance. Gravimetric capacitances were also obtained from these curves, C_{CP}, by applying equation 4, and the results are also shown in Table 8.

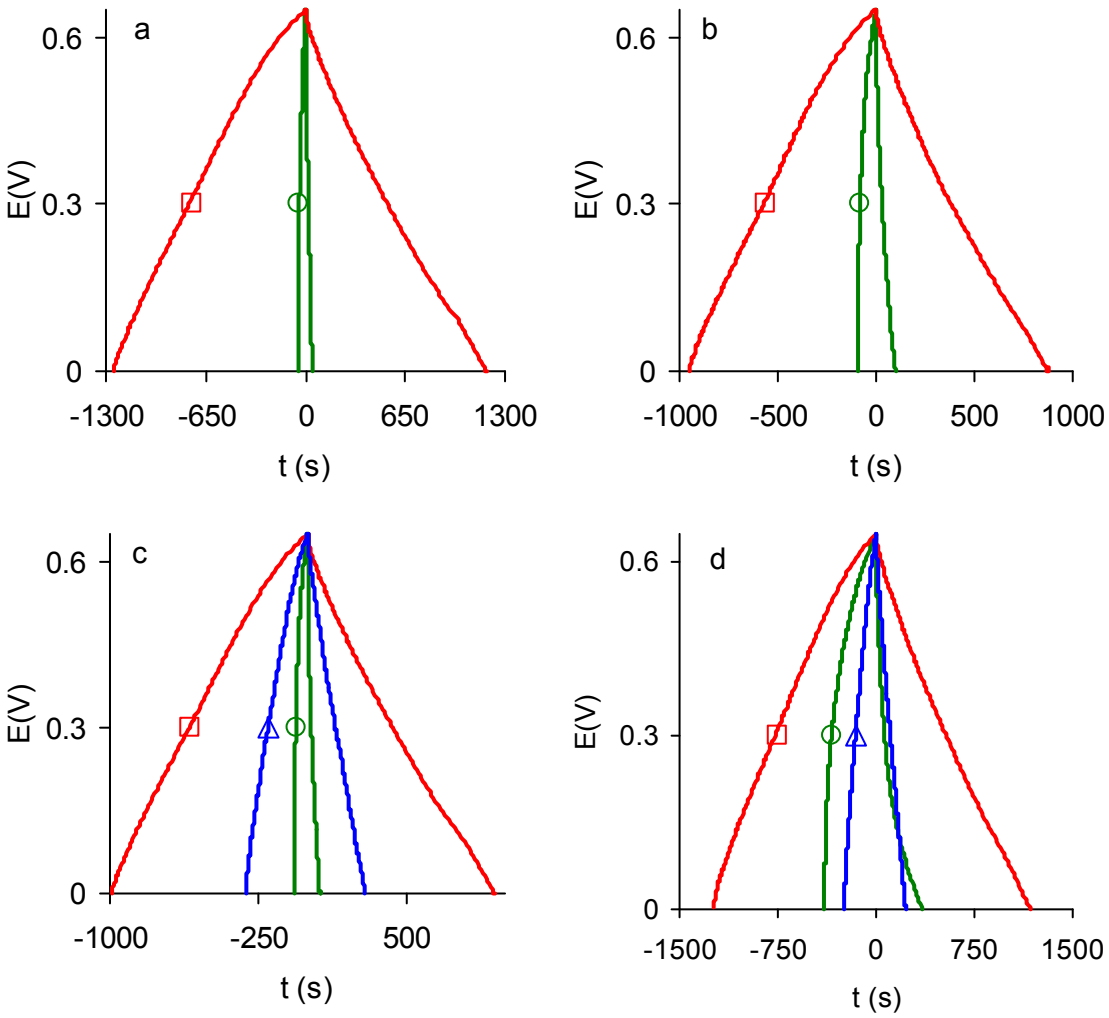

Figure 5. Chronopotentiometric curves obtained at 100 mA/g in 0.1M H_2SO_4: (a) RP1, (b) P1, (c) P3 and (d) POX. Samples obtained at 500 ºC (○), at 900 ºC (□) and 1500 ºC (△).

C_{CP}, C_{CV} at the lowest scan rate and C_0 were fairly close or close, especially in samples prepared at 900 ºC. C_∞ values were lower than C_0 because they would correspond to the capacitance at the more external surface of the carbon aerogels, i.e., in meso- and macropores. In each series, the highest capacitance was attained in samples heat-treated at 900 ºC. The interfacial capacitance, IC_{CP}, obtained from C_{CP} and the BET surface area of RP1-900, P1-900, and P3-900 ranged between 17 and 24 μF/cm^2 (Table 8). These values are in good agreement with the interfacial capacitance of a clean graphite surface [8,11], 20 μF/cm^2, and with the values ranging from 20 to 30 μF/cm^2 reported for different carbons [7,40], indicating a good electrolyte accessibility to the microporosity of the carbon aerogels.

The B content of RP1-900, P1-900, and P3-900 ranged from 0.1 to 0.3 % (BXPS in Table 3), and as above commented the increase in B content brought about an increase in the O content of the samples. It has been reported [16] that boron enhances both pseudofaradaic and double-layer capacitances. This is due to it increases the oxygen content and the charge density/density of states. Sample P3-900 with the highest B content shows pseudofaradaic effects in its cyclic voltammogram (Figure 4c) due to its highest O content. However, no B atoms were found (from XPS) substituting C atoms in the graphene layers that could have played a role in increasing the density of states/charge density and so the double-layer capacitance [45].

The highest IC_{CP} value, 34 μF/cm^2, was obtained with sample POX-900, due to the contribution of pseudofaradaic capacitance to the total capacitance. Heat

treatment of samples to 1500 ºC reduced the gravimetric and interfacial capacitance produced by the decrease in their micropore volumes.

5. CONCLUSIONS

The use of pyrocatechol instead of resorcinol in the preparation of organic gels with boric acid as polymerization catalyst allowed the chelation of part of this boric acid, as evidenced by the reduction in the initial mixture pH. Most of the boric acid was removed from the organic hydrogels during the exchange of water with acetone before their supercritical CO_2 drying.

The total B content of carbon aerogels was 0.1-0.3 %, and its distribution in the carbon matrix depended on the heat-treatment temperature at which the carbon aerogel was obtained. The XPS-determined chemical nature of the boron in the carbon aerogel also depended on the treatment temperature: the presence of B-O bonds was observed in boron oxycarbide moieties and boron oxide, while samples obtained at 900 and 1500 ºC also showed the presence of a boron carbide.

When the heat-treatment of samples increased from 500 to 1500 ºC, there was a narrowing of the C_{1s} peak of the XP spectra due to a loss of oxygen atoms and a certain ordering of the aromatic structures that constitute the graphene layers.

The use of pyrocatechol as the sole phenolic compound instead of resorcinol or a resorcinol-pyrocatechol mixture yielded carbon aerogels with no micropore constrictions and therefore with a microporosity fully accessible to N_2 molecules at -196 ºC. In addition, there was a profound change in the shape of the N_2 adsorption isotherms at -196 ºC, because the samples obtained with pyrocatechol were micro-mesoporous and showed a Type IV isotherm with Type H2 hysteresis cycle. The mesopore volume ranged from 0.3 to 0.4 cm^3/g and the mean mesopore size from 6.5 to 12.4 nm depending on the acid catalyst used (boric or oxalic acid) and the carbonization temperature. In contrast, the sample prepared with resorcinol was micro-macroporous and the sample prepared with a resorcinol-pyrocatechol mixture was micro-macroporous with large mesopores (around 40 nm width).

Carbon aerogels obtained at 500 ºC showed lower capacitance than those obtained at 900 ºC due to the higher electrical resistance resulting from their lower degree of aromatization. Carbon aerogels obtained with boric acid as polymerization catalyst and heat-treated at 900ºC showed an interfacial capacitance between 17 and 24 $\mu F/cm^2$. The influence of B on the capacitance was due to pseudofaradaic capacitance introduced by the increase in O content when B content increased. The sample prepared from polymerization of pyrocatechol and formaldehyde in the presence of oxalic acid and heat-treated at 900 ºC showed the highest interfacial capacitance, 34 $\mu F/cm^2$, due to the contribution of pseudofaradaic capacitance to the total capacitance. Heat treatment of samples to 1500 ºC reduced both gravimetric and interfacial capacitances.

6. REFERENCES

[1] Inagaki M, Kaneko K, Nishizawa T. Nanocarbons--recent research in Japan. Carbon 2002; 42(8-9):1401-17.

[2] Pekala RW. Organic aerogels from the polycondensation of resorcinol with formaldehyde. J Mat Sci 1989; 24(9):3221-7.

[3] Moreno-Castilla, C. Carbon gels in catalysis. In Serp P, Figueiredo JL, Editors. Carbon materials for catalysis, New York: J. Wiley & Sons, 2009: Chapter 10.

[4] Fairén-Jiménez D, Carrasco-Marín F, Moreno-Castilla C. Adsorption of benzene, toluene and xylenes on monolithic carbon aerogels from dry air flows. Langmuir 2007; 23(20):10095-101.

[5] Carrasco-Marín F, Fairén-Jiménez D, Moreno-Castilla C. Carbon aerogels from gallic acid-resorcinol mixtures as adsorbents of benzene, toluene and xylenes from dry and wet air under dynamic conditions. Carbon 2009; 47(2):463-9.

[6] Pekala RW, Farmer JC, Alviso CT, Tran TD, Mayer ST, Miller JM, et al. Carbon aerogels for electrochemical applications. J Non-Cryst Solids 1998; 225(1):74-80.

[7] Frackowiak E, Beguin F. Carbon materials for the electrochemical storage of energy in capacitors. Carbon 2001; 39(6):937-50.

[8] Babic B, Kaluderovic B, Bracar Lj, Krstajic N. Characterization of carbon cryogel synthesized by sol-gel polycondensation and freeze-drying. Carbon 2004; 42(12-13): 2617-24.

[9] Pandolfo AG, Hollenkamp AF. Carbon properties and their role in supercapacitors. J Power Sources 2006; 157(1):11-27.

[10] Bruno MM, Cotella NG, Miras MC, Koch T, Seidler S, Barbero C. Characterization of monolithic porous carbon prepared from resorcinol/formaldehyde gels with cationic surfactant. Colloids Surf A 2010;358(1-3):13-20.

[11] Szczurek A, Jurewicz K, Amaral-Labat G, Fierro V, Pizzi A, Celzard A. Structure and electrochemical capacitance of carbon cryogels derived from phenol-formaldehyde resins. Carbon 2010;48(13):3874-83.

[12] Calvo EG, Ania CO, Zubizarreta L, Menéndez JA, Arenillas A. Exploring new routes in the synthesis of carbon xerogels for their application in electric double-layer capacitors. Energy Fuels 2010; 24(6):3334-9.

[13] Greenwood NN, Earnshaw A. Chemistry of the elements. Oxford, UK: Butterworth-Heinemann; 1997. p. 230

[14] Acharya CK, Turner CH. Stabilization of Platinum Clusters by Substitutional Boron Dopants in Carbon Supports. J Phys Chem B 2006; 110(36):17706-10.

[15] Acharya CK, Turner CH. Effect of an electric field on the adsorption of metal clusters on boron-doped carbon surfaces. J Phys Chem C 2007; 111(40), 14804-12.

[16] Wang DW, Li F, Chen ZG, Lu GQ, Cheng HM. Synthesis and Electrochemical Property of Boron-Doped Mesoporous Carbon in Supercapacitor. Chem Mater. 2008;20(22):7195-200.

[17] Sing KSW, Everett DH, Haul RAW, Moscou L, Pierotti RA, Rouquerol J, et al. Reporting physisorption data for gas/solid systems with special reference to the determination of surface area and porosity. Pure & Appl Chem 1985;57(4):603-19.

[18] Stoeckli F. Characterization of microporous carbons by adsorption and immersion techniques. In: Patrick JW, editor. Porosity in carbons: characterization and applications, London: Edward Arnold, 1995: 66-97.

[19] Bansal RC, Donnet JB. Stoeckli F. Active Carbon. New York: Marcel Dekker. 1988: Chapter 3.

[20] Denoyel R, Fernández-Colinas J, Grillet Y, Rouquerol J. Assessment of the surface-area and microporosity of activated charcoals from immersion calorimetry and nitrogen adsorption data. Langmuir 1993; 9(2): 515-8.

[21] Gonzalez MT, Sepúlveda-Escribano A, Molina-Sabio M, Rodriguez-Reinoso F. Correlation between Surface Areas and Micropore Volumes of Activated Carbons Obtained from Physical Adsorption and Immersion Calorimetry. Langmuir 1995; 11(6): 2151-5.

[22] Silvestre-Albero J, Gómez de Salazar C, Sepúlveda-Escribano A, Rodriguez-Reinoso F. Characterization of microporous solids by immersion calorimetry. Colloids Surf A 2001; 187-188: 151-65.

[23] Villar-Rodil S, Denoyel R, Rouquerol J, Martinez-Alonso A, Tascon JMD. Characterization of aramid based activated carbon fibres by adsorption and immersion techniques. Carbon 2002; 40(8): 1376-80.

[24] Al-Muhtaseb SA, Ritter JA. Preparation and properties of resorcinol-formaldehyde organic and carbon gels. Adv Mater 2003; 15: 101-14.

[25] Job N, Thery A, Pirard R, Marien J, Kocon L, Rouzaud JN, et al. Carbon aerogels, cryogels and xerogels: Influence of the drying method on the textural properties of porous carbon materials. Carbon 2005;43(12):2481-94.

[26] Baumann TF, Worsley MA, Han TYJ, Satcher J. High surface area carbon aerogel monoliths with hierarchical porosity. J Non-Cryst Solids 2008; 354(29):3513-5.

[27] Fairén-Jiménez D, Carrasco-Marín F, Moreno-Castilla C. Porosity and surface area of monolithic carbon aerogels prepared using alkaline carbonates and organic acids as polymerization catalysts. Carbon 2006; 44(11):2301-07.

[28] Figueiredo JL, Pereira MFR, Freitas MMA, Orfao JJM. Modification of the surface chemistry of activated carbons. Carbon 1999; 37(9):1379-89.

[29] Zhong DH, Sano H, Uchiyama Y, Kobayashi K. Effect of low-level boron doping on oxidation behavior of polymide-derived carbon films. Carbon 2000; 38(8):1199-206.

[30] Darmstadt H, Roy C. Surface spectroscopic study of basic sites on carbon blacks Carbon 2003; 41(13):2662-5.

[31] Cermignani W, Paulson TE, Onneby C, Pantano CG. Synthesis and characterization of boron-doped carbons. Carbon 1995; 33(4): 367-74.

[32] Burgess JS, Acharya CK, Lizarazo J, Yancey N, Flowers B, Kwon G, et al. Boron-doped carbon powders formed at 1000ºC and one atmosphere. Carbon 2008; 46(13):1711-7.

[33] Jacobson LG, Shulze RK, Maia da Costa MEH, Nastasi M. X-ray photoelectron spectroscopy investigation of boron carbide films deposited by sputtering. Surf Sci 2004; 572(2-3):418-24.

[34] Ozaki J, Kimura N, Anahara T, Oya A. Preparation and oxygen reduction activity of BN-doped carbons. Carbon 2007; 45(9):1847-53.

[35] Kawaguchi J, Kawashima T, Nakajima T. Synthesis and structures of new graphite-like materials of composition BCN(H) and $BC_3N(H)$. Chem Mater 1996;8(6):1197-201.

[36] Cazorla-Amorós D, Alcañiz-Monge J, De la Casa-Lillo MA, Linares-Solano A. CO_2 as an adsorptive to characterize carbon molecular sieves and activated carbons. Langmuir 1998; 14(16):4589-96.

[37] Rodríguez-Reinoso F, Linares-Solano A. Microporous structure of activated carbons as revealed by adsorption methods. In: Thrower PA, editor. Chemistry and physics of carbon, vol 21, New York; Marcel Dekker; 1989, 1-146.

[38] Job N, Pirard R, Pirard JP. Alié C. Non intrusive mercury porosimetry: pyrolysis of resorcinol-formaldehyde xerogels. Part Part Syst Charact 2006; 23 (1):72-81.

[39] Stoeckli F, Centeno TA. On the determination of surface areas in activated carbons. Carbon 2005; 43(6):1184-90.

[40] Kinoshita K. Carbon: Electrochemical and physicochemical properties. New York: Wiley; 1988, p 293-387.

[41] Seredych M, Hulicova-Jurcakova D, Lu GQ, Bandosz TJ. Surface functional groups of carbons and the effects of their chemical character, density and accessibility to ions on electrochemical performance. Carbon 2008; 46(11):1475-88.

[42] Hulicova-Jurcakova D, Seredych M, Lu GQ, Bandosz TJ. Combined effect of nitrogen- and oxygen-containing functional groups of microporous activated carbon on its electrochemical performance in supercapacitors. Adv Funct Mater 2009; 19(3):438-47.

[43] Kotz R, Carlen M. Principles and applications of electrochemical capacitors. Electrochim Acta 2000; 45(15-16):2483-98.

[44] Wang DW, Li F, Liu M, Lu G, Cheng HM. 3D aperiodic hierarchical porous graphitic carbon material for high-rate electrochemical capacitive energy storage. Angew Chem Int Ed 2008; 47(2):373-6.

[45] Shiraishi S, Kibe M, Yokoyama T, Kurihara H, Patel N, Oya A, Kaburagi Y, Hishiyama Y. Electric double layer capacitance of multi-walled carbon nanotubes and B-doping effect. Appl Phys Mater A: Mater Sci Process 2006; 82: 585-91.

CHAPTER II

SUPERCAPACITOR PERFORMANCE OF CARBON GELS WITH VARIABLE SURFACE CHEMISTRY AND PHYSICS

1. ABSTRACT

This study describes the supercapacitor behavior of N-doped carbon xerogels in the form of microspheres and of carbon aerogels with varied porosities and surface oxygen complexes. The interfacial capacitance of N-doped carbon xerogels decreased with increased micropore surface area as determined by N_2 adsorption at -196 ºC. The interfacial capacitance showed a good correlation with the areal N_{XPS} concentration, although the best correlation was with the areal concentration of pyridinic functionalities. The gravimetric capacitance decreased with greater xerogel microsphere diameter. The interfacial capacitance of carbon aerogels increased with higher percentage of porosity as determined from particle and true densities. The interfacial capacity showed a linear relationship with the areal oxygen concentration and with the areal concentrations of CO- and CO_2- evolving groups.

2. INTRODUCTION

Supercapacitors, also termed electrochemical double-layer (EDL) capacitors, have attracted considerable attention as an alternative energy storage system that could enhance our ability to meet the rising demand for power [1-3]. Carbon is the most widely used material for supercapacitor electrodes due to its surface area, pore texture, surface chemistry, good polarizability, and easy processability, among other properties [1-3].

Electric charge storage in supercapacitors is mainly achieved by a non-faradaic mechanism, through the accumulation of ions on a double-layer at the electrode/electrolyte interface, and is dependent on the surface area and the accessibility of electrolyte to the carbon porosity. The capacitance can be improved by faradaic reactions that give rise to pseudocapacitance when surface functionalities such as surface nitrogen and surface oxygen complexes are present [4,5]. In the case of surface nitrogen complexes, this is due to the presence of pyridinic and pyrrolic or pyridonic functionalities, which increase the negative charge of the graphene layers [6-10], while quaternary nitrogen functionalities influence pseudocapacitance by increasing the positive charge of these layers [11]. In the case of surface oxygen complexes, the reversible hydroquinone/quinone redox reaction is widely considered to be responsible for pseudocapacitance in carbons [1,6,12]. In addition, surface nitrogen and oxygen functionalities, which are hydrophilic, can increase carbon capacitance by enhancing the wettability in aqueous solutions [2,7].

Carbon gels synthesized by the carbonization of organic gels using Pekala's method [13] have been used in adsorption [14], catalysis [15], and energy storage [1-3,16], among other applications. Their advantages include the versatility of their surface area, pore texture and surface chemistry, which can be controlled by varying their synthesis conditions and treatments. Furthermore, they can be obtained at a high purity or readily doped with different elements, and they can be prepared in a variety of forms, including pellets, microspheres, irregular-shaped powders, and films.

The objectives of this study were to examine the effect on capacitance in acidic medium of: i) the different N functionalities of N-doped carbon xerogels in the form of microspheres; and ii) the porosity and surface oxygen complexes of carbon aerogels. N-doped carbon xerogels were prepared by using the N-containing organic monomers 3-hydroxy aniline, 3-hydroxy pyridine, and melamine [17].

3. EXPERIMENTAL

Samples used in this work were carbon xerogels and aerogels whose preparation and characterization were previously reported [17-20]. Their recipes and synthesis procedures are displayed in Table 1. In addition, portions of carbonized sample G were CO_2-activated at 800 ºC to obtain two different degrees of activation (16 % and 27 % weight loss) and were designated G-16 and G-27, respectively. Finally, portions of carbon aerogel CA1 were oxidized with H_2O_2 and $(NH_4)_2S_2O_8$, following previously described methods [20,21], and designated CA1H and CA1S, respectively.

Electrochemical measurements were carried out in a Biologic multichannel potentiostat at room temperature using a 1 M H_2SO_4 solution as electrolyte. The working electrode was prepared by mixing the finely ground carbon gel, acetylene black (Denki Kagaku Kogyo Co., Japan), and binder (polytetrafluoroethylene, PTFE) at a weight ratio of 80:10:10. The mixture so obtained was pasted on graphite paper. The as-prepared electrodes were investigated with a typical three-electrode configuration using Ag/AgCl as reference electrode and a Pt wire as counter electrode.

Table 1. Recipes and synthesis procedures of carbon gels

Sample	R[a] (mol)	F[b] (mol)	C[c] (mol)	W[d] (mL)	Other ingredients (mol)	Drying method	T[l] (ºC)
HAM700	nil	0.620	K_2CO_3 ($1.4x10^{-4}$)	1000	3HA[e] (0.16),M[f] (0.10)	80 ºC, 10^{-2} mbar, 48 h	700
MR700	0.100	0.390	K_2CO_3 ($1.9x10^{-4}$)	1000	M (0.06)	80 ºC, 10^{-2} mbar, 48 h	700
MR900	0.100	0.390	K_2CO_3 ($1.9x10^{-4}$)	1000	M (0.10)	80 ºC, 10^{-2} mbar, 48 h	900
HPR700	0.170	0.350	K_2CO_3 ($1.4x10^{-4}$)	1000	3HP[g] (0.11)	80 ºC, 10^{-2} mbar, 48 h	700
HPR900	0.170	0.350	K_2CO_3 ($1.4x10^{-4}$)	1000	3HP (0.11)	80 ºC, 10^{-2} mbar, 48 h	900
CA1	0.112	0.224	Na_2CO_3 ($1.4x10^{-4}$)	27	nil	Supercritical CO_2	950
CA3	0.112	0.224	Na_2CO_3 ($1.4x10^{-4}$)	24	THF[h] (3mL)	Supercritical CO_2	950
B	0.112	0.224	K_2CO_3 ($1.4x10^{-4}$)	15.3	nil	Supercritical CO_2	900
I	0.112	0.224	OA[i] ($1.4x10^{-4}$)	26.7	nil	Supercritical CO_2	900
G	0.056	0.224	nil	11	GA[j](0.056),E[k](49mL)	Supercritical CO_2	900

[a]R: resorcinol; [b]F: formadehyde; [c]C: catalyst; [d]W: water; [e]3HA: 3-hydroxy aniline; [f]M: melamine; [g]3HP;: 3-hydroxy pyridine; [h]THF: tetrahydrofurane; [i]OA: oxalic acid; [j]GA: gallic acid; [k]E: etanol; [l]carbonization temperature.

Cyclic voltammograms were obtained within the potential window of -0.3 to 0.6 V at scan rates of 0.5, 1, and 5 mV/s. The gravimetric capacitance of carbon gels, C_{CV} (F/g), was obtained from these curves by equation (1)

$$C_{CV} = \frac{\sum \Delta t |I|}{2m\Delta V} \qquad (1)$$

where $\Sigma|I|\Delta t$ is the area of the current (A) against time (s) curve, m the mass of active material in the electrode (g), and ΔV the voltage window (V). Chronopotentiograms were performed under a constant current loading of 100 mA/g in a voltage range of 0-0.7 V. The gravimetric capacitance from these measurements, CCP (F/g), was obtained by equation (2).

$$C_{CP} = \frac{I_d \Delta t}{m\Delta V} \qquad (2)$$

where I_d is the discharge current (A), Δt the discharge time (s), and ΔV the voltage (V).

4. RESULTS AND DISCUSSION

4.1. N-doped carbon xerogels

The surface physics and chemistry of N-doped carbon xerogels were reported in detail elsewhere [17] and are therefore not discussed in the present Chapter. These xerogels were prepared as microspheres and Table 2 shows their main surface characteristics. They were essentially microporous with a narrow microporosity. The mean micropore width determined from N_2 adsorption isotherms at -196 ºC, $L_0(N_2)$, ranged between 0.48 and 0.60 nm. Therefore, the microporosity of these samples would be fully accessible to the H_3O^+ ion, size-

range 0.362-0.42 nm [22,23], but less accessible to the hydrated SO_4^{2-} ion $[SO_4(H_2O)_{12}]^{2-}$, with an estimated size of 0.533 nm [23,24]. Accordingly, the EDL contribution to the overall capacitance in H_2SO_4 would be lower from hydrated sulfate ions than from H_3O^+ ions.

Table 2. Surface physics and chemistry of N-doped carbon xerogels

Sample	S_{mic}[a]	$L_0(N_2)$	Mean ⊘[b]	N_{XPS}	N-6[c]	N-5[d]	N-Q[e]
	m^2/g	nm	μm	$\mu mol/m^2$	$\mu mol/m^2$	$\mu mol/m^2$	$\mu mol/m^2$
HAM-700	327	0.58	1.38	17.3	7.6	5.9	3.8
MR-700	506	0.56	0.27	4.8	2.2	1.1	1.5
MR-900	560	0.60	0.25	3.7	1.2	0.9	1.6
HPR-700	522	0.48	3.36	1.6	0.6	0.4	0.6
HPR-900	606	0.49	3.07	2.2	0.7	0.5	1.1

[a] From DR equation applied to N_2 adsorption isotherm at -196 K. $S_{mic} = 2000W_0/L_0$ where W_0 is the micropore volume (cm^3/g) and L_0 the mean micropore width (nm); [b] Mean diameter of the microespheres from SEM; [c] N-6: Pyridinic-N; [d] N-5: Pyrrolic or Pyridonic-N; [d] N-Q: Quaternary-N

Table 2 also includes the diameter of the microspheres, from scanning electron microscopy (SEM), and the type and concentration of N functionalities as determined by deconvolution of the N_{1s} X-ray photoelectron peak. N-6 and N-5 functionalities are located at the edges of the graphene layers, whereas N-Q functionalities are found within them.

Cyclic voltammograms of the samples are depicted in Figure 1. These curves are useful to estimate the difference between EDL capacitance and

pseudofaradaic effects, and they also allow to determine the electrode capacitance by applying equation (1). Similar cyclic voltammogram shapes were obtained with other N-doped carbons from melamine using either H_2SO_4 or KOH as electrolytes [8,23]. The cyclic voltammogram shapes are non-rectangular, indicating a deviation from the ideal double-layer capacitor. This deviation could be likely due to a pseudofaradaic contribution to sample capacitance and not to kinetic effects on pores, given that the scan rate was very slow. However, due to the big size of the hydrated anions an ion siveing effect [25,26] cannot be discarded.

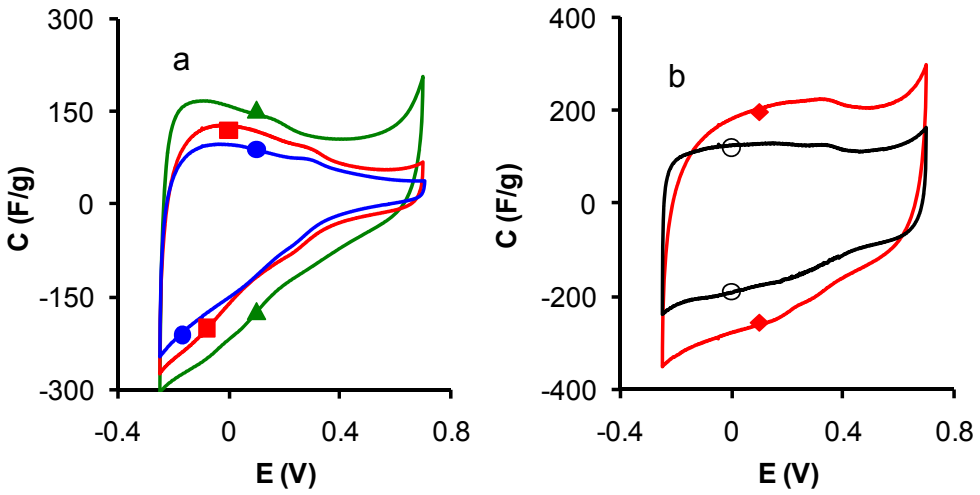

Figure 1. Cyclic voltammograms of N-doped carbon xerogels at a scan rate of 0.5 mV/s in 0.1 M H_2SO_4: (a) ▲, HAM-700; ■, HPR-700 and ●, HPR-900; (b) ◆, MR-700 and ○, MR-900.

A voltammetric peak is observed in all voltammograms at approximately 0.3 V mainly in the positive scan that can be associated to a pseudofaradic contribution of the nitrogen groups.

The pseudofaradaic effects are attributed to the presence of surface nitrogen complexes (e.g., pyridinic and pyridonic or pyrrolic complexes) that can undergo faradaic redox reactions [6-10]. These surface groups, located at the graphene layer edges, are easily reached by the electrolyte and enhance the carbon basicity [27] through a strong π delocalization in graphene layers, due to the electron-rich nature of these nitrogen sites. Therefore, protons can be attracted to the electrode surface, giving rise to pseudocapacitive interactions [8].

Using the density functional theory method, Zhu et al [11] demonstrated a weakening of the π electron conjugation in a graphene sheet model with one and two substitutional N atoms in the form of quaternary N complexes, reducing the electron conductivity and producing a major increase in the HOMO energy of the graphene sheet. Because of this increased HOMO energy, graphene sheets with N-Q functionalities would be more positively charged when used as anode material in supercapacitors, attracting more negatively-charged ions and increasing the capacitance. The elevated electrical resistivity and capacitance per unit surface area of N-doped carbon aerogels used as supercapacitors has been attributed to this process [8,11].

Chronopotentiometric curves of N-doped carbon xerogels are depicted in Figure 2. Charge and discharge curves are not symmetrical, as the cyclic voltammograms, and they deviate from the triangular shape. This deviation

indicates pseudofaradaic and/or ion sieving effects. Gravimetric capacitances, C_{CV} and C_{CP}, were obtained from cyclic voltammograms and chronopotentiometric curves by applying equations (1) and (2), respectively. Results obtained are compiled in Table 3. C_{CV} decreased with higher scan rate because of the influence of this rate on the capacitance of porous electrodes [28,29]: ions can reach both inner and external surfaces of porous carbon materials at low scan rates but only the external surface at high rates [30]. C_{CV} values at the low scan rate were similar to C_{CP} values in all samples.

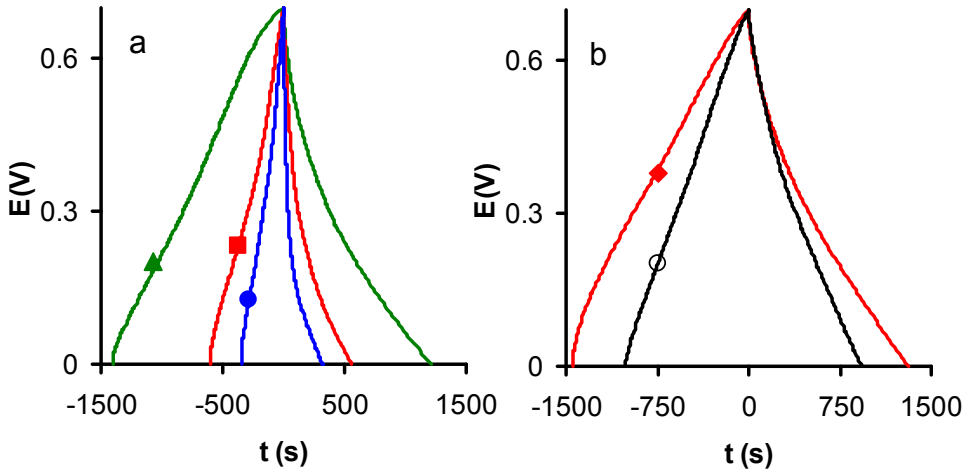

Figure 2. Chronopotentiometric curves of N-doped carbon xerogels obtained at 100 mA/g in 0.1 M H_2SO_4: (a) ▲, HAM-700; ■, HPR-700 and ●, HPR-900; (b) ◆, MR-700 and ○, MR-900

Galvanostatic discharge, the most accurate method to determine capacitance [31], was used to obtain the interfacial capacitance, IC_{CP}, dividing C_{CP} by S_{mic}

(Table 3). The relationship between IC_{CP} and S_{mic} is depicted in Figure 3, which shows a decrease in IC_{CP} with larger micropore surface area. This variation may be explained by a reduction in electronic and ionic accessibility to pores and/or N functionalities with greater S_{mic} [32]. In addition, it has also been reported [2,12] that the EDL capacitance is much lower on basal planes in graphite than at its edges. Because the micropore walls are formed by graphitic microcrystallite basal planes [33], with a predominance of edge sites at the external surface, a rise in the S_{mic} increases the proportion of surface sites constituted by basal planes *versus* edge sites, reducing interfacial capacitance.

Table 3. Gravimetric capacitances of N-doped carbon xerogels from cyclic voltammetry (C_{CV}) at different scan rates and chronopotentiometry (C_{CP}) at 100 mA/g, and interfacial capacitance (IC_{CP})

	C_{CV} (F/g)			C_{CP} (F/g)	IC_{CP} (μF/cm^2)
	0.5mV/s	1mV/s	5mV/s		
HAM-700	137	119	104	140	43
MR-700	200	175	149	196	39
MR-900	135	132	116	132	24
HPR-700	93	89	77	94	18
HPR-900	76	65	58	65	11

The relationship between the IC_{CP} and areal N_{XPS} concentration is depicted in Figure 4a, which also includes data on other samples described in the literature at the same current loading of 100 mA/g [10]. This Figure indicates a good agreement between the two parameters in the studied range. IC_{CP} values were plotted against the areal concentration of N-6, N-5, and N-Q functionalities (Figs.

4b, c, and d, respectively) in order to analyze the influence of the different surface nitrogen complexes. The interfacial capacitance showed the best correlation with the areal concentrations of pyridinic functionalities and the worst correlation with quaternary nitrogen functionalities.

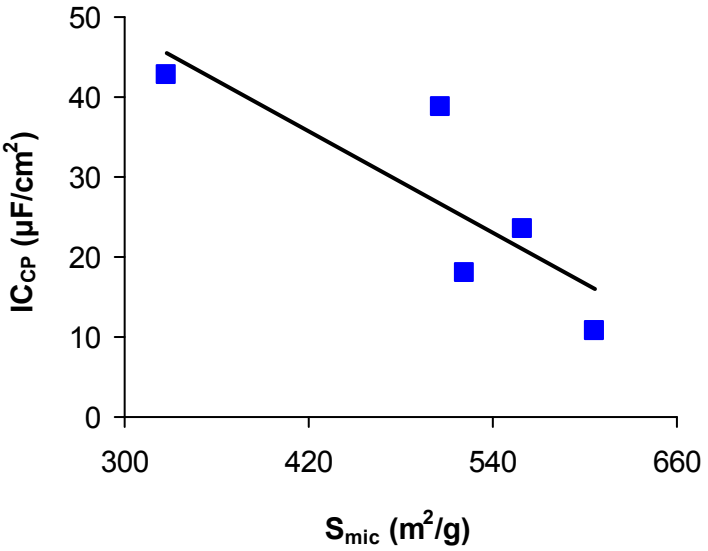

Figure 3. Relationship between the interfacial capacitance and micropore surface area in N-doped carbon xerogels

The poor correlation between IC_{CP} and N-Q in our samples may be due to the lower accessibility of the hydrated sulfate ions to their microporosity, given that electroadsorption of these negative ions would be on the positively-charged (due to N-Q functionalities) graphene layers that can form the micropore walls.

Figure 5 shows the trend of the gravimetric capacitance to decrease with greater mean diameter of the N-doped carbon xerogel microspheres. A study of carbon aerogels microspheres prepared by inverse emulsion polymerization [34]

also found a decrease in KOH-determined capacitance with larger microsphere size.

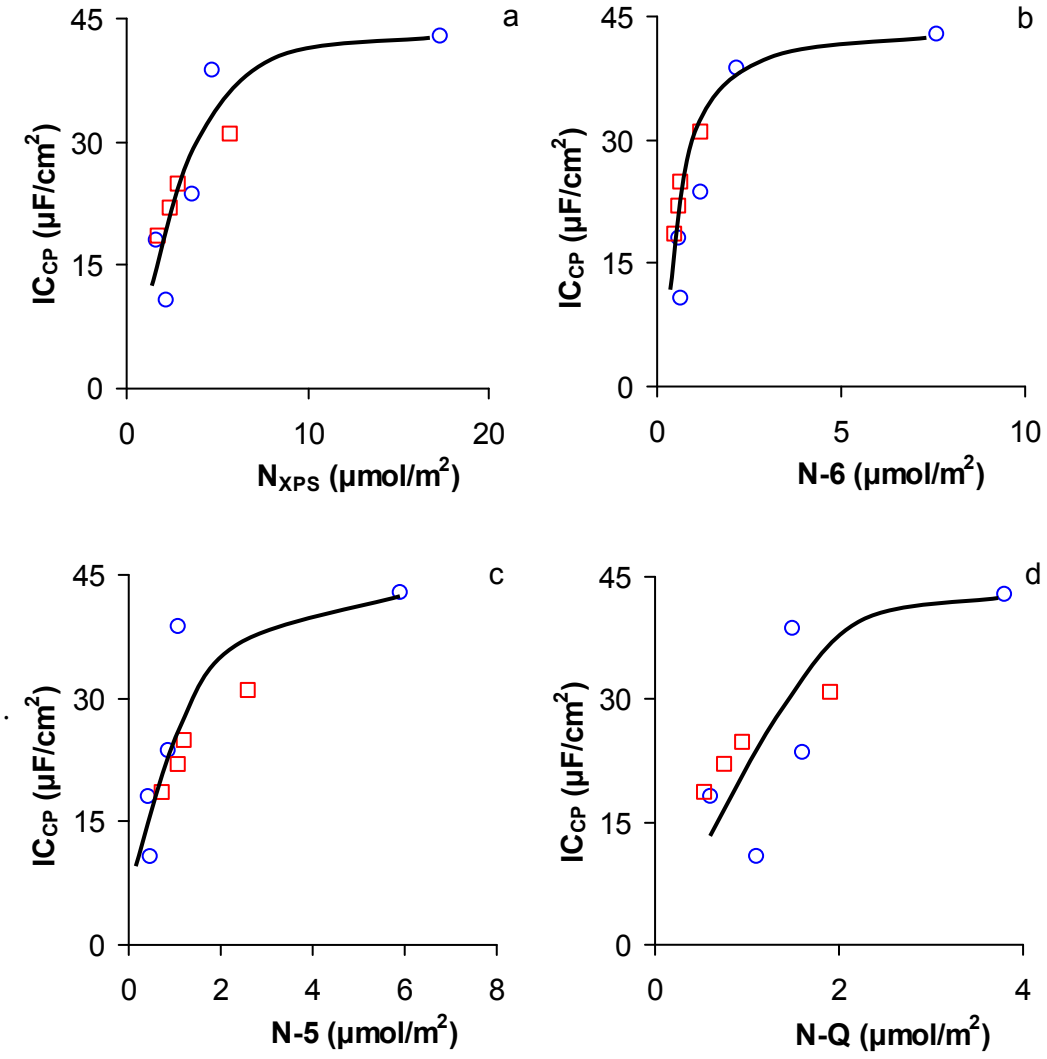

Figure 4. Interfacial capacitance at 100 mA/g in 0.1 M H_2SO_4 *versus* areal concentrations of nitrogen (a) and of N-6 (b), N-5 (c) and N-Q (d) functionalities. Symbols: ○, samples from this work and □, samples from [10].

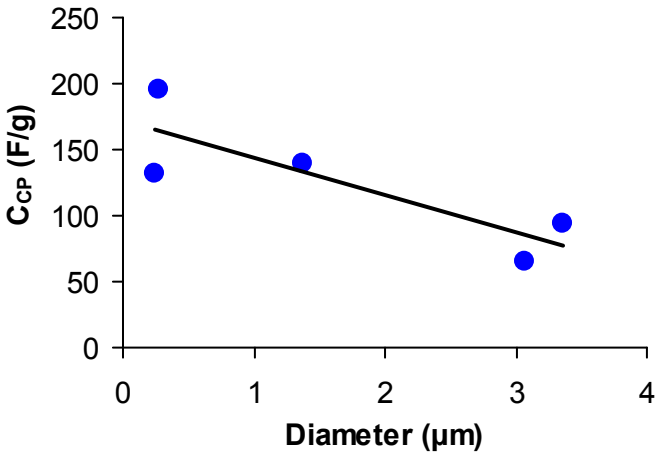

Figure 5. Relationship between the gravimetric capacitance and the mean diameter of the N-doped carbon xerogel microspheres

4.2. Carbon aerogels

The surface area and porosity of the carbon aerogels are compiled in Table 4. The samples were micro-mesoporous (B, G, G-16, G-27 and CA1) or micro-macroporous (I and CA3). The percentage of porosity of these samples was calculated from the particle and true densities, $\rho_{particle}$ and ρ_{true}, respectively, by applying equation (3) and considering ρ_{true} equal to 2 g/cm^3 [35].

$$P(\%) = \left(1 - \frac{\rho_{particle}}{\rho_{true}}\right) \times 100 \quad (3)$$

Table 5 shows the oxygen content determined from temperature programmed desorption, O_{TPD}, and the amounts of CO and CO_2 evolved at 1000ºC from sample CA1, along with the oxidized samples (CA1H and CA1S) obtained.

Table 4. Surface area and porosity of carbon aerogels

Sample	S_{BET}	$W_0(N_2)$[a]	$L_0(N_2)$[a]	V_P[b]	d_P[b]	$\rho_{particle}$	Porosity
	m^2/g	cm^3/g	nm	cm^3/g	nm	g/cm^3	%
B	813	0.31	0.68	0.79	34	0.62	69
I	740	0.30	0.65	0.70	$>10^3$	0.86	57
G	907	0.36	1.10	0.56	15	0.79	60
G-16	1192	0.49	1.33	0.57	15	0.77	61
G-27	1537	0.64	1.77	0.81	16	0.74	63
CA1	618	0.26	0.80	0.86	33	0.64	68
CA3	592	0.26	0.76	0.94	148	0.65	67

[a] $W_0(N_2)$ and $L_0(N_2)$ are the micropore volume and the mean micropore width, respectively, from DR equation applied to the N_2 adsorption isotherms at -196 ºC.
[b] V_P and d_P are the pore volume and mean pore size, respectively, of pores wider than 3.7 nm, obtained from mercury porosimetry

.

Table 5. Oxygen content from temperature programmed desorption and amounts of CO and CO_2 evolved at 1000 ºC

Sample	O_{TPD}	CO	CO_2
	%	mmol/g	mmol/g
CA1	0.85	0.34	0.10
CA1H	3.41	1.20	0.46
CA1S	10.64	3.78	1.43

Cyclic voltammograms of several carbon aerogels are shown in Figure 6a, all exhibiting a quasi-rectangular shape. The presence of redox processes are also clearly observed in the voltammogram of G-27. Cyclic voltammograms of

oxidized samples are depicted in Figure 6b. Redox humps between 0.3 and 0.4 V *versus* Ag/AgCl, associated with quinone/hydroquinone redox processes [1,6,12], are clearly observed in sample CA1S, which had the highest oxygen content. Carbon aerogels CA1H and CA1 show very similar voltammetric profiles with smoother redox humps than CA1S. The respective chronopotentiometric curves are shown in Figures 7a and b presenting a symmetrical profile

The gravimetric capacitances, C_{CV} and C_{CP}, obtained from the voltammograms and the chronopotentiograms are given in Table 6. Interfacial capacitance, I_{CP}, was obtained from C_{CP} and S_{BET}. As with the N-doped carbon xerogels, the C_{CP} value was similar or very close to the C_{CV} determined at the low scan rate, and the C_{CV} was lower at higher scan rates. The capacitance loss was between 15 and 22 % for all samples except sample I (around 30 %), which was the carbon aerogel with the lowest percentage of porosity and the highest particle density.

The performance of carbon aerogels in supercapacitor applications strongly depends on the preparation processes [1], i.e., the ingredients and their molar ratios, drying method, carbonization temperature, activation degree, and surface functionalization [4,5]. This is because the pore texture and surface chemistry of these materials can be controlled by modifying the above factors. Thus, the surface area, pore volumes and mean micropore width of carbon aerogel G were augmented when its degree of activation was increased to 27% burn-off, although the mean mesopore size remained unchanged (Table 4). Activation also slightly increased the oxygen content (O_{TPD}) from 0.56 % in sample G up to 0.77 % in sample G-27 [19].

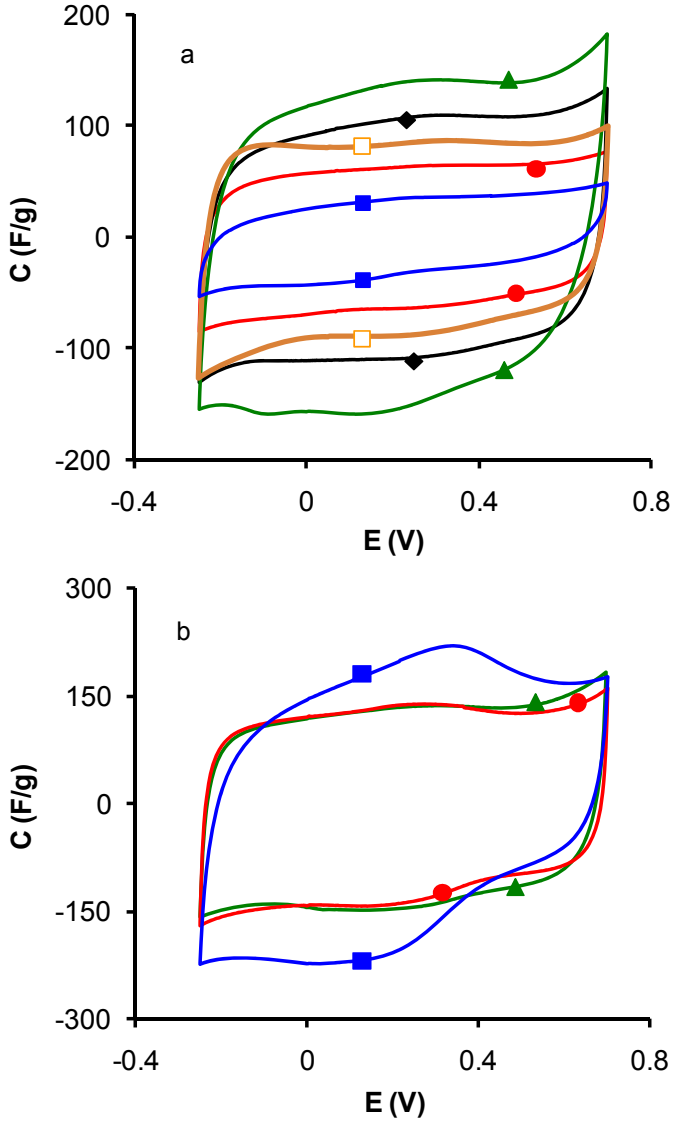

Figure 6. Cyclic voltammograms of carbon aerogels at a scan rate of 5 mV/s in 0.1 M H_2SO_4: (a) ■, I; ●, G; ◆, G-16; ▲, G-27 and □, CA3; (b) ▲, CA1; ●, CA1H and ■, CA1S.

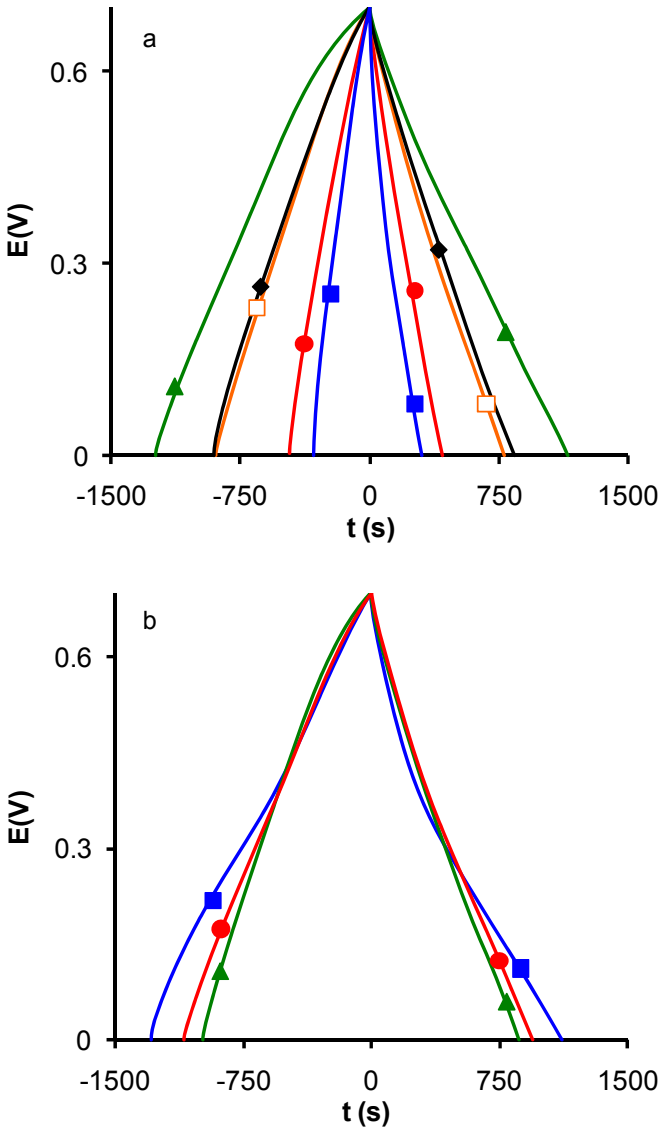

Figure 7. Chronopotentiometric curves of carbon aerogels at a scan rate of 5 mV/s in 0.1 M H_2SO_4: (a) ■, I; ●, G; ◆, G-16; ▲, G-27 and □, CA3; (b) ▲, CA1; ●, CA1H and ■, CA1S.

Table 6. Gravimetric capacitances of carbon aerogels from cyclic voltammetry (C_{CV}) at different scan rates and chronopotentiometry (C_{CP}) at 100 mA/g, and interfacial capacitance (IC_{CP})

	C_{CV} (F/g)			C_{CP} (F/g)	IC_{CP}
	0.5mV/s	1mV/s	5mV/s		($\mu F/cm^2$)
B	150	144	128	162	20
I	44	37	31	36	5
G	71	66	64	70	8
G-16	123	114	99	116	10
G-27	161	153	129	180	12
CA1	147	132	114	140	23
CA3	102	93	83	112	19
CA1H	148	141	123	150	26
CA1S	185	177	152	174	32

Variations in pore texture produced a major increase in gravimetric capacitance, from 70 to 180 F/g. Interfacial capacitance also increased but to a lesser extent, from 8 to 12 $\mu F/cm^2$ (Table 6), implying that other factors besides surface area contributed to the capacitance of these carbons. Thus, the fixation of oxygen functionalities during CO_2-activation of carbon aerogel G introduces pseudocapacitance as shown in Figure 6a, where redox humps between 0.3 and 0.4 V versus Ag/AgCl are observed with the increase in activation percentage (G-16 and G-27).

The relationship between the capacitance and surface area of differently prepared carbon gels is not always linear [36]. For instance, the gravimetric capacitance of sample G-16 was similar to that of sample CA3 (Table 6) but its S_{BET} value was two-fold higher (Table 4). Samples B and I showed similar micropore volume and mean micropore width and their surface area only differed by around 9% but the capacitance (gravimetric and interfacial) was much higher in sample B than in sample I. These differences could be the result of the surface conditions dictated from the different preparation procedures. Thus, they can develop: microporosity inaccessible to the electrolyte, specific pore size distributions, different electrical resistances (due to the different degrees of aromatization reached during the preparation of the carbon gel [36]), and different crystal orientations, among other conditions.

Interfacial capacitance of carbon aerogels linearly increased with larger porosity within the studied porosity range, as shown in Figure 8. We highlight that carbon aerogels with a particle density of 0.62-0.65 g/cm^3 and the highest interfacial capacitance (19-23 μF/cm^2) have an appropriate porosity for large electrolyte pathways and are likely to deliver adequate power and energy densities [32,37].

The fixation of surface oxygen complexes on carbon aerogel CA1 by different oxidation treatments increased the gravimetric and interfacial capacitances (Table 6) by introducing pseudocapacitance. Figure 9 shows the linear increase in IC_{CP} with higher areal oxygen concentration and with the areal concentrations of CO- and CO_2-evolving groups.

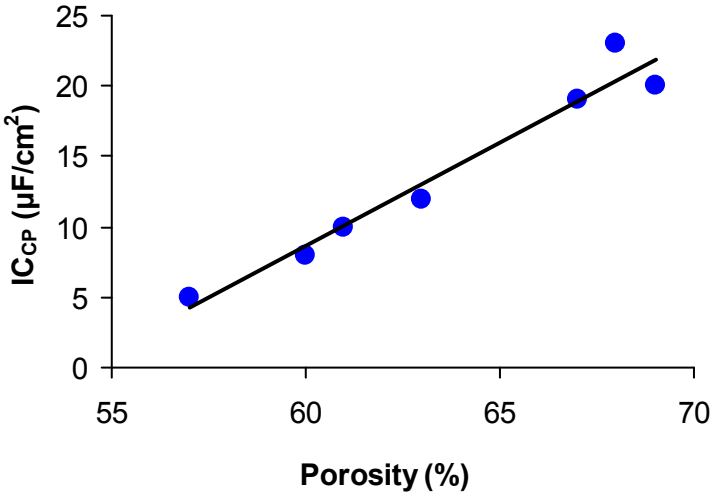

Figure 8. Interfacial capacitance *versus* porosity of carbon aerogels.

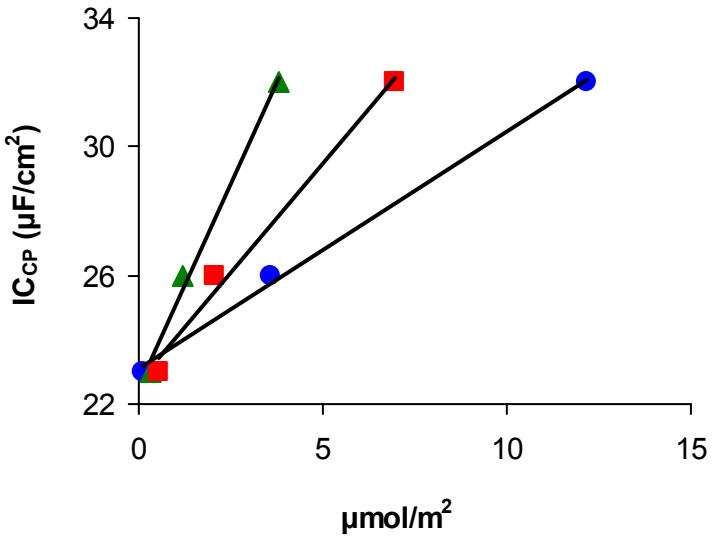

Figure 9. Relationship between interfacial capacitance and areal concentrations of oxygen, ●, and of CO- and CO_2-evolving functionalities, ■ and ▲, respectively.

5. CONCLUSIONS

Cyclic voltammogram shapes of N-doped carbon xerogels were nonrectangular due to pseudofaradaic effects attributable to the presence of surface nitrogen complexes and/or sieving effects in micropores.. The interfacial capacitance of N-doped carbon xerogels decreased with larger micropore surface area. In addition, there was a good correlation between the interfacial capacitance and the areal N_{XPS} concentration, although the best correlation was found with the areal concentration of pyridinic functionalities. The gravimetric capacitance of N-doped carbon xerogels tended to decrease with greater mean diameter of the xerogel microspheres.

Interfacial capacitance of carbon aerogels linearly increased with larger porosity within the studied porosity range. Carbon aerogels with a particle density of 0.62-0.65 g/cm^3 showed the highest interfacial capacitance 19-23 μF/cm^2. Carbon aerogel oxidation brought about a linear increase of the interfacial capacitance with the rise in the areal concentration of oxygen and with the areal concentrations of CO- and CO_2-evolving functionalities.

6. REFERENCES

1. Frackowiak E, Beguin F. Carbon materials for the electrochemical storage of energy in capacitors. Carbon 2001; 39(6):937-950.
2. Pandolfo AG, Hollenkamp AF. Carbon properties and their role in supercapacitors. J Power Sources 2006; 157(1):11-27.

3. Zhang LL, Zhao XS. Carbon-based materials as supercapacitor electrodes. Chem Soc Rev 2009; 38(9):2520-2531.

4. Bleda-Martínez MJ, Maciá-Agulló JA, Lozano-Castelló D, Morallón E, Cazorla-Amorós D, Linares-Solano A. Role of surface chemistry on electric double layer capacitance of carbon materials. Carbon 2005; 43:2677-84.

5. Bleda-Martínez MJ, Lozano-Castelló D, Morallón E, Cazorla-Amorós D, Linares-Solano A. Chemical and electrochemical characterization of porous carbon materials. Carbon 2006; 44:2642-51.

6. Hulicova-Jurcakova D, Seredych M, Lu GQ, Bandosz TJ. Combined Effect of Nitrogen- and Oxygen-Containing Functional Groups of Microporous Activated Carbon on its Electrochemical Performance in Supercapacitors. Adv Funct Mater 2009; 19(3):438-447.

7. Lota G, Grzyb B, Machnikowska H, Machnikowski J, Frackowiak E. Effect of nitrogen in carbon electrode on the supercapacitor performance. Chem Phys Lett 2005; 404(1-3):53-58.

8. Hulicova D, Yamashita J, Soneda Y, Hatori H, Kodama M. Supercapacitors Prepared from Melamine-Based Carbon. Chem Mater 2005; 17(5):1241-1247.

9. Lota G, Lota K, Frackowiak E. Nanotubes based composites rich in nitrogen for supercapacitor application. Electrochem Commun 2007; 9(7):1828-1832.

10. Seredych M, Hulicova-Jurcakova D, Lu GQ, Bandosz TJ. Surface functional groups of carbons and the effects of their chemical character, density and

accessibility to ions on electrochemical performance. Carbon 2008; 46(11):1475-1488.

11. Zhu ZH, Hatori H, Wang SB, Lu GQ. Insights into Hydrogen Atom Adsorption on and the Electrochemical Properties of Nitrogen-Substituted Carbon Materials. J Phys Chem B 2005; 109(35):16744-16749.

12. Kinoshita K. Carbon: Electrochemical and physicochemical properties. New York: Wiley; 1988, p 293.

13. Pekala RW. Organic aerogels from the polycondensation of resorcinol with formaldehyde. J Mat Sci 1989; V24(9):3221-3227.

14. Fairén-Jiménez D, Carrasco-Marín F, Moreno-Castilla C. Adsorption of benzene, toluene and xylenes on monolithic carbon aerogels from dry air flows. Langmuir 2007;23(20):10095-101.

15. Moreno-Castilla, C. Carbon gels in catalysis. In Serp P, Figueiredo JL, editors. Carbon materials for catalysis, New York: J. Wiley & Sons, 2009: Chapter 10.

16. Pekala RW, Farmer JC, Alviso CT, Tran TD, Mayer ST, Miller JM, Dunn B. Carbon aerogels for electrochemical applications. J Non-Cryst Solids 1998; 225(1):74-80.

17. Pérez-Cadenas M, Moreno-Castilla C, Carrasco-Marín F, Pérez-Cadenas AF. Surface chemistry, porous texture and morphology of N-doped carbon xerogels. Langmuir 2009;25:466-470.

18. Fairén-Jiménez D, Carrasco-Marin F, Moreno-Castilla C. Porosity and surface area of monolithic carbon aerogels prepared using alkaline carbonates and organic acids as polymerization catalysts. Carbon 2006;44(11):2301-2307.

19. Carrasco-Marín F, Fairén-Jiménez D, Moreno-Castilla C. Carbon aerogels from gallic acid-resorcinol mixtures as adsorbents of benzene, toluene and xylenes from dry and wet air under dynamic conditions. Carbon 2009;47(2):463-9.

20. Dawidziuk MB, Carrasco-Marín F, Moreno-Castilla C. Influence of support porosity and Pt content of Pt/carbon aerogel catalysts on metal dispersion and formation of self-assembled Pt-carbon hybrid nanostructures. Carbon 2009;47(11):2679-87.

21. Moreno-Castilla C, Ferro-García MA, Joly JP, Bautista-Toledo I, Carrasco-Marín F, Rivera-Utrilla J. Activated carbons surface modifications by nitric acid, hydrogen peroxide and ammonium peroxydisulfate treatments. Langmuir 1995;11(11):4386-92.

22. Eliad L, Salitra G, Soffer A, Aurbach D. Ion Sieving Effects in the Electrical Double Layer of Porous Carbon Electrodes: Estimating Effective Ion Size in Electrolytic Solutions. J Phys Chem B 2001;105(29):6880-7.

23. Hulicova D, Kodama M, Hatori H. Electrochemical Performance of Nitrogen-Enriched Carbons in Aqueous and Non-Aqueous Supercapacitors. Chem Mater 2006; 18(9):2318-26.

24. Endo M, Maeda T, Takeda T, Kim YJ, Koshiba K, Hara H, Dresselhaus MS. Capacitance and Pore-Size Distribution in Aqueous and Nonaqueous Electrolytes Using Various Activated Carbon Electrodes. J Electrochem Soc 2001;148(8):A910-A914.

25. Salitra G, Soffer A, Eliad L, Cohen Y, Aurbach D. Carbon electrodes for double layer capacitors. I. Relations between ion and pore dimensions. J Electrochem Soc 2000;147(7): 2486-93.

26. Barbieri O, Hahn M, Herzog A, Kötz R. Capacitance limits of high surface area activated carbons for double layer capacitors. Carbon 2005;43:1303-10.

27. Koh M, Nakajima T. Adsorption of aromatic compounds on CxN-coated activated carbons. Carbon 2000;38(14):1947-54.

28. Szczurek A, Jurewicz K, Amaral-Labat G, Fierro V, Pizzi A, Celzard A. Structure and electrochemical capacitance of carbon cryogels derived from phenol-formaldehyde resins. Carbon 2010;48(13):3874-83.

29. Kotz R, Carlen M. Principles and applications of electrochemical capacitors. Electrochim Acta 2000;45(15-16):2483-98.

30. Wang DW, Li F, Liu M, Lu G, Cheng HM. 3D aperiodic hierarchical porous graphitic carbon material for high-rate electrochemical capacitive energy storage. Angew Chem Int Ed 2008;47(2):373-6.

31. Kierzek K, Frackowiak E, Lota G, Gryglewicz G, Machnikowski J. Electrochemical capacitors based on highly porous carbons prepared by KOH activation. Electrochim Acta 2004;49(4):515-23.

32. Pröbstle H, Wiener M, Fricke J. Carbon aerogels for electrochemical double layer capacitors. J Porous Mat 2003;10(4):213-22.

33. Kaneko K, Ishii C, Ruike M, Kuwabara H. Origin of superhigh surface area and microcrystalline graphitic structures of activated carbons. Carbon 1992;30(7):1075-88

34. Wang X, Wang X, Liu L, Bai L, An H, Zheng L, Yi L. Preparation and characterization of carbon aerogel microspheres by an inverse emulsion polymerization. J Non-Cryst Solids 2011;357(3):793-797.

35. Fairén-Jiménez D, Carrasco-Marín F, Djurado D, Bley F, Ehrburger-Dolle F, Moreno-Castilla C. Surface area and microporosity of carbon aerogels from gas adsorption and small- and wide-angle X-ray scattering measurements. J Phys Chem B 2006;110(17):8681-8.

36. Moreno-Castilla C, Dawidziuk MB, Carrasco-Marín M, Zapata-Benabithe Z. Surface characteristics and electrochemical capacitances of carbon aerogels obtained from resorcinol and pyrocatechol using boric and oxalic acids as polymerization catalysts. **http://dx.doi.org/10.1016/j.carbon.2011.05.013**.

37. Qu D, Shi H. Studies of activated carbons used in double-layer capacitors. J Power Sources 1998; 74(1):99-107.

CHAPTER III

INFLUENCE OF SUPPORT POROSITY AND PT CONTENT OF PT/CARBON AEROGEL CATALYSTS ON METAL DISPERSION AND FORMATION OF SELF-ASSEMBLED PT-CARBON HYBRID NANOSTRUCTURES

1. ABSTRACT

Three carbon aerogels with different meso-macropore networks were used as supports for Pt catalysts using $[Pt(NH_3)_4]Cl_2$ as precursor salt. Results obtained showed mesopore volume and mean mesopore size to be important parameters that control Pt particle size and dispersion in catalysts containing 2 wt% Pt. Once the most appropriate porosity to obtain the highest dispersion was determined, the metal content was increased to 20 wt% Pt. However, the mean Pt particle size only increased from 1 to 2 nm, indicating the importance of an appropriate mesoporosity for obtaining a high dispersion at high metal loading. Mean Pt particle size was always slightly smaller by transmission electron microscopy than by H_2 chemisorption, because some Pt particles were not reduced during pre-treatment, as confirmed by X-ray photoelectron spectroscopy. Finally, transmission electron microscopy observations of catalysts with metal loading of 8-20 wt% before pre-treatment showed the formation of self-assembled Pt-carbon hybrid nanorods and nanowires. To the best of our knowledge, this is the first observation of this phenomenon in Pt/C catalysts.

2. INTRODUCTION

Carbon aerogels (CAs) can be used as supports for catalysts due to the versatility of their shape and their surface properties [1] and because they can be tailored with the appropriate characteristics by controlling the ingredients and the preparation methods [2,3]. Support pore texture is one of the most important properties controlling the dispersion and metal particle size. Thus, when activated

carbon-supported Pt catalysts prepared with $H_2[PtCl_6].6H_2O$ to yield around 1 wt% Pt metal loading were reduced in H_2 flow at 400 ºC, the Pt dispersion depended on the number of pores with diameter between 9 and 11 nm [4].

The use of activated carbons as supports has two main drawbacks: they are generally microporous with a poorly developed mesoporosity; and they contain a variable amount of mineral matter, which can influence the behaviour of the metal catalyst. In contrast, CAs can be designed with a homogeneous and well-developed mesoporosity and with a high level of purity.

CA-supported Pt catalysts prepared by different methods have been characterized and used in various reactions [1,5-12]. Saquing et al. [5] prepared two Pt/CA nanocomposites with different total pore volumes using a supercritical deposition method, varying the Pt content between 10 and 40%. One catalyst containing 40 wt % Pt yielded the same mean Pt particle size (around 3 nm) as that containing 30 wt % Pt but with a different support. The authors attributed this result to the higher pore volume of the former, but did not describe any other pore texture characteristics of the supports. They also indicated that the metal loading may influence the particle size, which increased from around 1 to 3 nm when the Pt content rose from 10 to 40 wt %.

Marie et al. [8] used two CAs with high pore volumes and surface area and different pore-size distributions to prepare a Pt catalyst containing 30 wt % Pt. Pore sizes that contributed to the pore volume were 50-60 nm in one CA and 30-38 nm in the other. CA-supported Pt catalysts were prepared using anionic or cationic Pt precursors; the surface area of Pt deposited was similar between the

supports, therefore the pore texture of the supports had no influence on the Pt dispersion.

Du et al. [9] used five CAs as supports for Pt catalysts, prepared by reducing $H_2[PtCl_6]$ with ethylene glycol in a suspension that contained the CA. They reported that the pore structure had no influence on the Pt particle size (around 3 nm) or dispersion but that the activity of the catalysts in the oxygen reduction reaction increased with larger mean mesopore size.

According to the above findings, the effect of the CA porosity on Pt dispersion has yet to be elucidated. Therefore, the objective of the present study was to clarify the influence of the pore texture of CAs on Pt particle size and dispersion when they are used as supports. After establishing the most appropriate porosity to yield a high dispersion for catalysts containing 2 wt % Pt, the effect of Pt metal loading on Pt dispersion was also investigated. During characterization of some of the supported catalysts before pre-treatment by high-resolution transmission electron microscopy (TEM), we incidentally detected the formation of self-assembled Pt-carbon hybrid nanorods and nanowires without the assistance of a surfactant or a template. To the best of our knowledge this is the first time that these nanostructures have been found in Pt catalysts supported on carbons.

3. EXPERIMENTAL

This study used three CAs, referred to hereafter as CA1, CA2 and CA3. They were prepared by carbonizing the organic aerogels obtained from the

polymerization reaction of resorcinol (0.112 mol) and formaldehyde (0.224 mol), using Na_2CO_3 (1.4 x 10-4 mol) as catalyst. Ingredients were dissolved in water (27 mL) for sample CA1, in a water-methanol mixture (24-3 mL) for sample CA2, and in a water-tetrahydrofurane mixture (24-3 mL) for sample CA3. Mixtures were stirred to obtain a homogeneous solution that was cast into glass moulds (45 cm length x 0.5 cm i.d.). The glass moulds were sealed and the mixture was cured using a previously reported method [13]. After curing, the gel rods were cut into 5 mm pellets, the solvent was exchanged with acetone and the pellets were dried with supercritical CO_2. Organic aerogels so obtained were carbonized at 950 ºC in N_2 flow (100 cm^3/min) at a heating rate of 1.5 ºC/min and with a soaking time of 5 h. A portion of CA1 was oxidized with $(NH_4)_2S_2O_8$ (CA1S), as described elsewhere [14].

Supported Pt catalysts were prepared by impregnation of CAs with an aqueous solution of $[Pt(NH_3)_4]Cl_2$ to yield Pt catalysts containing between 2 and 20 wt% Pt, referred to by adding the Pt content to the name of the carbon aerogel. Total metal content of supported catalysts was obtained by burning them off at 800 ºC in air and weighing the residue.

Characterization of samples was carried out by the following methods: N_2 and CO_2 adsorption at –196 and 0º C, respectively; mercury porosimetry; temperature programmed desorption (TPD) coupled with mass spectrometry; immersion calorimetry; determination of pH of the point of zero charge (pH_{PZC}); H_2 chemisorption at 25 ºC; TEM and X-ray photoelectron spectroscopy (XPS).

Adsorption isotherms were measured with an Autosorb 1 from Quantachrome after outgassing samples overnight at 110 ºC under high vacuum (10^{-6} mbar). N_2 adsorption isotherms were analyzed by BET equation, from which the surface area, S_{BET}, was obtained.

In addition, the Dubinin-Radushkevich (DR) equation (1) was applied to N_2 and CO_2 adsorption isotherms at -196 and 0 ºC, respectively,

$$W = W_0 \exp\left[\left(-\frac{A}{\beta E_0}\right)^2\right] \qquad (1)$$

where W is the amount absorbed at relative pressure p/p_0; W_0 is the limiting value filling the micropores; A is the differential molar work given by $A = RT \ln P_0 / P$; β is the affinity coefficient, taken to be 0.33 and 0.35 for N_2 and CO_2, respectively, and E_0 is the characteristic adsorption energy. N_2 and CO_2 molar volumes were taken to be 34.65 and 43.01 cm^3/mol, respectively [15].

Once the E_0 value was known, the mean micropore width, L_0, was obtained by applying the Stoeckli equation (2) [16].

$$L_0\ (nm) = \frac{10.8}{E_0 - 11.4\ (kJ/mol)} \qquad (2)$$

Mercury porosimetry was performed up to a pressure of 4200 kg/cm^2 using Quantachrome Autoscan 60 equipment. This technique yielded the following parameters: pore volume corresponding to pores with a diameter between 3.7 and 50 nm, V_2, referred to as mesopore volume, although it should be noted that mesopore volume range is classically defined as 2 - 50 nm [17]; volume of pores

with a diameter greater than 50 nm, or macropore volume, V_3, and particle density, ρ.

TPD was carried out by heating the samples to 1000 ºC at 10 ºC/min and analyzing the CO and CO_2 evolved by means of a model Prisma mass spectrometer from Pfeiffer. The oxygen content, O_{TPD}, was calculated from the amount of CO and CO_2. The immersion enthalpy into benzene and water, $\Delta_i H_{benz}$ and $\Delta_i H_{water}$, respectively, were obtained in a model C80-D Setaram calorimeter. Samples were previously outgassed overnight under dynamic vacuum of 10^{-6} mbar at the sample location and at 120 ºC. Measurements were made at least twice for each sample. The pH_{PZC} was determined as reported elsewhere [14].

Before their characterization by H_2 chemisorption, TEM or XPS, catalysts were pre-treated at 400 ^oC in He flow for 12 h or in He flow for 8 h and subsequently in H_2 flow for 4 h. H_2 chemisorption isotherms were measured in conventional volumetric equipment made of Pyrex glass and free of mercury and grease, which reached a dynamic vacuum better than 10^{-6} mbar at the sample location. Equilibrium pressure was measured with a Baratron transducer from MKS. A 0.250-g sample of the supported catalyst was pre-treated as described above and outgassed at 400 ^oC for 1 h. Subsequently, it was cooled down to 25 ^oC and a H_2 adsorption isotherm was measured between 70 and 350 mbar. H_2 uptake was determined from the intercept of the linear adsorption isotherm [18]. Platinum dispersion, D, and its average particle size, dH_2, were obtained from the H_2 uptake, assuming that one H atom was chemisorbed by one surface Pt atom and that $dH_2(nm)=1.08/D$.

TEM was carried out with Philips electron microscope equipment, model CM-20, at magnification of 600,000 X. Pre-treated and non- pre-treated catalysts were suspended in ethanol and sonicated for 10 min. The suspended catalyst particles were deposited on a carbon-coated copper grid that was introduced several times into the suspension, "fishing" the particles. Micrographs obtained were analysed by an image programme from which the Pt particle size distribution, PSD, and mean Pt particle size, d_{TEM}, were obtained.

XPS measurements were made with an ESCA 5701 from Physical Electronics equipped with MgKα X-ray source ($h\nu$ = 1253.6 eV) and hemispherical electron analyser. Samples analysed by XPS were those previously used for H_2 chemisorption. A base pressure of 10^{-9} mbar was maintained during data acquisition. The spectra obtained after background signal correction were fitted to Lorentzian and Gaussian curves, using the peak of C_{1s} at 284.6 eV as internal standard.

4. RESULTS AND DISCUSSION

4.1. Characteristics of the supports

Mercury porosimetry curves obtained with CAs are depicted in Figure 1 and the results are shown in Table 1. These curves show that there was no volume variation during depressurization. The shape of mercury intrusion curves may indicate that CAs are densified under application of isostatic pressure. To test this possibility, it is recommended [19] to weigh the samples before and after the mercury porosimetry run to determine the mercury remaining within the pore

network after depressurization. This volume, V_R, agreed with the total pore volume (V_2 + V_3) obtained from the intrusion curves (Table 1). Therefore, the mercury porosimetry data corresponded to the irreversible intrusion of the CAs into the meso- and macropores and not to a compression of the material under isostatic pressure.

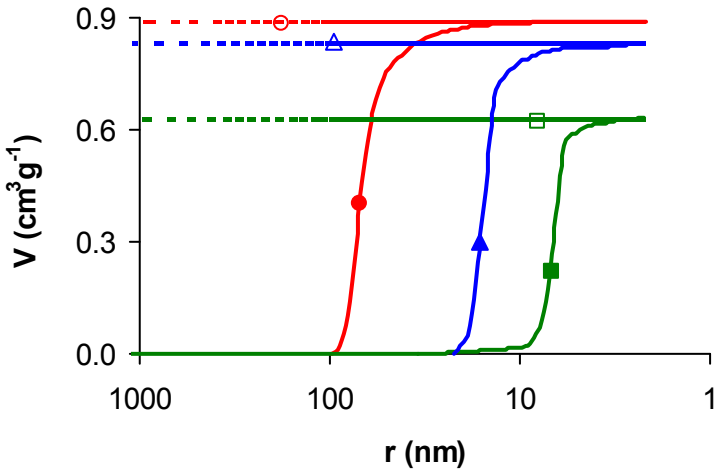

Figure 1. Intrusion-extrusion curves from mercury porosimetry. CA1, △; CA2, □; CA3, ○. Symbols on curves are only to identify the sample. Intrusion, closed symbol; extrusion, open symbol.

Results given in Table 1 show that CA1 and CA2 were mesoporous materials, whereas CA3 was macroporous. Pore size distributions in the meso-macropore range were monomodal (Figure 2). The mean pore diameter, d_p, from the maximum of the distribution is given in Table 1, indicating that CA1 had wider mesopores than CA2. The monolith density was highest in CA2 because its (V_2 + V_3) pore volume was the lowest.

Table 1. Mesopore (V_2) and macropore (V_3) volumes, mean pore width (d_P) and density (ρ) of carbon aerogels from mercury porosimetry

	CA1	CA2	CA3
V_3 (cm^3/g)	0.00	0.02	0.91
V_2 (cm^3/g)	0.86	0.61	0.03
V_R (cm^3/g)*	0.85	0.64	0.94
d_p (nm)	33	13	148
ρ (g/cm^3)	0.64	0.82	0.65

* Volume of mercury remaining in the porosity after depressurization

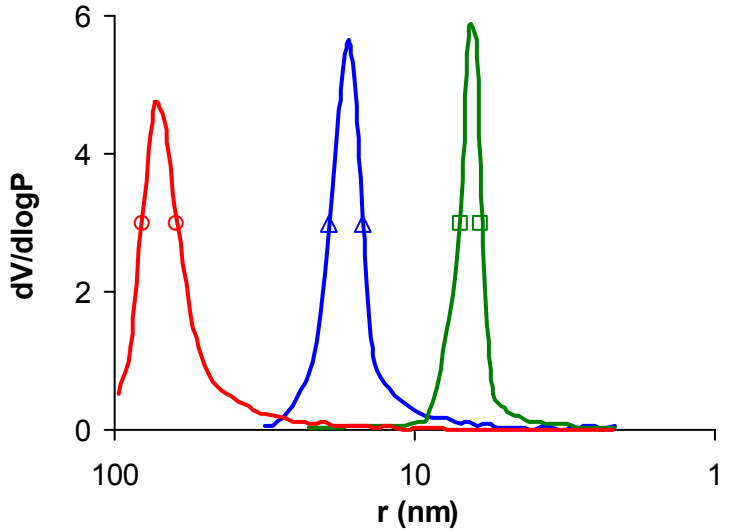

Figure 2. Pore size distribution from mercury porosimetry. CA1, △; CA2, □; CA3, ○.

Figures A.II.1 and A.II.2 in Appendix II show the N_2 at -196 °C and CO_2 at 0 °C isotherms respectively. Table 2 lists the surface area and microporosity of the CAs and Table 3 shows their surface chemistry. The CAs had a medium surface area value, with a S_{BET} ranging from 592 to 700 m^2/g. The micropore volume obtained from CO_2 adsorption at 0 ºC yields the volume of narrow micropores (below about 0.7 nm width), whereas the total micropore volume is obtained from N_2 adsorption at -196 ºC if there are no constrictions at micropore entrances [15]. The value of $W_0(N_2)$ was slightly higher or similar to $W_0(CO_2)$, indicating an absence of micropore constrictions. Total micropore volume of sample CA2 was somewhat higher versus the other two supports, increasing its surface area value. However the average micropore width was similar in all samples at between 0.7 and 0.8 nm.

Table 2. BET surface area (S_{BET}), micropore volume (W_0), mean micropore width (L_0), heat of immersion into benzene ($\Delta_i H_{benz}$) and surface area accesible to benzene (S_{benz}) of carbon aerogels

	CA1	CA2	CA3	CA1S
S_{BET} (m^2/g)	618	700	592	544
$W_0(N_2)$ (cm^3/g)	0.26	0.29	0.26	0.23
$L_0(N_2)$ (nm)	0.80	0.83	0.76	0.79
$W_0(CO_2)$ (cm^3/g)	0.24	0.25	0.26	0.22
$L_0(CO_2)$ (nm)	0.61	0.62	0.60	0.53
$\Delta_i H_{benz}$ (J/g)	84.5	91.0	71.9	73.8
S_{benz} (m^2/g)	741	798	631	647

The S_{BET} value of CA1 was diminished by the oxidation to obtain CA1S. This reduction in surface area is a consequence of the fixation of surface oxygen complexes (Table 3) at the micropore entrances, giving rise to a narrowing of the smaller micropores, as can be seen from the $L_0(CO_2)$ values of the oxidized versus original CA1 samples.

Table 3. Surface chemistry of carbon aerogels. Amounts of CO and CO_2 evolved after heating at 1000 ºC in He flow. Total (O_{TPD}) and surface (O_{XPS}) oxygen content. Heat of immersion into water ($\Delta_i H_{water}$) and $\Delta_i H_{water}/\Delta_i H_{benz}$ ratio. pH at the point of zero charge (pH_{PZC})

	CA1	CA2	CA3	CA1S
CO (mmol/g)	0.34	0.13	0.19	3.78
CO_2 (mmol/g)	0.10	0.06	0.11	1.43
O_{TPD} (%)	0.85	0.42	0.66	10.64
O_{XPS} (%)	4.14	4.22	4.24	11.60
$\Delta_i H_{water}$ (J/g)	40.0	nd*	41.1	65.7
$\Delta_i H_{water}/\Delta_i H_{benz}$	0.47	nd	0.57	0.89
pH_{PZC}	8.0	nd	nd	2.0

* nd = not determined

The enthalpy of immersion into benzene was converted into a surface area value (S_{benz}) following the method proposed by Denoyel el al [20] and other authors [21-23], taking account of the enthalpy of immersion into benzene of a non porous carbon black, 0.114 J/m^2 [20]. The minimal dimension [23] of N_2 (0.36 nm) and benzene (0.37 nm) is almost the same, therefore they would have access to the same slit-shape micropore range. However, the S_{BET} is sometimes

underestimated, because part of the microporosity is so narrow that a molecular layer of N_2 cannot be accommodated on each micropore wall. In contrast, benzene molecules interact with both micropore walls in the immersion method, yielding a high surface area value. The S_{benz} values obtained are compiled in Table 2. They were slightly higher than S_{BET} in all samples, indicating the presence of some narrow micropores.

Figures A.II.3 and A.II.4 of Appendix II show the TPD profiles for carbon aerogels, Table 3 shows the amounts of CO and CO_2 evolved from CAs when heat-treated to 1000º C, from which the total oxygen content, O_{TPD}, was calculated. This Table also reports the total oxygen content from XPS, which is known to give the surface composition of a solid up to a depth of 2-3 nm. Therefore, the O_{XPS} value gives the oxygen content of the outer surface of the solid. O_{XPS} was greater than O_{TPD} in all samples except for CA1S, indicating that most of the surface oxygen complexes were located on the outer surface of the CAs. This has been observed in many other carbon materials as a consequence of exposure to the atmosphere. The strong oxidant used to prepare CA1S provided an uniform oxidation of the outer and inner surface of the CA1 support, therefore they had similar oxygen contents. Oxidation of CA1 produced a decrease in the pH_{PZC} (Table 3), making the CA1S acidic.

The surface hydrophobicity of a carbon material decreases when its oxygen content increases. In this study, the surface hydrophobicity of CAs was determined by the $\Delta_i H_{water}/\Delta_i H_{benz}$ ratio. The immersion enthalpy into benzene is assumed to be proportional to the surface area accessible to the wetting liquid, whereas the immersion enthalpy into water depends on both the surface area

accessible to the liquid and the surface oxygen complexes. Results obtained show that CA1S has a $\Delta_i H_{water}/\Delta_i H_{benz}$ ratio higher than CA1, indicating a reduction in the hydrophobicity of the CA1 carbon surface after its oxidation.

4.2. Characteristics of the supported catalysts with 2 wt% Pt loading

A TEM micrograph of CA1-2Pt catalyst before pre-treatment is depicted in Figure 3, as an example, and shows that catalysts with 2 wt% metal loading before pre-treatment contained small and well-dispersed rounded Pt nanoparticles.

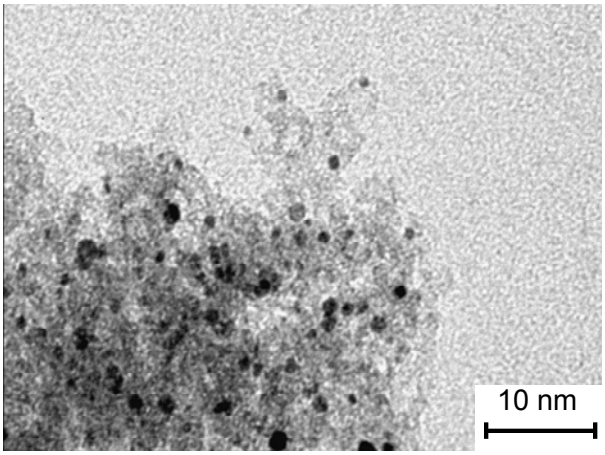

Figure 3. Transmision electron microscopy picture of the CA1-2Pt catalyst before pre-treatment.

When activated carbon-supported Pt catalysts are prepared using $[Pt(NH_3)_4]Cl_2$ as metal precursor, they cannot be pre-treated directly in H_2 flow at 400 ºC because a very low dispersion is obtained, due to the formation of $[Pt(NH_3)_2H_2]$, an unstable and mobile intermediate hydride that produces an

agglomeration of the Pt particles. Instead, the catalyst is preferentially pre-treated under He flow at 400 ºC, which produces a gradual decomposition of the amino complex leading to metallic Pt [4,18].

Figure 4 shows PSDs after He pre-treatment at 400 ºC. CA1-2Pt showed the narrowest PSD, followed by CA2-2Pt. CA1 and CA2 were micro-mesoporous, but CA1 had a higher mesopore volume and a wider mean mesopore size than CA2 (33 nm vs. 13 nm). These support characteristics make dH_2 and d_{TEM} values (Table 4) lower in CA1-2Pt than in CA2-2Pt. Interestingly, the highest dispersion for Pt catalysts supported on carbon xerogels [24] was obtained using a carbon xerogel with large mesopores (40 nm), suggesting that this may be the optimal mesopore size to obtain a high Pt dispersion. These results seem to indicate that below around 33-40 nm in size, the Pt clusters formed in the pores during pre-treatment are so close that they can sinter, reducing the final dispersion.

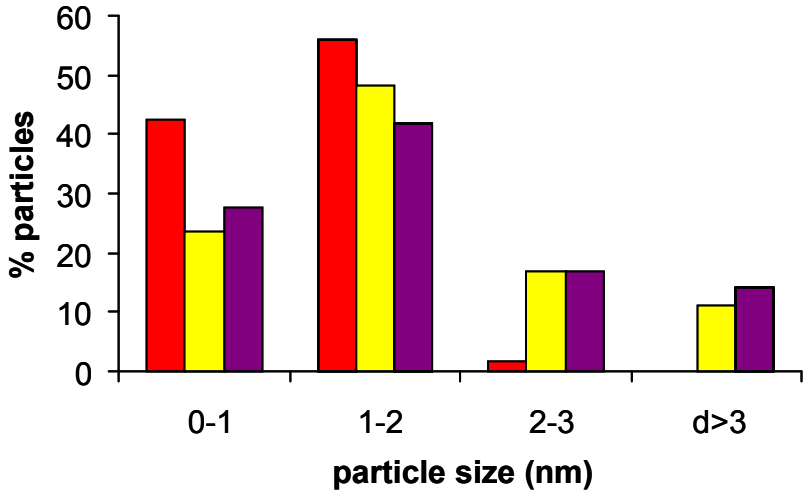

Figure 4. Particle size distribution of catalysts CA1-2Pt, ; CA2-2Pt, ; CA3-2Pt, after He pre-treatment at 400 ºC for 12 h.

By contrast, a wider PSD was obtained with CA3-2Pt catalyst, which had the highest dH_2 and d_{TEM} values. The support in this case was a micro-macroporous carbon aerogel. Although macropores can facilitate the impregnation, they can also enhance the sintering of the Pt particles, likely because the mobility of Pt particles during the pre-treatment is not as restricted as it could be in pores in the range of 33-40 nm in size.

Table 4. Mean Pt particle size (d) and dispersion (D) from H_2 chemisorption and TEM after He pre-treatment of catalysts at 400 ºC for 12h

	CA1-2Pt	CA2-2Pt	CA3-2Pt
dH_2(nm)	1.8	2.1	3.8
d_{TEM}(nm)	1.3	1.6	2.9
DH_2 (%)	60	51	28
D_{TEM} (%)	83	68	37

The effect of the mesopore volume of the carbon support on Pt dispersion is depicted in Figure 5, showing that the mean Pt particle size linearly decreased when the mesopore volume of the support increased.

The d_{TEM} values in Table 4 were always slightly smaller than the dH_2 values. The same trend was found in all studied samples (see below). This difference was also observed by Saquing et al [5] but they offered no explanation. We believe that it might be because some surface Pt atoms did not chemisorb H_2, likely because the He pre-treatment did not reduce them all to the metallic state.

The $Pt_{4f7/2}$ core level deconvoluted spectra of the CA1-2Pt catalysts before and after He pre-treatment are depicted in Figure 6, as an example, the corresponding spectra for pre-treated catalysts CA2-2Pt and CA3-2Pt are presented in Figure A.II.5 of Appendix II. All catalysts before pre-treatment showed only one peak, at a binding energy (BE) of 72.1 eV, which is assigned in the literature [25] to an intermediate oxidation state between Pt(0) and Pt(II). The spectra of He pre-treated catalysts showed two peaks at BEs of 71.6 and 73.0 eV and are compiled in Table 5 alongside their corresponding percentages. The peak at 71.6 eV can be assigned to Pt(0), although this value ranges from 71.0 to 71.5 eV in the literature [10,26,27]. The shift to a higher binding energy in our He pre-treated catalyst may be due to electronic effects of very small and highly dispersed Pt particles present on the activated carbon. Finally, the peak at 73.0 eV can be assigned to Pt(II) [10,26,27].

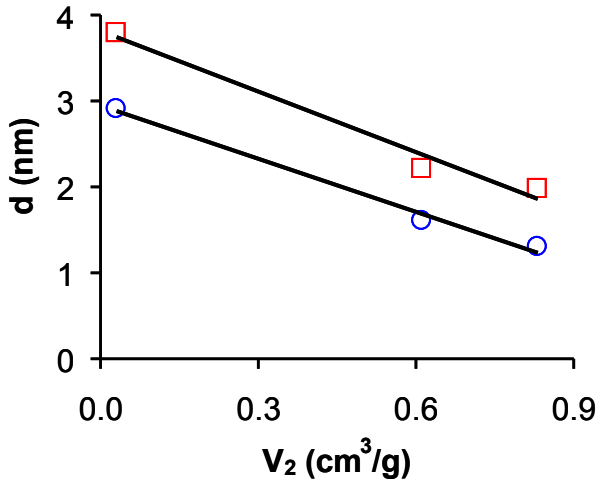

Figure 5. Relationship between mean Pt particle size and mesopore volume of the support; dH_2, □; d_{TEM}, ○.

Results obtained indicate that He pre-treatment of catalysts at 400 ºC did not completely reduce Pt(II) to the metallic state, which may explain the above-commented difference between dH_2 and d_{TEM}. The variation in peak percentage at a BE of 71.7 eV indicates that the reduction of Pt(II) to Pt(0) was lesser as the Pt particle size increased. In addition, the Pt_{XPS}/Pt_{Total} ratio decreased when Pt dispersion also diminished, due to the rise in bulk versus surface Pt atoms with the increase in Pt particle size.

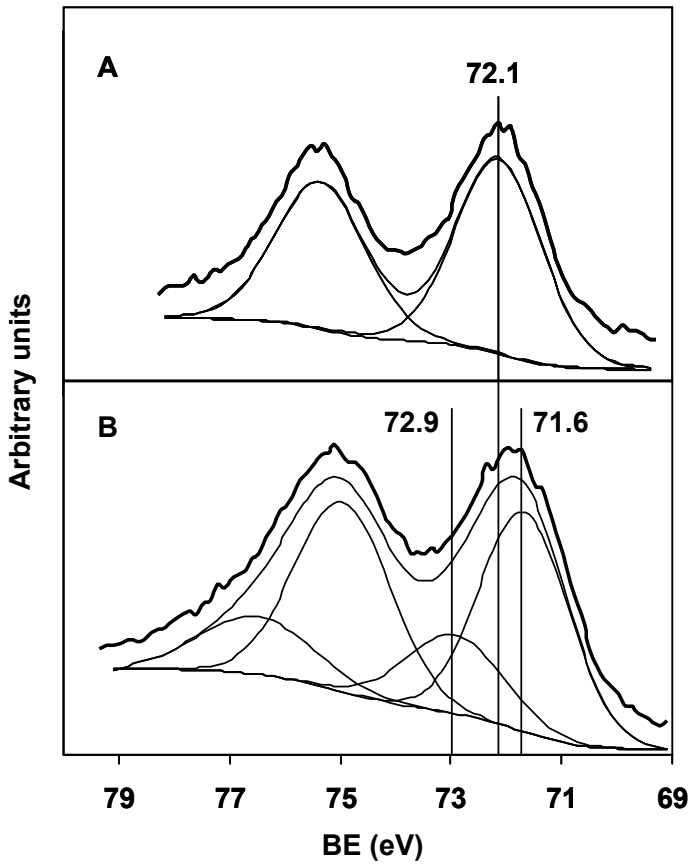

Figure 6. X-ray photoelectron spectroscopy profiles of the Pt_{4f} region for catalyst CA1-2Pt: A, before and B, after pre-treatment in He at 400 ºC for 12 h.

Table 5. Results of deconvoluting the $Pt_{4f7/2}$ component of the XPS profile after He pre-treatment of catalysts at 400 ºC for 12h . Binding energy (BE) of the peaks in eV, percentage of the peaks and surface to total Pt ratio (Pt_{XPS}/Pt_{Total})

Catalyst	BE	Percentage	BE	Percentage	Pt_{XPS} (wt.%)	Pt_{XPS}/Pt_{Total}
CA1-2Pt	71.6	77	72.9	23	2.0	1.0
CA2-2Pt	71.6	65	73.0	35	1.1	0.6
CA3-2Pt	71.6	59	72.9	41	0.6	0.3

4.3. Characteristics of the supported catalysts with a Pt loading higher than 2 wt%

The CA1 support was selected to prepare Pt catalysts with higher Pt contents (up to 20 wt %), because it showed the most appropriate mesoporosity to give a high Pt dispersion. Some TEM micrographs of catalysts before pre-treatment are depicted in Figure 7, as an example. These images were unexpected, since they showed the formation of self-assembled Pt-carbon hybrid nanorods and nanowires instead of the individual rounded particles found with catalysts containing 2 wt% Pt before pre-treatment. Hence, these nanostructures only appeared at high metal loading and were very abundant at 20 wt% Pt. Nanoparticle assemblies are of great interest for fundamental and applied research and have attracted considerable attention in recent years [28-37].

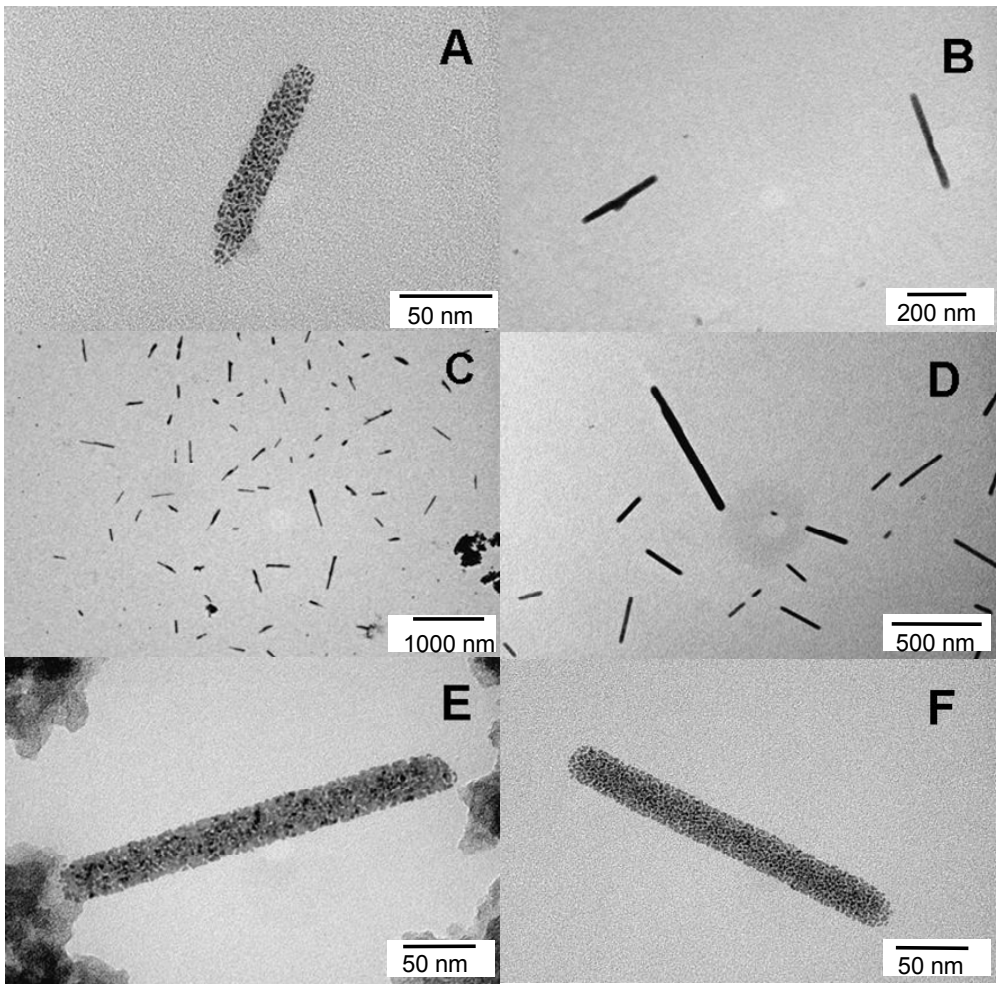

Figure 7. Transmission electron microscopy picture of catalysts before pre-treatment: (A) CA1-8Pt; (B) CA1-14Pt and (C, D, E and F) CA1-20Pt.

Pt-carbon hybrid nanorods and nanowires were formed when the solvent (ethanol) containing the dispersed catalyst nanoparticles was evaporated on the TEM grid. The formation of rods, wires and ring nanostructures has been

reported [29,30,31,37] when Ag and Au nanoparticles suspended in an organic solvent were deposited on a solid substrate. However, to the best of our knowledge, this is the first observation of the formation of Pt-carbon hybrid nanorods and nanowires without the assistance of a surfactant or template.

Notably, the nanorods and nanowires were not formed after heating the catalysts above 200 ºC in He flow. Hence, they disappeared when the $[Pt(NH_3)_4]Cl_2$ was decomposed. The influence of the surface chemistry of the support on the formation of these nanostructures was determined by using the CA1S support to prepare a supported catalyst containing 14 wt% Pt. The surface chemistry of CA1S differs from that of CA1, being more acidic and hydrophilic the former support. TEM micrographs obtained with CA1S-14Pt before pre-treatment are depicted in Figure 8, as an example, showing that nanorod and nanowire formation was not affected by variations in the surface chemistry of the support due to an increase in surface oxygen complexes.

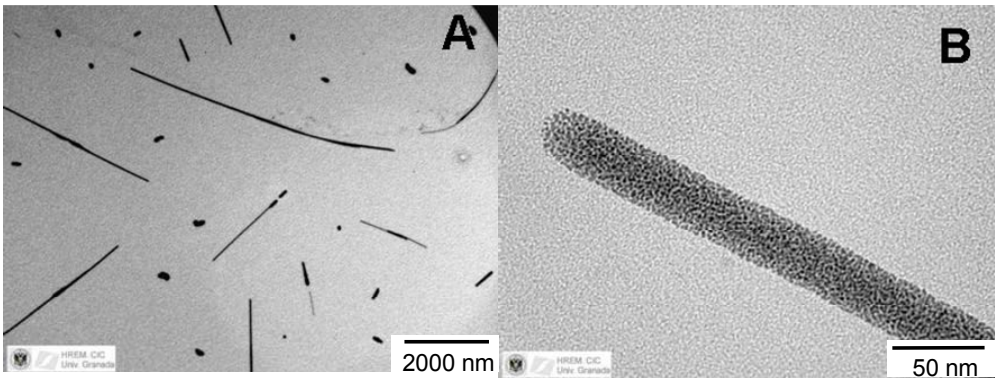

Figure 8. Transmision electron microscopy picture of catalyst CA1S-14Pt before pre-treatment.

XPS studies showed only one peak at 72.1 eV for the catalysts before pre-treatment that were prepared with the CA1 support, whereas this peak was shifted to 73.1 eV when CA1S was used. Therefore the oxidized support prevented the partial reduction of Pt(II) during preparation of the catalysts, indicating that the formation of nanostructures was not due to changes in the oxidation state of Pt, as has been reported in other systems [32].

Formation of these self-assembled nanostructures would be determined by different forces that are, combined together, sufficient to overcome the entropy loss caused by ordering [37]. However, the formation mechanism of these self-assembled nanostructures is not yet understood, and our group is currently studying the nature of the interactions responsible.

Catalysts supported on CA1 were pre-treated in He flow at 400 ºC or alternatively in He and H_2 flow at 400 ºC. This latter treatment was carried out in an attempt to increase the percentage reduction of Pt(II). Similar PSDs were obtained after both pre-treatments, and those after the He-H_2 pre-treatment are shown in Figure 9 as an example. Most of the Pt particles were below 2 nm and their contribution decreased when the metal content of the supported catalysts increased.

Table 6 shows the mean Pt particle size and dispersion results obtained after the two pre-treatments. The $Pt_{4f7/2}$ XPS profile of all samples also showed two peaks at 71.6 eV and 73.1-73.2 eV, corresponding to Pt(0) and Pt(II), respectively. Percentages of both Pt species and the Pt_{XPS}/Pt_{Total} ratio are compiled in Table 7.

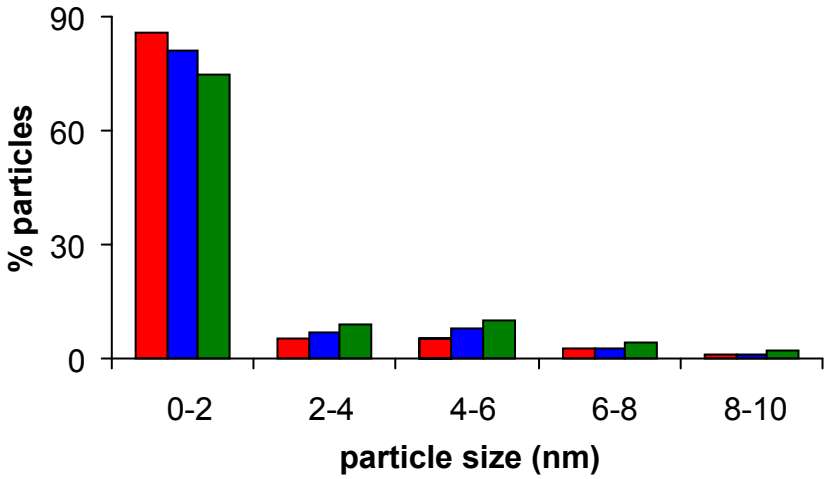

Figure 9. Particle size distribution of catalysts CA1-8Pt, ■; CA1-14Pt, ■ and CA1-20Pt, ■ after He-H_2 pre-treatment at 400 ºC for 12 h.

Table 6. Mean Pt particle size (d in nm) and dispersion percentage (D) from H_2 chemisorption and TEM after He and He-H_2 pre-treatments of catalysts at 400 ºC for 12 h

Catalyst	He pre-treatment				He-H_2 pre-treatment			
	dH_2	d_{TEM}	DH_2	D_{TEM}	dH_2	d_{TEM}	DH_2	D_{TEM}
CA1-2Pt	1.8	1.3	60	83	1.3	1.1	83	98
CA1-8Pt	2.0	1.5	54	72	1.6	1.3	67	83
CA1-14Pt	2.8	1.7	39	64	2.0	1.5	54	72
CA1-20Pt	3.1	2.9	34	37	2.3	1.9	47	57

Table 7. Percentage of the components of the deconvoluted XPS profiles after He and He-H_2 pre-treatments of catalysts at 400 ºC for 12h and surface to total Pt ratio (Pt_{XPS}/Pt_{Total})

Catalyst	He pre-treatment			He-H_2 pre-treatment		
	71.6 eV	73.2 eV	Pt_{XPS}/Pt_{Total}	71.7 eV	73.4 eV	Pt_{XPS}/Pt_{Total}
CA1-2Pt	77	23	1.0	81	19	0.8
CA1-8Pt	75	25	0.8	81	19	0.7
CA1-14Pt	74	26	0.8	79	21	0.7
CA1-20Pt	71	29	0.8	79	21	0.7

It is noteworthy that a ten-fold increase in the metal content of the catalysts only produced around a two-fold increase in mean Pt particle size. These results demonstrate the importance of an appropriate mesopore network for obtaining very small Pt nanoparticles, even at high Pt contents. The smallest mean Pt particle size (around 1 to 2 nm) was obtained after the He-H_2 pre-treatment, when the Pt content increased from 2 to 20%. Hence, the CA1-2Pt catalyst showed nearly atomic dispersion.

After both pre-treatments, all samples showed somewhat higher dH_2 than d_{TEM} values. However, this difference was smaller after the He-H_2 pre-treatment because of a larger reduction of Pt(II) to Pt(0) due to the longer exposure to H_2 flow (Table 7). In addition, the percentage reduction decreased with the increase in Pt content of the catalyst, although this reduction was very slight after the He-H_2 pre-treatment.

5. CONCLUSIONS

This study demonstrates that the mesopore volume and mean mesopore size are both very important surface characteristics of carbon aerogels to obtain a high dispersion for Pt catalysts with a 2 wt% metal loading and prepared from $[Pt(NH_3)_4]Cl_2$ as precursor salt. Thus, the highest dispersion was obtained with a carbon aerogel that had a mean mesopore diameter of 33 nm. Although the Pt content increased ten-fold (from 2 to 20 wt%), the mean Pt particle size increased only two-fold (from 1 to 2 nm). These results underline the importance of an appropriate mesopore network for obtaining very small Pt particles, even at high Pt loading.

After pre-treatment of the catalysts in He flow at 400 ºC for 12 h, the average Pt particle size obtained by TEM was slightly smaller than that obtained from H_2 chemisorption. The same phenomenon, although to a smaller degree, was found when the pre-treatment was carried out in He and H_2 flow. Therefore, the difference between the two methods of Pt particle size determination may be due to a greater reduction of Pt(II) to Pt(0) after He-H_2 pre-treatment. This proposition was confirmed by XPS findings.

Finally, TEM images of non pre-treated catalysts with a Pt content between 8 and 20 wt% showed the formation of self-assembled Pt-carbon hybrid nanorods and nanowires. These nanostructures were formed after solvent evaporation of the suspension deposited on the TEM grid. They were also formed when the support was oxidized to increase its oxygen content, hydrophylicity and surface acidity. However, they were not observed when the Pt precursor salt was decomposed. To the best of our knowledge, this is the first observation of the

formation of Pt-carbon hybrid nanorods and nanowires without the assistance of a surfactant or template.

6. REFERENCES

[1] Moreno-Castilla C, Maldonado-Hódar FJ. Carbon aerogels for catalysis applications: an overview. Carbon 2005; 43(3): 455-65.

[2] Pekala RW, Kong FM. Resorcinol-formaldehyde aerogels and their carbonized derivatives. Polym. Prep. 1989; 30: 221-3.

[3] Al-Muhtaseb SA, Ritter JA. Preparation and properties of resorcinol-formaldehyde organic and carbon gels. Adv Mater 2003; 15: 101-14.

[4] Rodríguez-Reinoso F, Rodríguez-Ramos I, Moreno-Castilla C, Guerrero-Ruiz A, López-González JD. Platinum catalysts supported on activated carbon. I Preparation and characterization. J Catal 1986; 99(1): 171-83.

[5] Saquing CD, Cheng TT, Aindow M, Erkey C. Preparation of platinum/carbon aerogel nanocomposites using a supercritical deposition method. J Phys Chem B 2004; 108: 7716-22.

[6] Marie J, Berthon-Fabry S, Achard P, Chatenet M, Pradourat A, Chainet E. Highly dispersed platinum on carbon aerogels as supported catalysts for PEM fuel cell-electrodes: comparison of two different synthesis paths. J Non-Cryst Solids 2004; 350: 88-96.

[7] Smirnova A, Dong X, Hara H, Vasiliev A, Sammes N. Novel carbon aerogel-supported catalysts for PEM fuel cell application. Int J Hydrogen Energ 2005; 30(2): 149-58.

[8] Marie J, Berthon-Fabry S, Chatenet M, Chainet E, Pirard R, Cornet N, et al. Platinum supported on resorcinol-formaldehyde based carbon aerogels for

PEMFC electrodes: Influence of the carbon support on electrocatalytic properties. J Appl Electrochem 2007; 37: 147-53.

[9] Du H, Gan L, Li B, Wu P, Qiu Y, Kang F, et al. Influences of Mesopore Size on Oxygen Reduction Reaction Catalysis of Pt/Carbon Aerogels. J Phys Chem C 2007; 111(5): 2040-3.

[10] Kim HJ, Kim WI, Park TJ, Park HS, Suh DJ. Highly dispersed platinum-carbon aerogel catalyst for polymer electrolyte membrane fuel cells. Carbon 2008; 46(11): 1393-400.

[11] Maldonado-Hódar FJ, Moreno-Castilla C, Pérez-Cadenas AF. Catalytic combustion of toluene on platinum-containing monolithic carbon aerogels. Appl Catal B 2004; 54(4): 217-24.

[12] Padilla-Serrano MN, Maldonado-Hódar FJ, Moreno-Castilla C. Influence of Pt particle size on catalytic combustion of xylenes on carbon aerogel-supported Pt catalysts. Appl Catal B 2005; 61(3-4): 253-8.

[13] Moreno-Castilla C, Maldonado-Hódar FJ, Pérez-Cadenas AF. Physico-chemical surface properties of Fe, Co, Ni and Cu-doped monolithic organic aerogels. Langmuir 2003; 19(14): 5650-5.

[14] Moreno-Castilla C, Ferro-García MA, Joly JP, Bautista-Toledo I, Carrasco-Marín F, et al. Activated carbons surface modifications by nitric acid, hydrogen peroxide and ammonium peroxydisulfate treatments. Langmuir 1995; 11(11): 4386-92.

[15] Cazorla-Amorós D, Alcañiz-Monge J, De la Casa-Lillo MA, Linares-Solano A. CO_2 as an adsorptive to characterize carbon molecular sieves and activated carbons. Langmuir 1998; 14: 4589-96.

[16] Stoeckli F. Characterization of microporous carbons by adsorption and immersion techniques. In: Patrick JW, editor. Porosity in carbons: characterization and applications, London: Edward Arnold, 1995: 66-97.

[17] Bansal RC, Donnet JB. Stoeckli F. Active Carbon. New York: Marcel Dekker. 1988: Chapter 3.

[18] Ubago-Pérez R, Carrasco-Marín F, Moreno-Castilla C. Carbon-supported Pt as catalysts for low-temperature methanol decomposition to carbon monoxide and hydrogen. Appl Catal A 2004; 275(1-2): 119-26.

[19] Job N, Pirard R, Pirard JP, Alié C. Non intrusive mercury porosimetry: Pyrolysis of resorcinol-formaldehyde xerogels. Part Part Syst Charact 2006; 23(1): 72-81.

[20] Denoyel R, Fernández-Colinas J, Grillet Y, Rouquerol J. Assessment of the surface-area and microporosity of activated charcoals from immersion calorimetry and nitrogen adsorption data. Langmuir 1993; 9(2): 515-8.

[21] Gonzalez MT, Sepúlveda-Escribano A, Molina-Sabio M, Rodriguez-Reinoso F. Correlation between surface areas and micropore volumes of activated carbons obtained from physical adsorption and immersion calorimetry. Langmuir 1995; 11(6): 2151-5.

[22] Silvestre-Albero J, Gómez de Salazar C, Sepúlveda-Escribano A, Rodriguez-Reinoso F. Characterization of microporous solids by immersion calorimetry. Colloids Surf A 2001; 187-188: 151-65.

[23] Villar-Rodil S, Denoyel R, Rouquerol J, Martinez-Alonso A, Tascon JMD. Characterization of aramid based activated carbon fibres by adsorption and immersion techniques. Carbon 2002; 40(8): 1376-80.

[24] Job N, Pereira MFR, Lambert S, Cabiac A, Delahay G, Colomer JF, et al. Highly dispersed platinum catalysts prepared by impregnation of texture-tailored carbon xerogels. J Catal 2006; 240 (2), 160-71.

[25] Ordoñez S, Díez FV, Sastre H. Characterisation of the deactivation of platinum and palladium supported on activated carbon used as hydrodechlorination catalysts. Appl Catal B 2001; 31(2), 113-22.

[26] Choi HC, Choi SH, Yang OB, Lee JS, Lee KH, Kim YG. Hydrodechlorination of Carbon Tetrachloride over Pt/MgO. J Catal 1996; 161(2): 790-7.

[27] Coloma F, Sepúlveda-Escribano A, Fierro JLG, Rodríguez-Reinoso F. Preparation of platinum supported on pregraphitized carbon-blacks. Langmuir 1994; 10(3): 750-5.

[28] Esumi K, Matsuhisa K, Torigoe K. Preparation of Rodlike Gold Particles by UV Irradiation Using Cationic Micelles as a Template. Langmuir 1995; 11(9): 3285-7.

[29] Ohara PC, Heath JR, Gelbart WM. Self-assembly of submicrometer rings of particles from solutions of nanoparticles. Angew Chem Int Ed Engl 1997; 36(10): 1077-80.

[30] Chung SW, Markovich G, Heath JR. Fabrication and Alignment of Wires in Two Dimensions. J Phys Chem B 1998; 102(35): 6685-7.

[31] Hutchinson TO, Liu YP, Kiely C, Kiely CJ, Brust M. Templated gold nanowire self-assembly on carbon substrates. Adv Mater 2001; 13(23): 1800-3.

[32] Murphy CJ, Jana NR. Controlling the aspect ratio of inorganic nanorods and nanowires. Adv Mater 2002; 14(1): 80-2.

[33] Kim F, Song JH, Yang P. Photochemical Synthesis of Gold Nanorods. J Am Chem Soc 2002; 124(48): 14316-7

[34] Sun Y, Xia Y. Large-scale synthesis of uniform silver nanowires through a soft, self-seeding, polyol process. Adv Mater 2002; 14(11): 833-7.

[35] Surendran G, Apostolescu G, Tokumoto M, Prouzel E, Ramos L, Beaunier P, et al. From self-assembly of platinum nanoparticles to nanostructures materials. Small 2005; 1(10): 964-7.

[36] Tang Z, Kotov NA. One-dimensional assemblies of nanoparticles: Preparation, properties and promise. Adv Mater 2005; 17(8): 951-62.

[37] Nakashima H, Furukawa K, Kashimura Y, Torimitsu K. Self-Assembly of Gold Nanorods Induced by Intermolecular Interactions of Surface-Anchored Lipids. Langmuir, 2008; 24(11): 5654-8

CHAPTER IV

HYDROGENOLYSIS AND ISOMERIZATION OF N-BUTANE ON PT CATALYSTS SUPPORTED ON CARBON AEROGELS AND ACTIVATED CARBON

1. ABSTRACT

Hydrogenolysis and isomerization reactions of n-butane on Pt supported on carbon aerogels and an activated carbon were studied in this work. Turnover frequency (TOF) for hydrogenolysis was influenced by the support. This could be due to the degree of aromatization of the carbon aerogel or to the development of Pt surfaces with different indexes. Both hydrogenolysis and isomerization were related with the mean Pt particle size in the case of the catalysts supported on carbon aerogels obtained at 900-950 ºC. There was a compensation effect between the activation energy and the pre-exponential factor, which was common for both hydrogenolysis and isomerization reactions. This indicates that both reactions have the same intermediate, which was the chemisorbed dehydrogenated alkane.

2. INTRODUCTION

Alkane hydrogenolysis consist of the breakage of C-C bonds with the uptake of hydrogen. They are always exothermic because each hydrogenolysis reaction involves the rupture of a C-C bond and the formation of two C-H bonds. Alkane hydrogenolysis over supported metal catalysts have interest both for the theoretical aspects, as many hydrogenolysis reactions are structure sensitive, and also because of their industrial applications in alkane reforming [1-3]. Structure sensitive reactions are those in which the TOF and/or the selectivity is dependent on metal particle size or metal structure [4]. TOF is defined as the number of molecules reacting per surface metal atom and per second.

The type of metal has influence on the catalyst activity and the hydrogenolysis depth, that is, in how many C-C bonds are broken per visit of a reactant molecule to the catalyst surface. Thus, Pt is not so active as other metals of the 8, 9 and 10 groups of the Periodic Table, but is high selective for single hydrogenolysis. This means that it breaks a single C-C bond per visit to the metal surface.

Alkane isomerization can also takes place under hydrogenolysis conditions. Although both reactions depend on the metal catalyst and the support it has been shown that, in general, Pt catalysts are more active in the hydrogenolysis than in the isomerization reaction.

In the present work the n-C_4H_{10}/H_2 reaction was used to test the catalytic activity of different Pt catalysts supported on selected carbon aerogels, whose preparation and characterization were described in details in previous Chapters of this PhD memory. An activated carbon was also used as Pt catalyst support with the purpose of comparison.

3. EXPERIMENTAL

Supports used were the carbon aerogels: CA1, CA2, CA3, P1-900, P3-500, P3-900, POX-500 and POX-900. The activated carbon used as support was BV46. Preparation and characterization of this support was described in detail elsewhere [5]. Briefly, it was prepared from olive stones after carbonization in N_2

flow at 900 ºC and steam activation at 850 ºC to 45 % burn-off. This was a microporous activated carbon with surface area from immersion calorimetry into benzene of 1153 m^2/g and a micropore volume of 0.40 cm^3/g from benzene adsorption at 30 ºC.

In all cases the Pt loading was 2 wt.%. Preparation and characterization of Pt catalysts using the supports CA1, CA2 and CA3 were described in detail in Chapter IV, and the rest of supported catalysts were prepared and characterized following the same methods described in that Chapter. The pre-treatment of catalysts before their characterization was carried out in He flow, 60 cm^3/min, at 400 ºC for 12 h.

The n-C_4H_{10}/H_2 reaction was studied in a glass, plug-flow microreactor. The amount of catalyst was 0.1 g and the temperature was between 260 and 390 ºC depending on the supported catalyst used. Before reaction the catalysts were pre-treated in the same reactor at 400 ºC in He flow for 12 h. After reaction the samples were cooled in flowing He to the reaction temperature and the He flow switched to a n-C_4H_{10}/H_2 flow, 60 cm^3/min, with a 1/10 molar ratio. Gases from the reactor were analyzed on-line with a gas chromatograph, Varian model CP-3800, using a Chromosorb 102 column. The reactor was operated at atmospheric pressure and the conversion was kept below around 16 %.

Catalytic activity measurements for hydrogenolysis and isomerization will be reported as TOF, i.e., the number of n-butane molecules that react per surface Pt atom and per second. The TOF was calculated from the equation (1):

$$TOF_X = \frac{0.74 \times P_X \times F_{n\text{-}C_4H_{10}}}{W \times 2 \times Q_{H_2}} \qquad (1)$$

where TOF_x is the turnover frequency for hydrogenolyesis (TOF_H) or for isomerization (TOF_I) in s^{-1}, P_X is the proportion of n-butane undertaking hydrogenolysis (P_H) or converted to isobutane (P_I), $F_{n\text{-}C_4H_{10}}$ is the n-butane flow rate (cm^3/min), W is the weight of catalyst (g), Q_{H_2} is the dihydrogen uptake (μmol/g), which was multiplied by two due to dihydrogen is dissociatively chemisorbed on two surface Pt atoms, and 0.74 is the conversion factor from cm^3/min to μmol/s.

4. RESULTS AND DISCUSSION

Results obtained in the characterization of Pt catalysts supported on carbon aerogels from CA series were presented and discussed in Chapter IV. So, in this Chapter will be presented results obtained with the rest of supported catalysts. A TEM micrograph of catalyst P3-900-2Pt after its reduction pre-treatment is given in Figure 1, as an example, and shows that Pt particles were well dispersed on the support. Pt particle size distributions (PSDs) were obtained from different pictures similar to the above one. Figure 2 shows the PSDs of catalysts POX-500-2Pt and POX-900-2Pt. Both distributions are narrow with around 90 % of particles below 4 nm in size, being narrower the PSD of the last catalyst. Similar PSDs for the rest of the supported catalysts are shown in Figure AIII.1 of the Appendix III. Mean Pt particle size and its dispersion from H_2 chemisorption at 25

ºC and from PSDs are compiled in Table 1. For the same catalyst, d_{H_2} and d_{TEM} values are similar or very close.

The $Pt_{4f7/2}$ core level deconvoluted spectra of some selected catalysts are depicted in Figure A.III.2 of Appendix III. Results obtained from these spectra are compiled in Table 2 and they are similar to those reported in Chapter IV for Pt catalysts supported on CA series. Thus, there are two peaks: one at 71.6 eV and the other one at 73.0-73.2 eV that can be assigned to Pt(0) and Pt(II), respectively. In all cases the percentage of Pt(0) was higher than that of Pt(II).

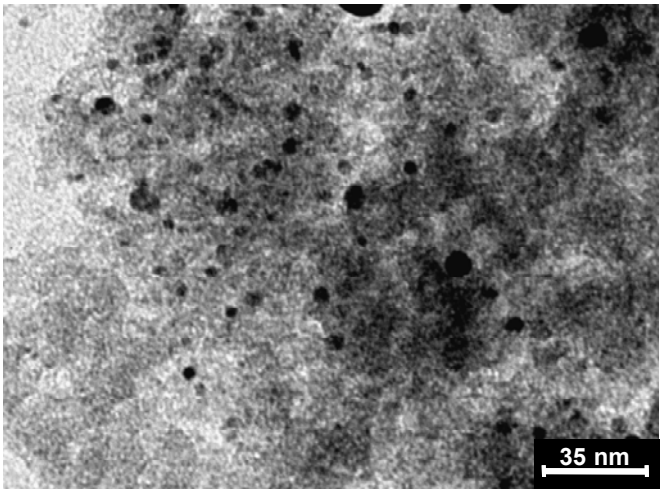

Figure 1. TEM picture of catalyst P3-900-2Pt

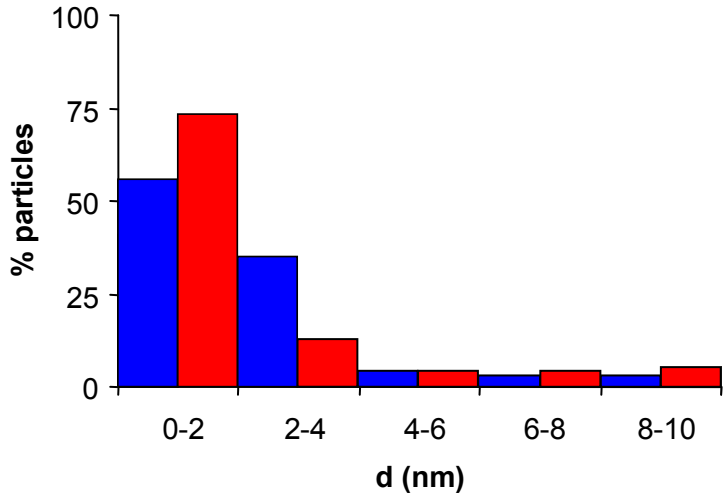

Figure 2. Particle size distribution of catalysts: POX-500-2Pt and POX-900-2Pt

Table 1.- Mean particle size (d) and dispersion (D) from H_2 chemisorption at 25 ºC and TEM

Catalyst	d_{H_2} (nm)	d_{TEM} (nm)	D_{H_2} (%)	D_{TEM} (%)
CA1-2Pt	1.8	1.3	60	83
CA2-2Pt	2.1	1.6	51	68
CA3-2Pt	3.8	2.9	28	37
P1-900-2Pt	3.3	3.6	36	30
P3-900-2Pt	2.6	2.9	42	39
POX-900-2Pt	2.5	2.6	44	42
P3-500-2Pt	3.7	5.3	29	20
POX-500-2Pt	2.8	2.9	38	37
BV46-2Pt	4.0	n.d	27	n.d

n.d: not determined

Table 2.- Results of deconvoluting the $Pt_{4f7/2}$ component of the XPS profile of pre-treated catalysts. Binding energy (BE) of the peaks in eV, percentage of the peaks, surface Pt content (Pt_{XPS}) and surface to total Pt ratio (Pt_{XPS}/Pt_{Total})

Catalyst	BE	%	BE	%	Pt_{XPS} (wt.%)	Pt_{XPS}/Pt_{tot}
P1-900-2Pt	71.6	74	73.1	26	1.7	0.85
P3-900-2Pt	71.6	79	73.0	21	1.7	0.85
P3-500-2Pt	71.6	77	73.2	23	2.9	1.45

The $n\text{-}C_4H_{10}/H_2$ reaction catalyzed by Pt yields the hydrogenolysis products (propane, ethane and methane) simultaneously to iso-butane according to the following scheme (1):

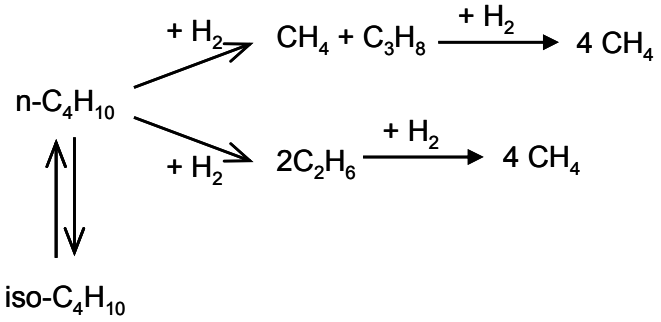

(1)

Since n-butane has only four carbon atoms the formation of cyclic isomerization products is not probable and the only isomerization product is iso-butane. The reaction is produced in presence of H_2, which regulates the concentration of surface intermediates with different dissociation degrees [1]. The n-butane hydrogenolysis might take place through a terminal C-C bond cleavage

yielding CH_4 and C_3H_8 or by the central C-C bond cleavage yielding C_2H_6. In the first case, the propane produced might undergo hydrogenolysis yielding ethane and methane. Ethane produced can be further degraded to methane.

Product distributions obtained at 320 ºC are compiled in Table 3. Results show that the percentages of methane and propane produced are practically coincident in all cases. It is then possible to assume that the methane obtained in the reaction is produced by terminal C-C bond cleavage and that there is no multiple hydrogenolysis of butane as with other catalysts like Ni [3,6], which was attributed to demethylation.

Catalytic conversion for hydrogenolysis and isomerization of n-butane against temperature are shown, as an example, in Figure 3 for catalysts CA1-2Pt, POX-500-2Pt and POX-900-2Pt. The rest of conversions against temperature curves are plotted in Figures AIII.3 to AIII.7 of Appendix III. These Figures show that the increase of conversion with temperature was more pronounced in case of the hydogenolysis reaction.

TOF values at 320 ºC are compiled in Table 4. For Pt catalysts supported on carbon aerogels obtained at 900-950 ºC TOF_H is much higher, about one order of magnitude, than TOF_I. These results are in agreement with others found with Pt(100) and Pt(111) single crystals and polycrystalline Pt foil [7], and Pt catalysts supported on zeolite [8]. In contrast, Pt catalysts prepared with supports carbonized at 500 ºC (P3-500 and POX-500) and the activated carbon BV46 exhibit TOF_H values lower than the other catalysts, and equal or quite close to TOF_I.

Table 3.- Conversions (%) and product distributions (mol %) in the n-C_4H_{10}/H_2 reaction at 320 ºC

Catalyst	Conversion (%)		C_1	C_2	C_3	i-C_4
	H	I				
CA1-2Pt	6.2	0.4	40	17	40	3
CA2-2Pt	6.7	0.4	40	17	40	3
CA3-2Pt	6.0	0.7	40	16	39	5
P1-900-2Pt	6.7	0.5	40	18	39	3
P3-900-2Pt	7.3	0.3	41	17	40	2
POX-900-2Pt	7.1	0.4	40	17	40	3
P3-500-2Pt	0.2	0.2	31	17	22	30
POX-500-2Pt	0.3	0.3	30	9	30	31
BV46-2Pt	0.8	0.3	35	18	30	17

It is important to highlight that TOF_H of POX-500-2Pt is around twenty times smaller than that of POX-900-2Pt, although the supports have similar surface area and pore texture (Chapter I, Table7) and both catalysts have similar mean Pt particle size (Table 1). The same occurs when catalysts P3-500-2Pt and P1-900-2Pt, with similar d_{H_2} values, are compared.

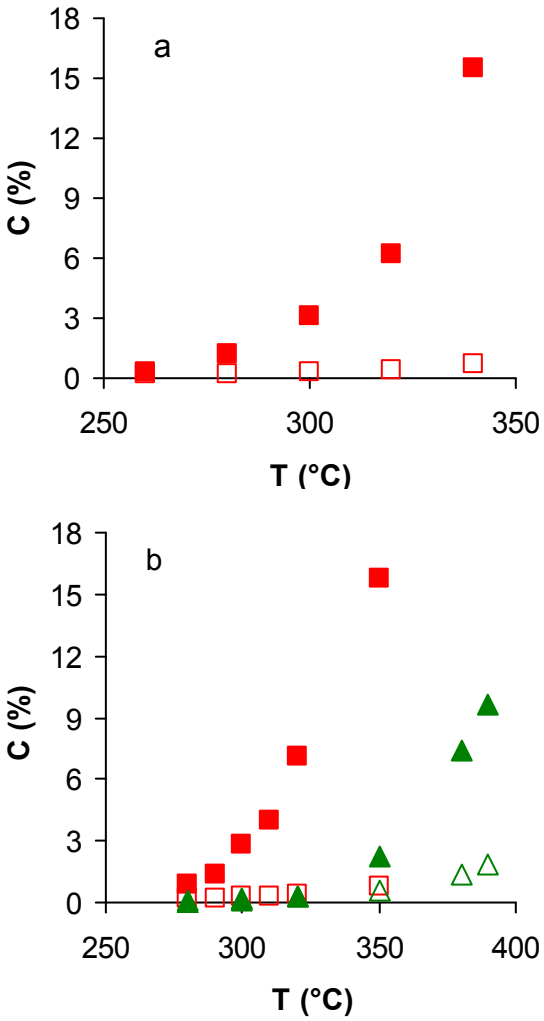

Figure 3. Conversion against reaction temperature. (a) □, CA1-2Pt, (b) △, POX-500-2Pt and □, POX-900-2Pt. Closed symbols, hydrogenolysis; open symbols, isomerization

Table 4.- Turnover frequencies (TOF×10^3) at 320 ºC, activation energies (E_a) and pre-exponential factor (Ln A) for hydrogenolysis (H) and isomerization (I) reactions

Catalyst	TOF_H s^{-1}	TOF_I s^{-1}	Temp. range ºC	E_a(H) kJ/mol	Ln A(H)	E_a(I) kJ/mol	Ln A(I)
CA1-2Pt	37.5	2.5	260-340	131	27	42	7
CA2-2Pt	51.2	3.1	270-320	138	29	30	4
CA3-2Pt	74.3	8.2	280-320	150	31	55	10
P1-900-2Pt	72.1	4.9	280-330	155	32	49	8
P3-900-2Pt	67.4	3.0	280-380	143	30	32	4
POX-900-2Pt	61.6	3.3	280-350	147	31	31	4
P3-500-2Pt	3.4	3.2	280-390	142	29	70	12
POX-500-2Pt	3.2	3.1	280-390	153	31	72	13
BV46-2Pt	8.1	2.6	300-400	129	27	125	24

An important difference found between carbon aerogels carbonized at 500 and 900 ºC is that aromatization degree of the carbon structure increased with higher carbonization temperature (see Chapter II). So, according to this the higher the aromatization degree of the carbon aerogel the higher the TOF of the Pt catalyst supported on it for the n-butane hydrogenolysis. The explanation lies in that there could be electronic transfer between the support and the Pt particles that would make easier the cracking of the chemisorbed alkane as it will be shown later.

Another possible explanation, for the above differences found in TOF_H and TOF_I with the type of support, is that Pt particles supported on carbon aerogels

obtained at 900-950 ºC develop preferentially low-index Pt surfaces. Thus, it has been shown [7] that the more open Pt(100) surfaces are one order of magnitude more active for the hydrogenolysis of n-butane than the close-packed Pt(111) surfaces.

On the other hand, TOF_H and TOF_I values of catalyst BV46-2Pt are of the same order of magnitude than other Pt catalysts supported on activated carbons that are reported in the literature [1]. Likely, the differences in aromatization degree between carbon aerogels obtained at high temperature and activated carbons could be also the explanation to that behavior.

The relationships between TOF_H and TOF_I with the mean Pt particle size are depicted in Figure 4. For catalysts supported on carbon aerogels prepared at 900-950 ºC TOF_H linearly increases with d_{H2} up to around 3 nm in size, reaching a plateau up to around 4 nm. However, in all the d_{H2} range studied TOF_I lineraly increases although in a much lesser extent than TOF_H. Hydrogenolysis reaction in the above catalysts seems to be sensitive to the catalyst structure at least up to a mean Pt particle size of 3 nm. However, the variation of TOF_I in the particle size range studied is not so high and it is difficult to assure that this reaction is sensitive to catalyst structure. These results are different to those found with Pt catalyst supported on activated carbons [1], where TOF_H lineraly increased with the increase in the mean Pt particle size, and TOF_I was insensible to the variation in Pt particle size. Perhaps this was due to the differences in surface chemistry between carbon aerogels and activated carbons.

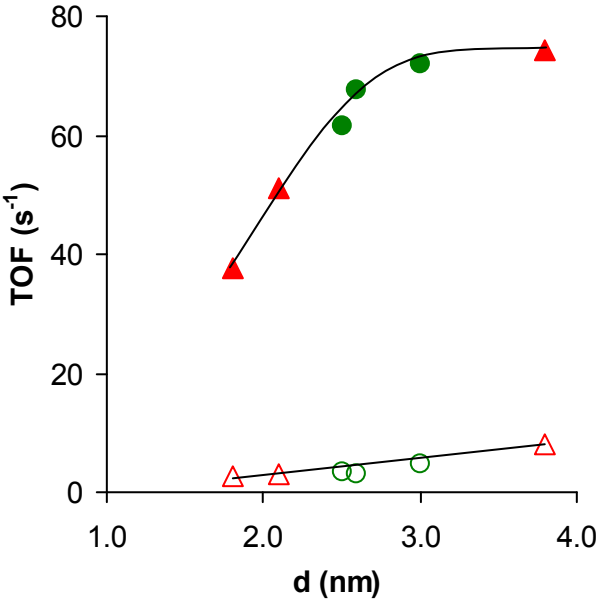

Figure 4. Relationship of TOF_H, closed symbols and TOF_I, open symbols at 320 ºC with the mean Pt particle size for catalysts supported on carbon aerogels obtained at 900 ºC, ○ and 950 ºC, △.

Arrhenius plots were used to calculate the apparent activation energy for hydrogenolysis, $E_a(H)$, and isomerization $E_a(I)$. These plots are depicted in Figures AIII.8 to AIII.16 of the Appendix III and the activation energies and the corresponding frequency factors, Ln A_H and Ln A_I, are compiled in Table 4. For all catalysts supported on carbon aerogels $E_a(H)$ was higher than $E_a(I)$, whereas for catalyst BV46-2Pt $E_a(H)$ and $E_a(I)$ were equal, which is in agreement with results found for Pt catalysts supported on activated carbons [1].

Several models for hydrogenolysis reactions over metal catalysts were suggested [3], but the following general reaction mechanism is widely accepted.

Step 1. Dissociative dihydrogen chemisorption and dehydrogenative chemisorption of the alkane

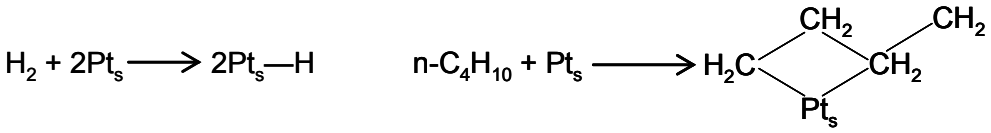

where Pt_s is a surface Pt atom. The formation of this 1,3 diasorbed dehydrogenated alkane intermediate has been postulated for the hydrogenolysis of saturated hydrocarbons on Pt [1].

Steps 2 and 3. Fragmentation of the dehydrogenated species, and rehydrogenation and desorption of the products

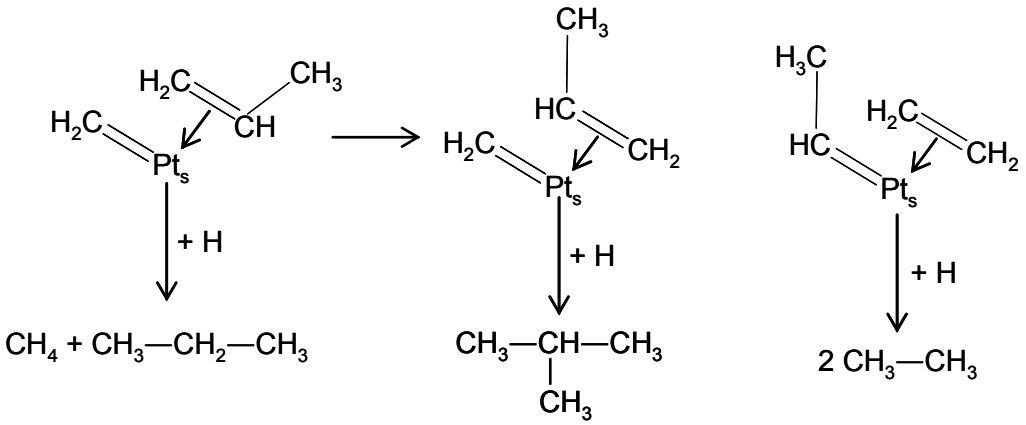

The plot of Ln A against E_a for both the hydrogenolysis and isomerization reactions and for all catalysts is shown in Figure 5, and indicates a good compensation effect (correlation coefficient, R^2 = 0.997). This compensation

effect has been observed for alkane hydrogenolysis over Pt catalysts [2,3] and other metals [9], and other systems [10,11]. In the case of alkane hydrogenolysis, it has been proposed [2,3,11] that it is due to that E_a(H), as measured from rate data, is much higher than the true activation energy for the reactions. The discrepancy arises from a positive contribution to E_a(H) from the dehydrogenative chemisorption of the alkane. Thus, at high temperatures there is a large increase in the concentration of the chemisorbed dehydrogenated alkane, leading to higher reaction rates. Then, this compensation effect implies that no mechanistic information about the rate determining step can be obtained by comparison of overall activation energies. These arguments could explain that E_a(H) > E_a(I) for catalysts supported on carbon aerogels obtained at 900-950 ºC.

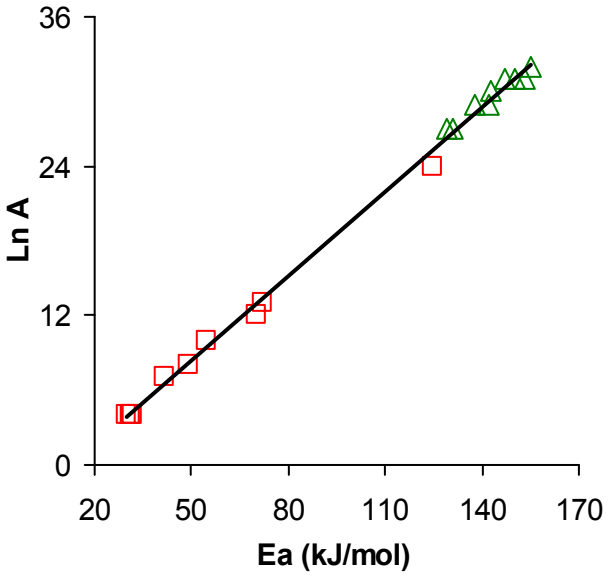

Figure 5.

Compensation effect of n-butane hydrogenolysis (△) and isomerization (□).

An interesting observation is that the isomerization reaction lies on the same compensation effect plot as the hydrogenolysis reaction. This means that both reactions have a common intermediate, the dehydrogenated alkane formed in *Step 1*. Thus, rearrangement of the η^2-propene intermediate in *Step 2* could yield isobutane.

The above hydrogenolysis mechanism could also explain the higher TOF_H value of Pt catalysts supported on carbon aerogels obtained at 900-950 ºC in comparison to those obtained at 500 ºC. The π-olefin complexes are formed by a dative π-bond from the hydrocarbon to empty d-orbitals of Pt and a retrodonating π-bond from the filled d-orbitals to the empty π^* antibonding orbital of the hydrocarbon; both bonds are reinforced each other by a synergic mechanism. Therefore, the increase in the aromatization degree of the support would increase the electronic density on the Pt particles supported on it, leading to an increase of the retrodonating π-bond, and making easier the formation of the above π-olefin complexes, and therefore, the cracking of the chemisorbed dehydrogenated n-butane.

5. CONCLUSIONS

Pt catalyst studied showed single hydrogenolysis. TOF_H was much higher than TOF_I in those catalysts prepared with carbon aerogels obtained at 900-950 ºC. However, TOF_H for catalysts supported on carbon aerogels obtained at 500 ºC and the activated carbon was lower than in the above catalysts and similar to

TOF_I. These results might be due to either the different degree of aromatization of the supports or by the development Pt surfaces with different indexes.

Hydrogenolysis reaction with Pt catalysts supported on carbon aerogels obtained at 900-950 ºC seemed to be structure sensitive at least up to a Pt particle size of 3 nm. However, in the case of the isomerization reaction with these catalysts it is difficult to assure that it was structure sensitive.

There was a clear compensation effect between the apparent activation energy and the pre-exponential factor, which was common to both hydrogenolysis and isomerization reactions. This effect could be due to the dehydrogenative chemisorption of n-butane. On the other hand, both reactions had the same intermediate, the chemisorbed dehydrogenated n-butane.

6. REFERENCES

1. Rodríguez-Reinoso F, Rodríguez-Ramos I, Moreno-Castilla C, Guerrero-Ruiz A, López-González JD. Platinum catalysts supported on activated carbons. II. Isomerization and hydrogenolysis of n-butane. J Catal 1987;107(1):1-7.
2. Bond GC, Cunningham RH. Alkane transformations on supported platinum catalysts. 4. Kinetics of hydrogenolysis of ethane, propane, and n-butane on Pt/Al2O3 (EUROPT-3) and PtRe/Al2O3 (EUROPT-4). J Catal 1997;166:172-85.
3. Jackson SD, Kelly GJ, Webb G. Supported metal catalysts; preparation, characterization, and function. Part VI. Hydrogenolysis of ethane, propane,

n-butane and iso-butane over supported platinum catalysts. J Catal 1998;176:225-34.

4. Che M, Bennett CO. The influence of particle size on the catalytic properties of supported metals. In Eley DD, Pines H, Weisz PB, editors. Advances in Catalysis, vol. 36. San Diego, CA: Academic Press; 1989 p. 55-172.
5. López-Ramón MV, Stoeckli F, Moreno-Castilla C, Carrasco-Marín F. On the characterization of acidic and basic surface sites on carbon by various techniques. Carbon 1999;37(8):1215-21.
6. Jackson SD, Kelly GJ, Webb G. Supported nickel catalysts: Hydrogenolysis of ethane, propane, n-butane and iso-butane over alumina-, molybdena-, and silica-supported nickel catalysts. Phys Chem Chem Phys 1999;1:2581-7.
7. Anderson SL, Szanyi J, Paffett MT. Datye AK. Hydrogenolysis and isomerization of n-butane on low-index Pt single cystals and pollycrystaline Pt foil. J Catal 1996;159:23-30.
8. Bond GC, Lin X. Hydrogenolysis of propane and of n-butane on Pt/KL zeolite. J Catal 1997;169:76-84.
9. Galvey AK. Compensation effect in heterogeneous catalysis. In: Eley DD, Pines H, Weisz PB, editors. Advances in Catalysis, vol. 26. San Diego, CA: Academic Press; 1977 p. 247-322.
10. Gilhooley K, Jackson SD, Rigby S. Steady-state effects in the medium pressure hydrogenation of carbon monoxide over rhodium catalysts. Appl Catal 1986;21:349-57
11. Bond GC. Source of the activation energy in heterogeneously catalysed reactions. Catal Today 1993;17:399-410.

APPENDIX I

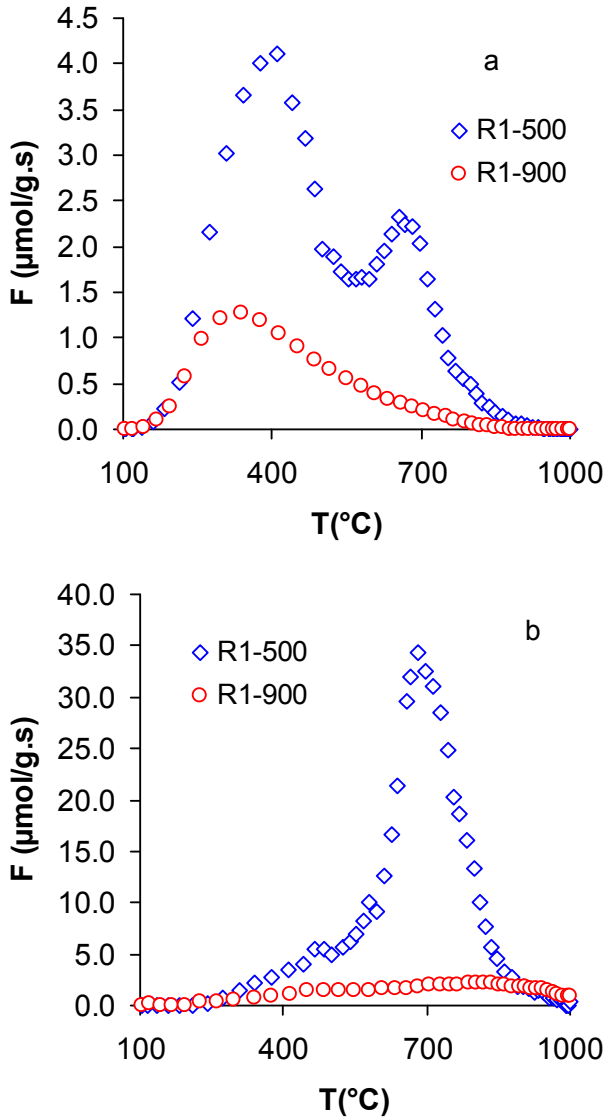

Figure A.I.1. TPD of samples from R1 series. a) CO_2-evolving profiles, b) CO-evolving profiles

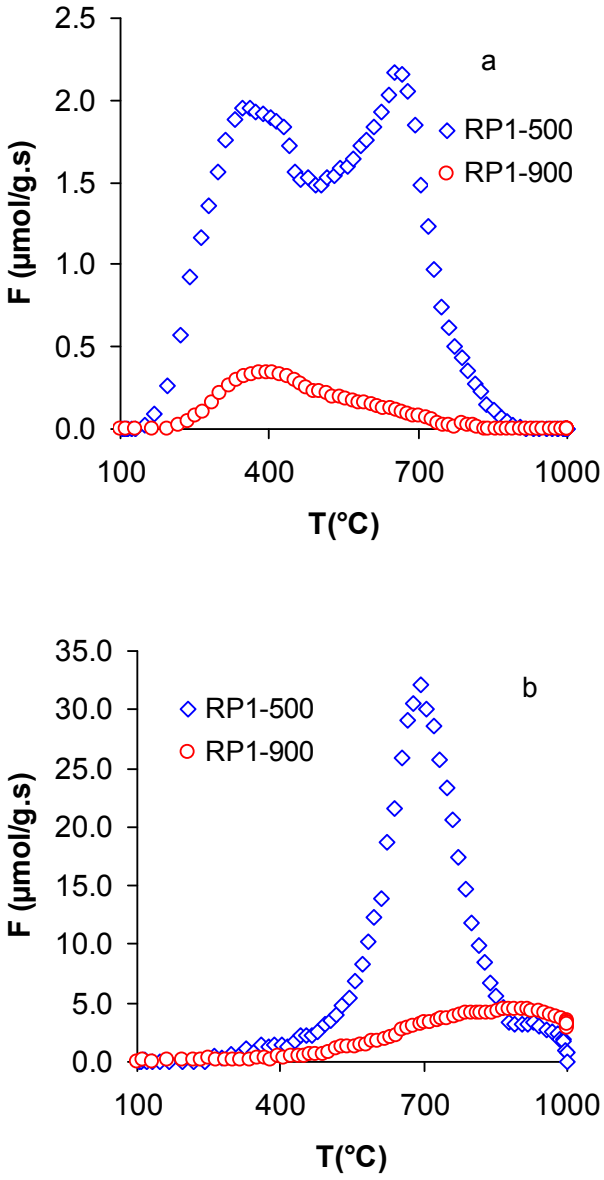

Figure A.I.2. TPD of samples from RP1 series. a) CO_2-evolving profiles, b) CO-evolving profiles

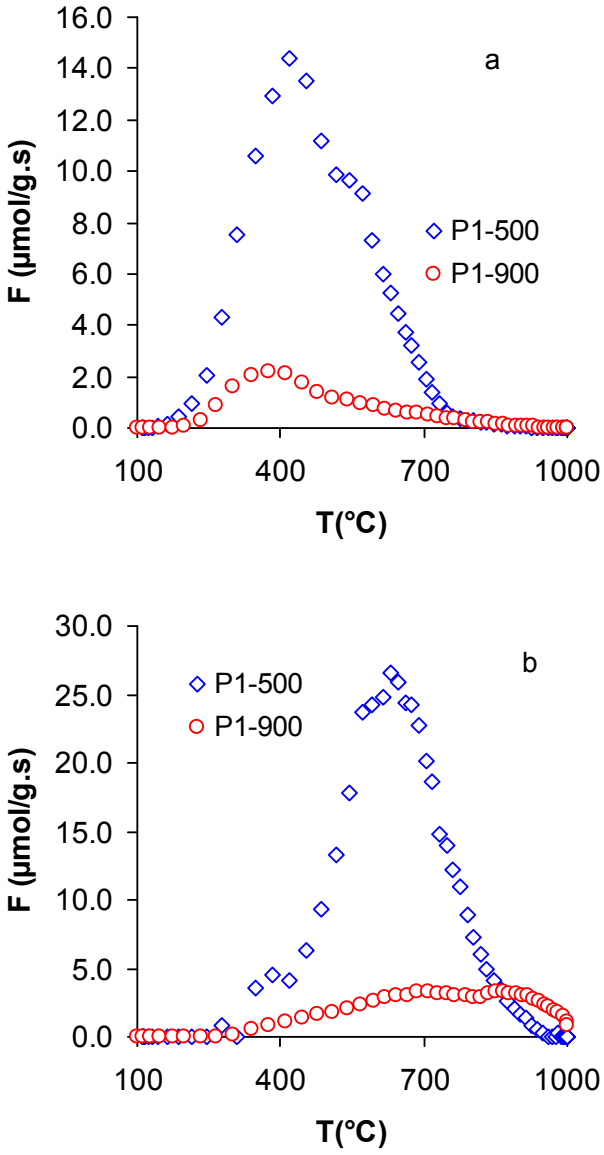

Figure A.I.3. TPD of samples from P1 series. a) CO_2-evolving profiles, b) CO-evolving profiles

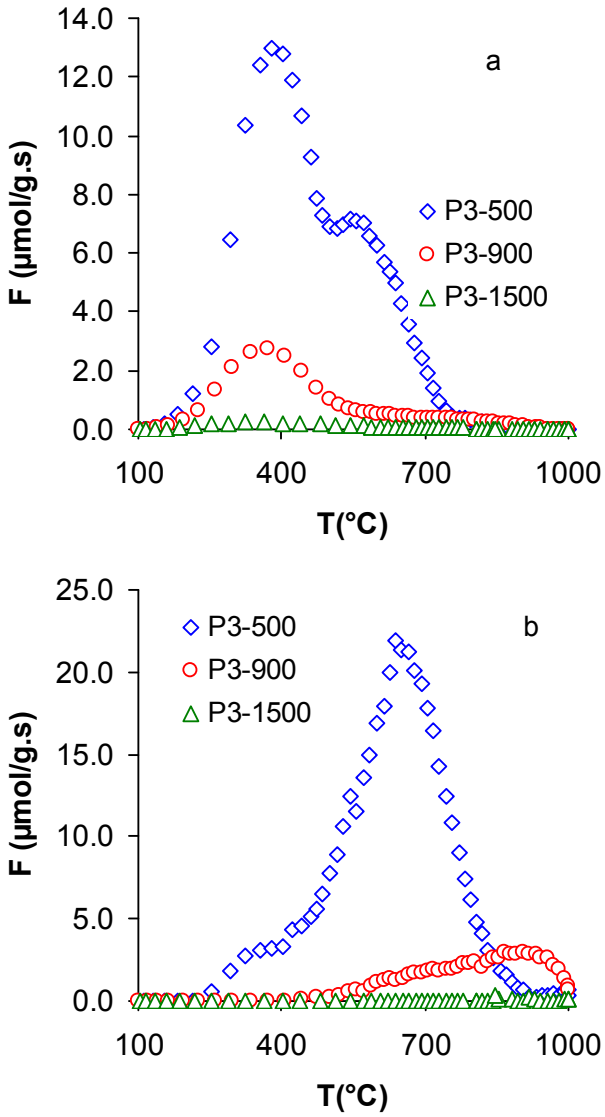

Figure A.I.4. TPD of samples from P3 series. a) CO_2-evolving profiles, b) CO-evolving profiles

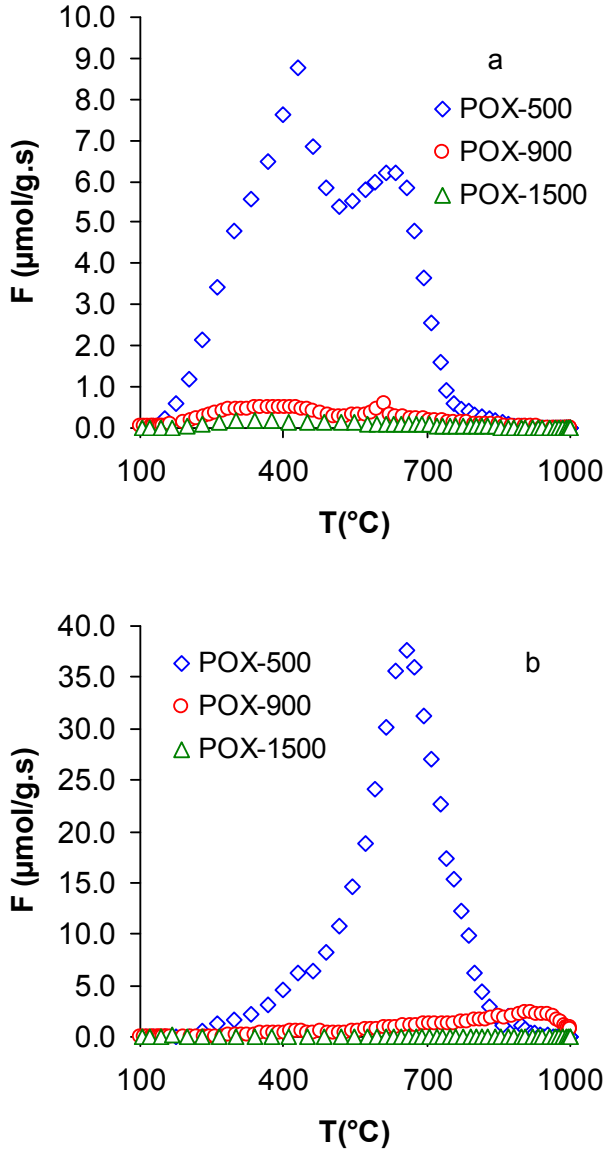

Figure A.I.5. TPD of samples from POX series. a) CO_2-evolving profiles, b) CO-evolving profiles

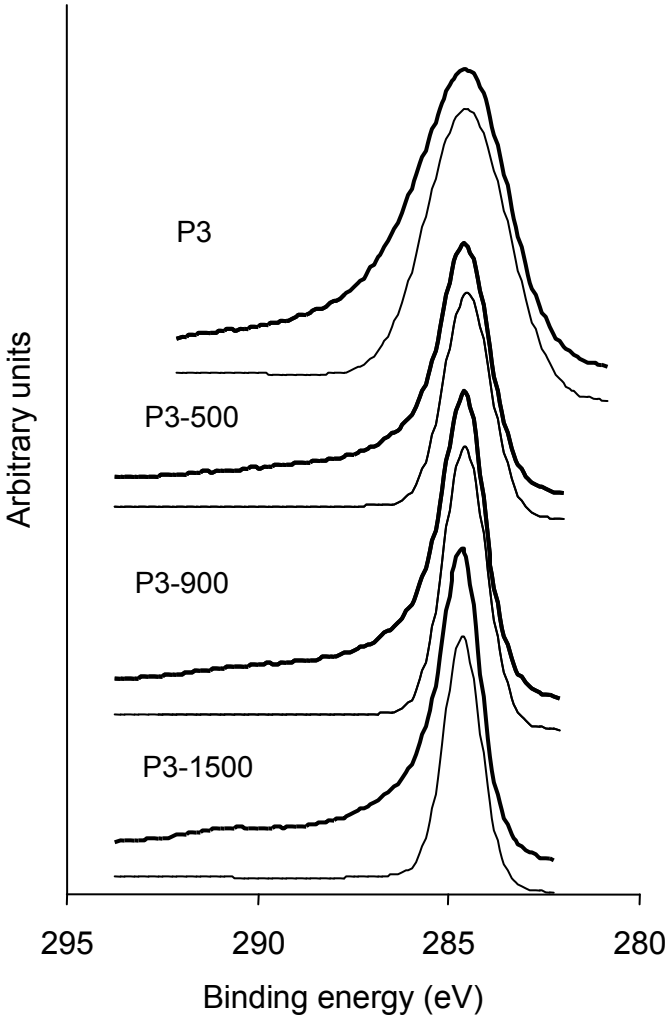

Figure A.I.6. C_{1s} XP spectra (thick curve) of samples from P3 series. Thin curves correspond to the fitted aromatic carbon peak at 284.6 eV.

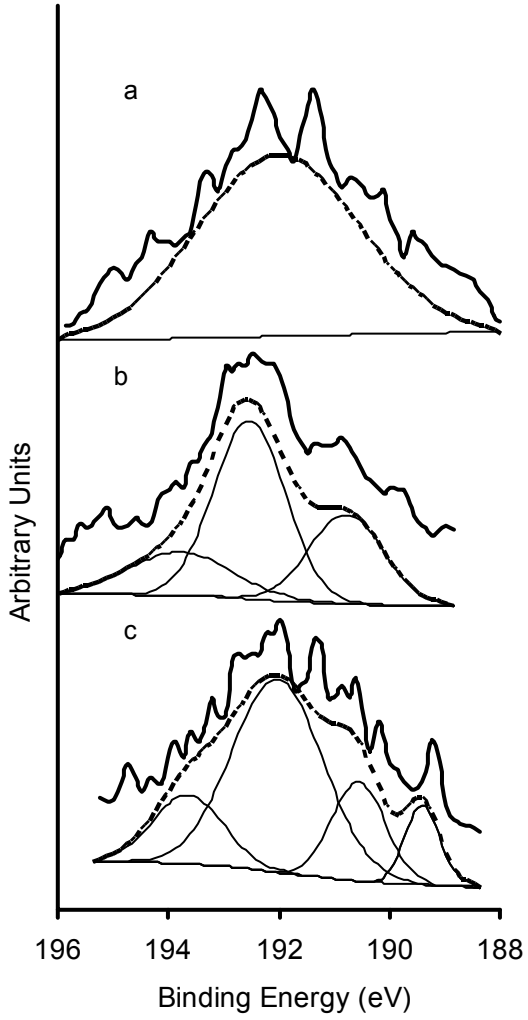

Figure A.I.7. X-ray photoelectron spectroscopy profiles of the B1s region for samples: (a) R1, (b) R1-500, (c) R1-900.

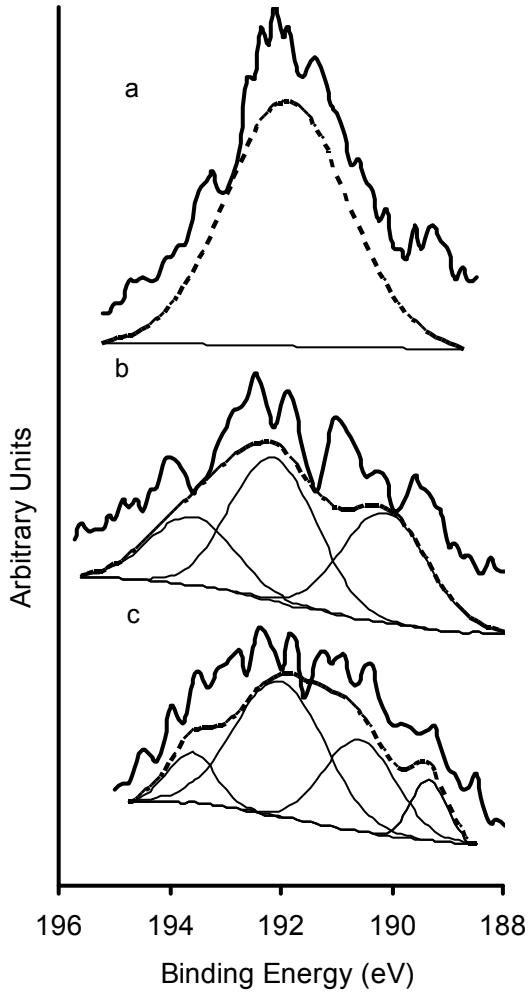

Figure A.I.8. X-ray photoelectron spectroscopy profiles of the B1s region for samples: (a) RP1, (b) RP1-500, (c) RP1-900.

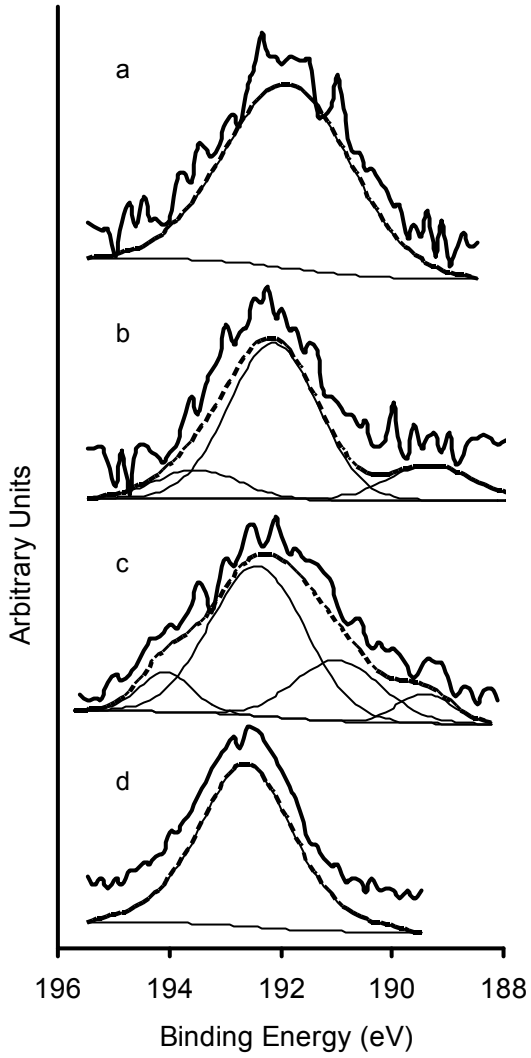

Figure A.I.9. X-ray photoelectron spectroscopy profiles of the B1s region for samples: (a) P3, (b) P3-500, (c) P3-900 and (d) P3-1500.

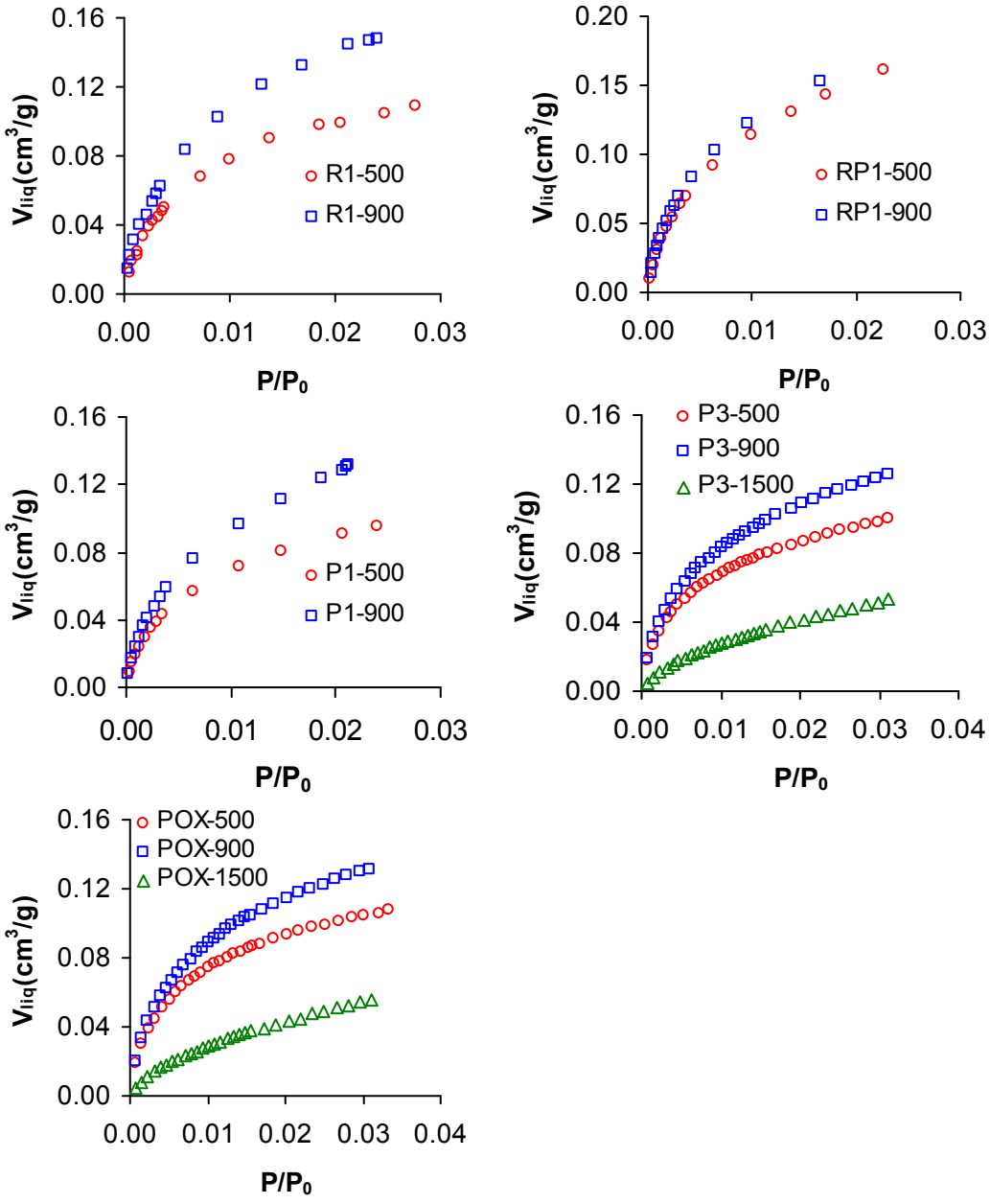

Figure A.I.10. CO_2 adsorption isotherms for carbon aerogel series.

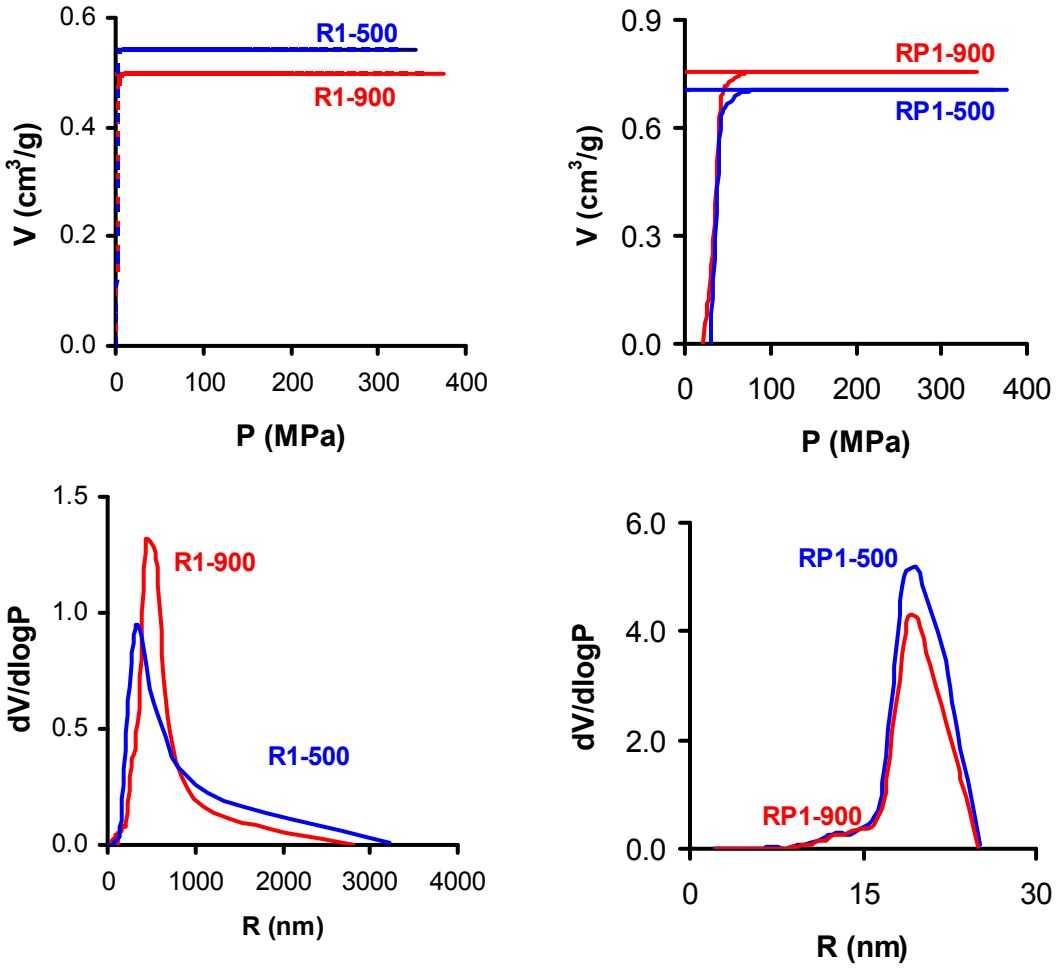

Figure A.I.11. Mercury porosimetry intrusion-extrusion curves for carbon aerogels.

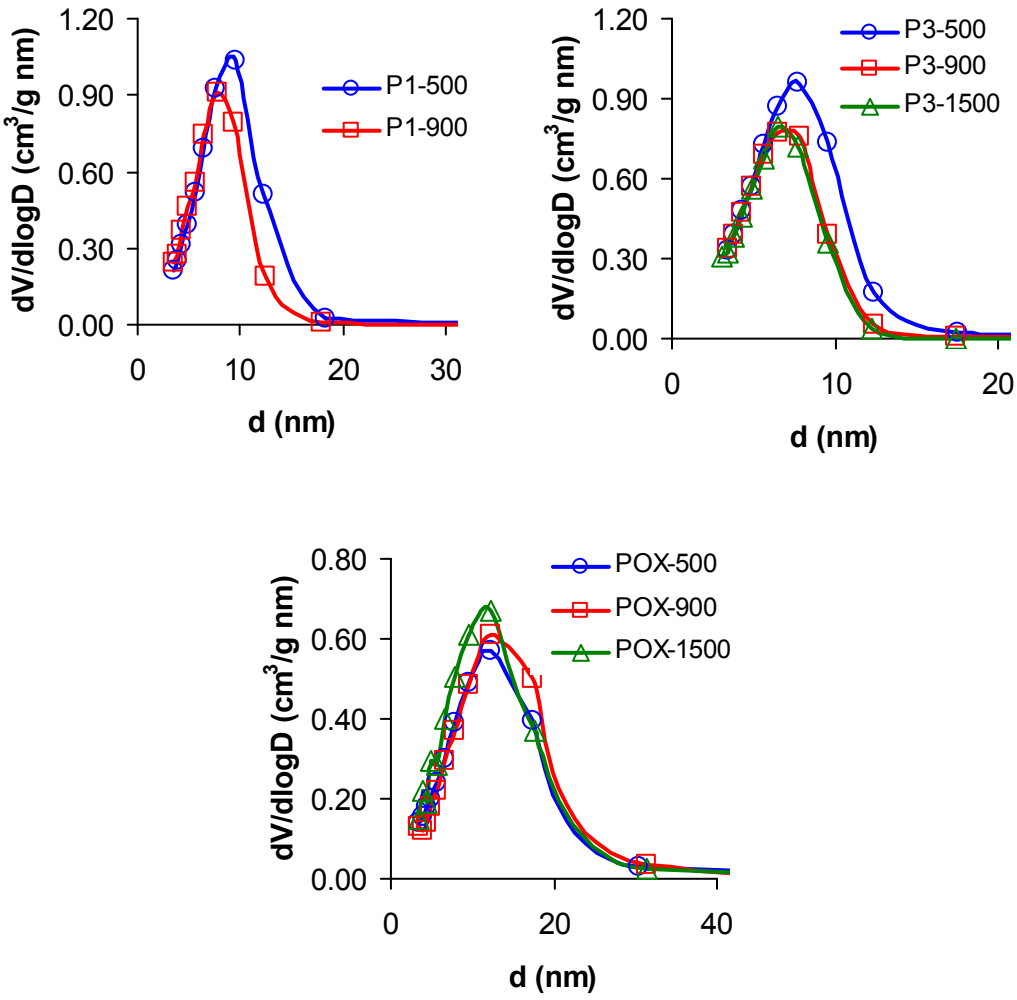

Figure A.I.12. Mesopore size distribution for carbon aerogel series from BJH method.

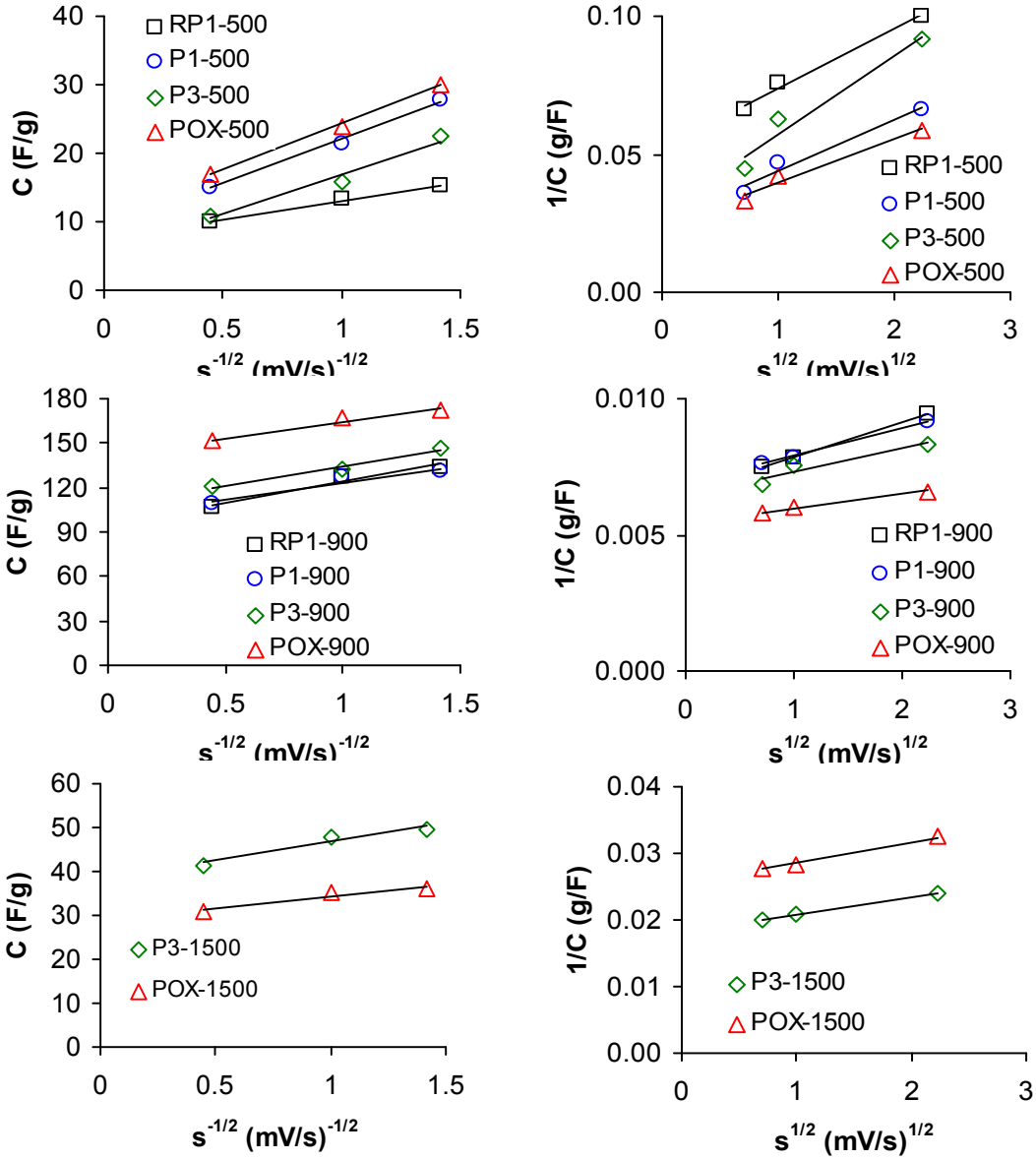

Figure A.I.13. Plots of the gravimetric capacitance vs. the inverse square root of the scan rate and of the inverse gravimetric capacitance vs. the square root of the scan rate.

APPENDIX II

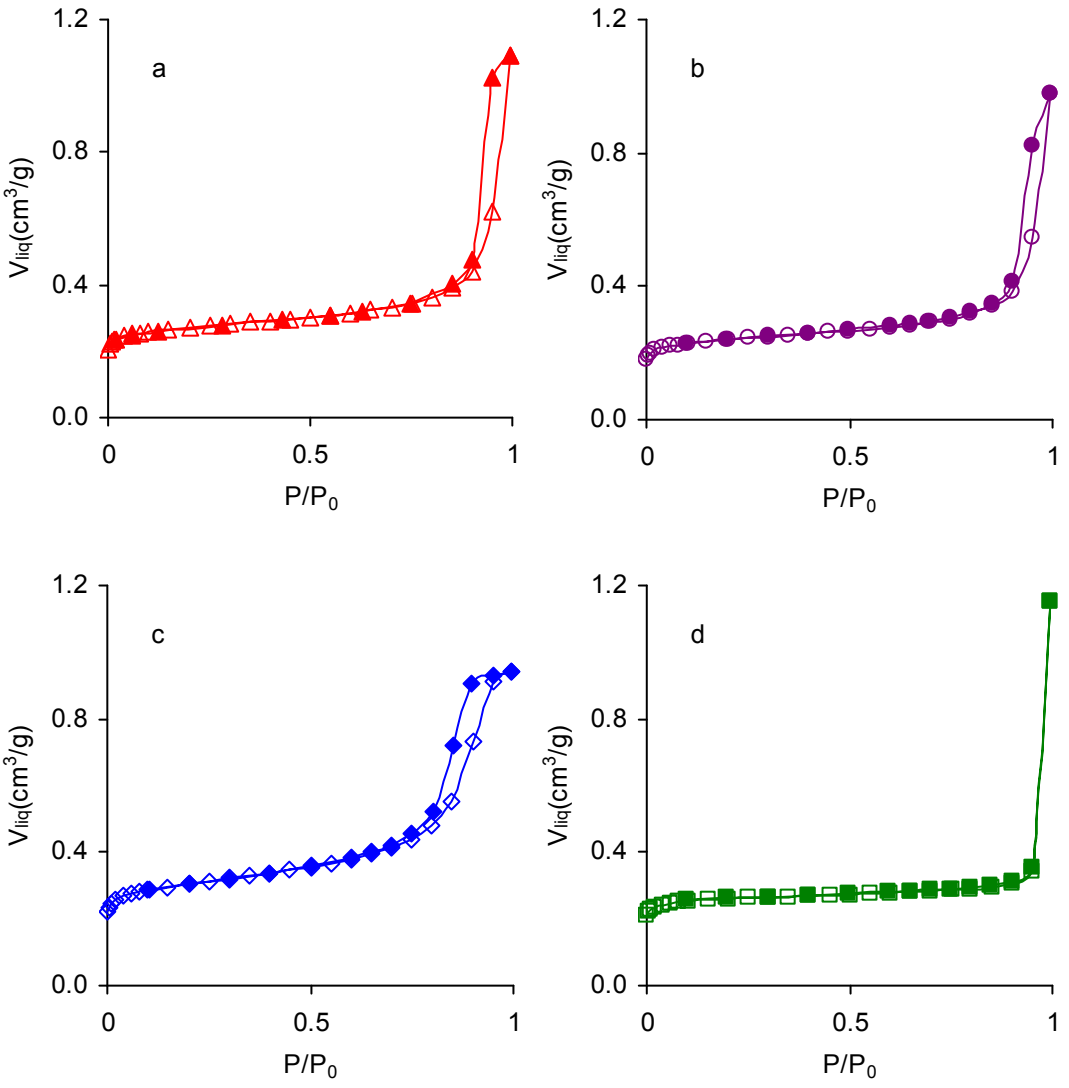

Figure A.II.1. N_2 adsorption-desorption isotherms at -196º C on samples: (a) CA1; (b) CA1S; (c) CA2 and (d) CA3. Adsorption, open symbols and desorption, closed symbols.

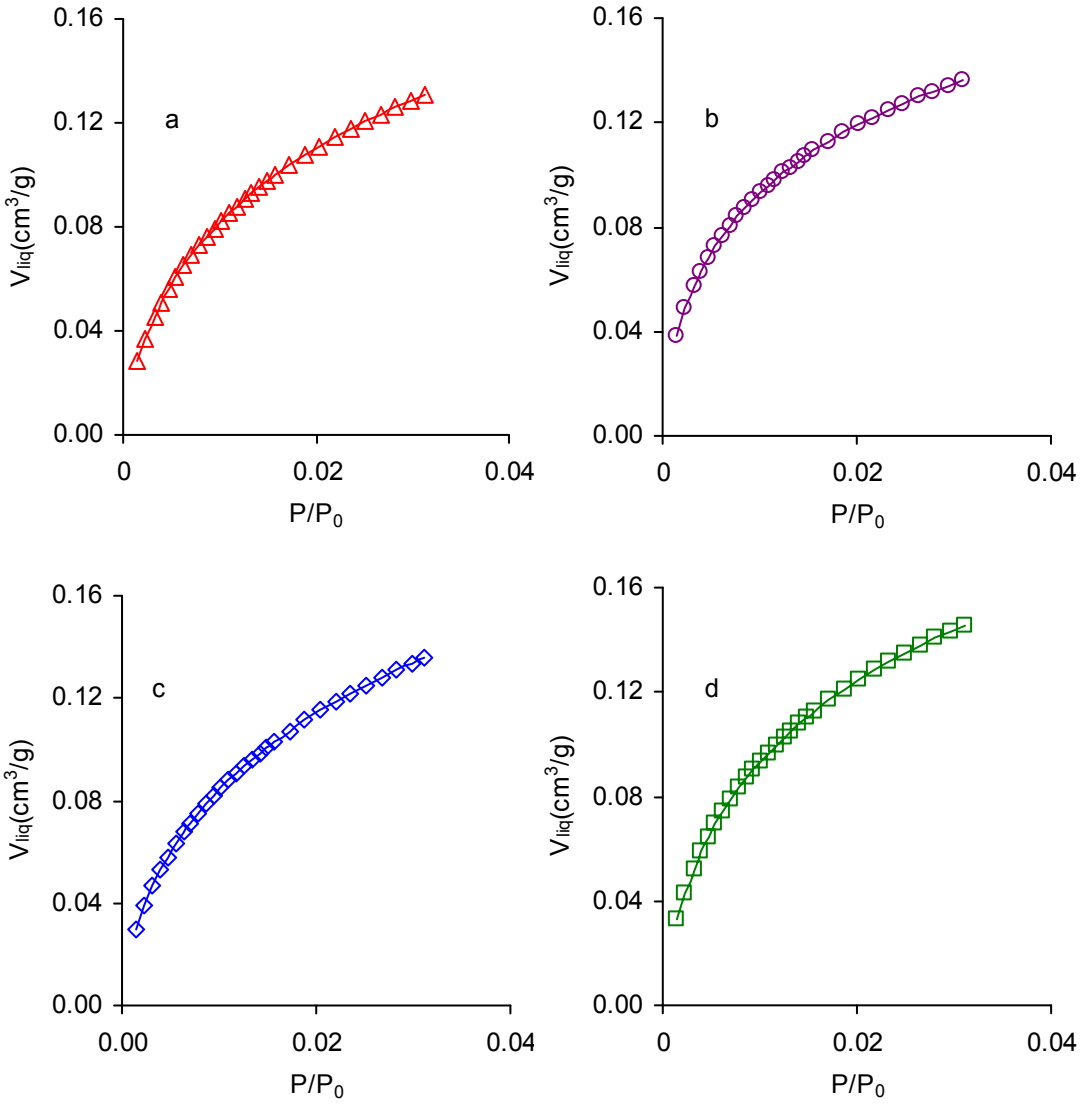

Figure A.II.2. CO_2 adsorption-desorption isotherms at 0º C on samples: (a) CA1; (b) CA1S; (c) CA2 and (d) CA3.

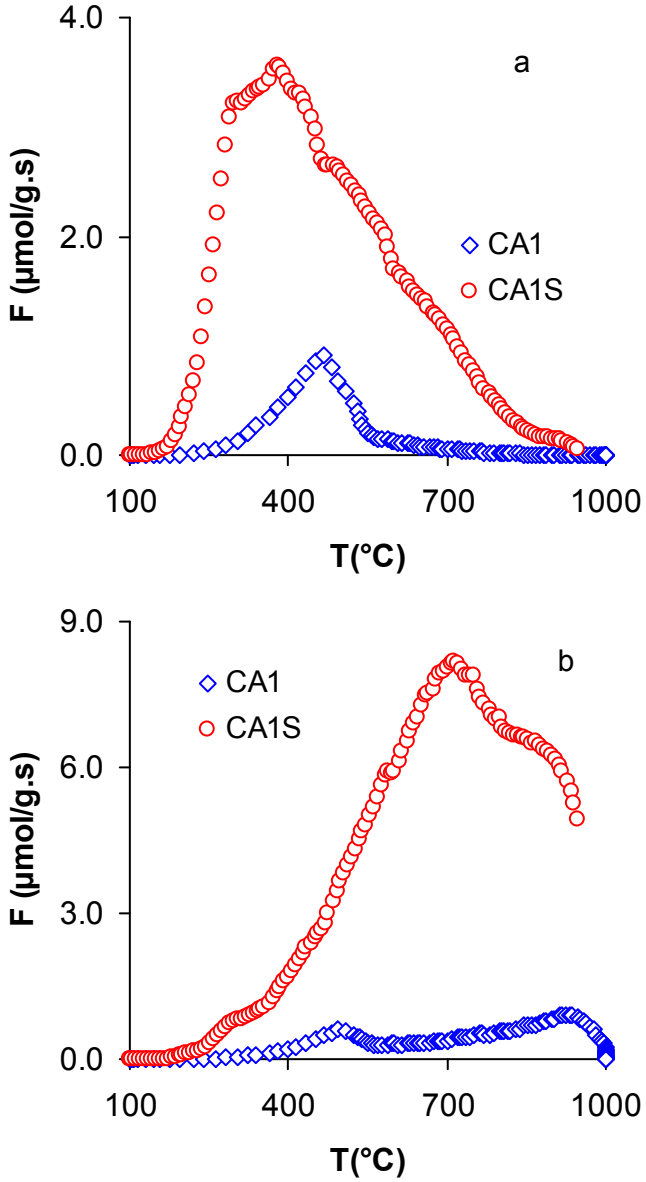

Figure A.II.3. TPD of samples CA1 and CA1S. a) CO_2-evolving profiles, b) CO-evolving profiles

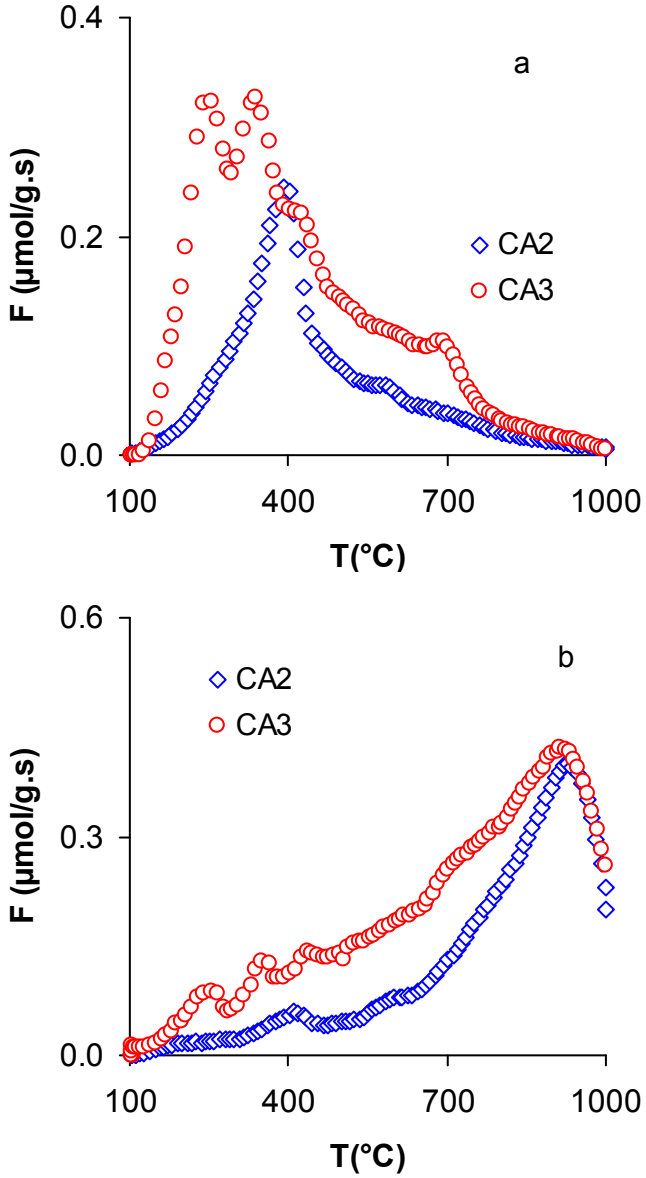

Figure A.II.4. TPD of samples CA2 and CA3. a) CO_2-evolving profiles, b) CO-evolving profiles

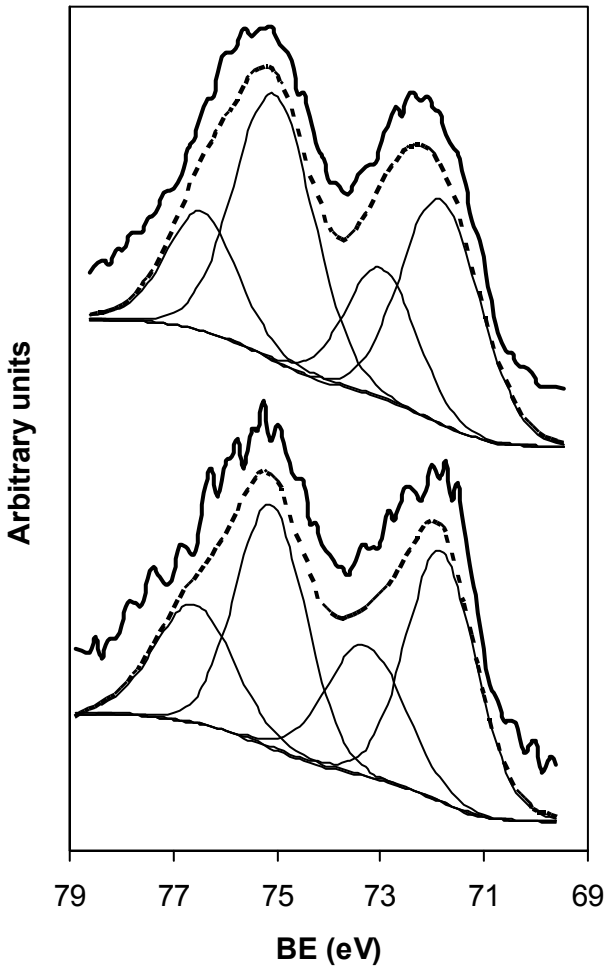

Figure A.II.5. X-ray photoelectron spectroscopy profiles of the Pt_{4f} region for catalysts CA2-2Pt (a) and CA3-2Pt (b) after pre-treatment in He at 400 ºC for 12 h.

APPENDIX III

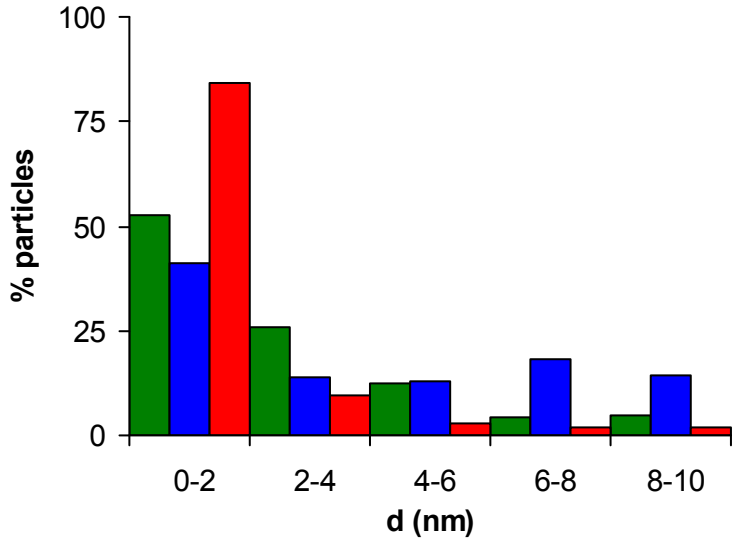

Figure A.III.1. Particle size distribution of catalysts. , P1-900-2Pt; ,P3-500-2Pt; , P3-900-2Pt.

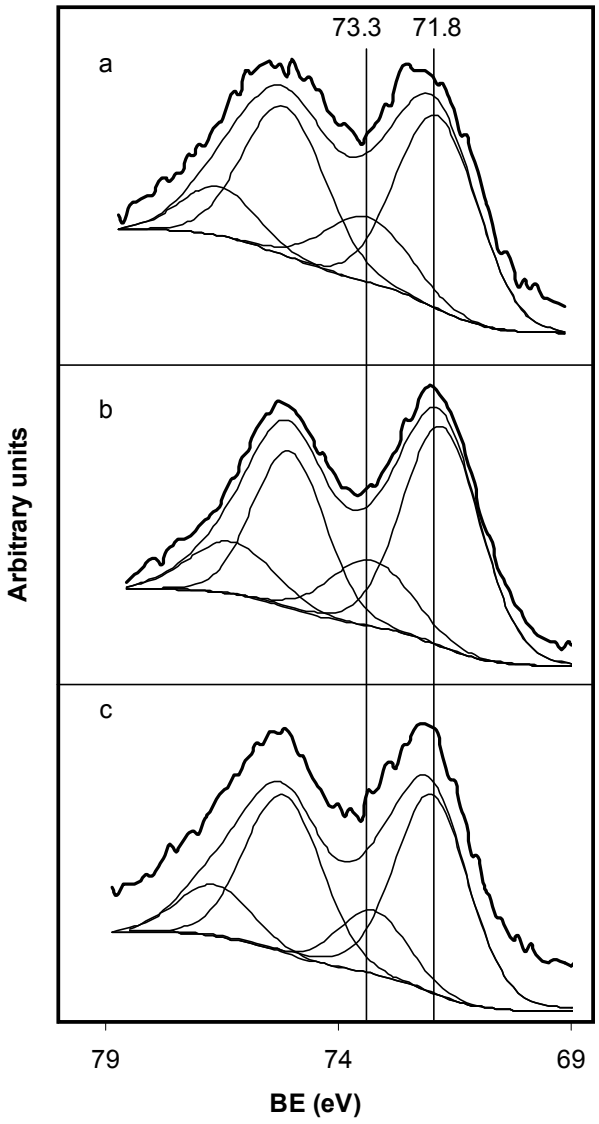

Figure A.III.2. X-ray photoelectron spectroscopy profiles of the Pt4f region for catalysts: a, P1-900-2Pt; b, P3-500-2Pt and c, P3-900-2Pt, after pre-treatment in He at 400 °C for 12 h.

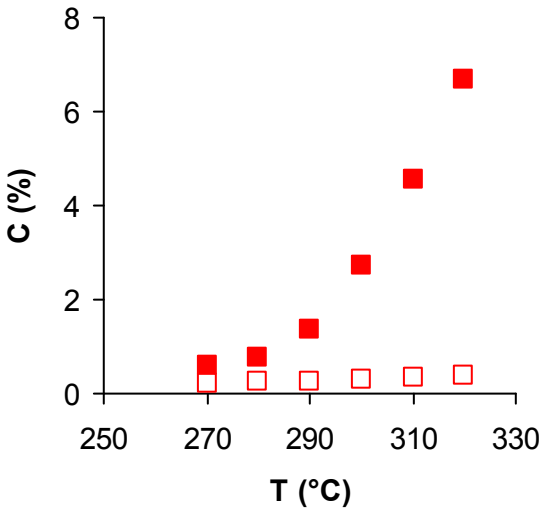

Figure A.III.3. Conversion against reaction temperature on catalyst CA2-2Pt. Hydrogenolysis, closed symbols; isomerization, open symbols.

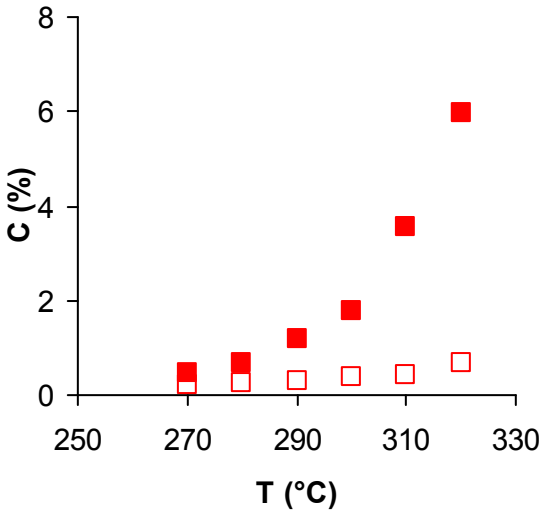

Figure A.III.4. Conversion against reaction temperature on catalyst CA3-2Pt. Hydrogenolysis, closed symbols; isomerization, open symbols

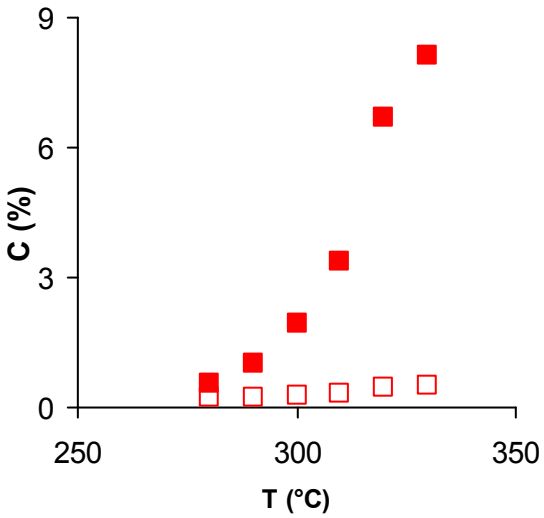

Figure A.III.5. Conversion against reaction temperature on catalyst P1-900-2Pt. Hydrogenolysis, closed symbols; isomerization, open symbols

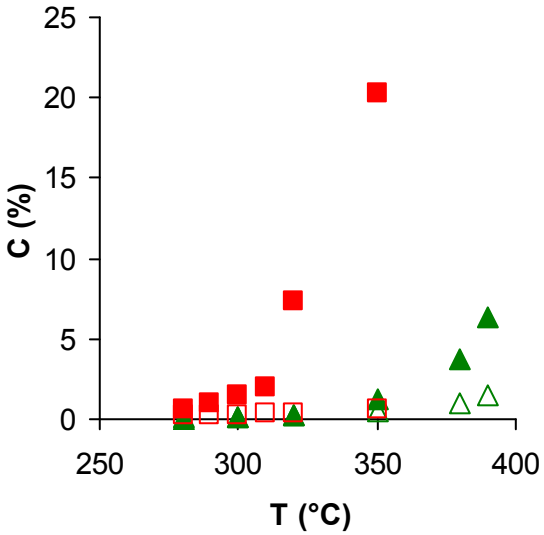

Figure A.III.6. Conversion against reaction temperature on catalysts: △, P3-500-2Pt and □, P3-900-2Pt. Hydrogenolysis, closed symbols; isomerization, open symbols

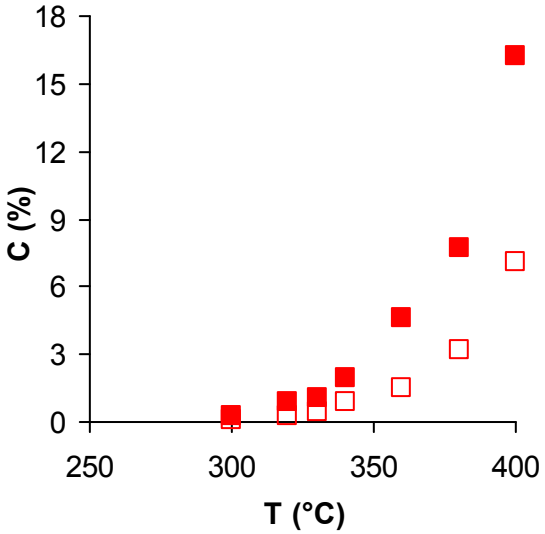

Figure A.III.7. Conversion against reaction temperature on catalyst BV46-2Pt. Hydrogenolysis, closed symbols; isomerization, open symbols

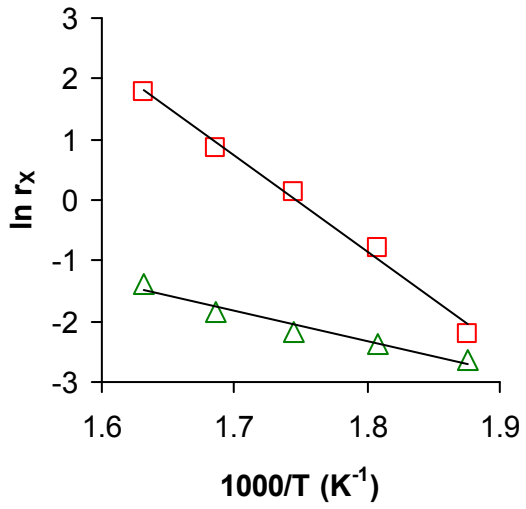

Figure A.III.8. Arrhenius plots for hydrogenolysis (□) and isomerization (△) of n-butane on catalysts CA1-2Pt

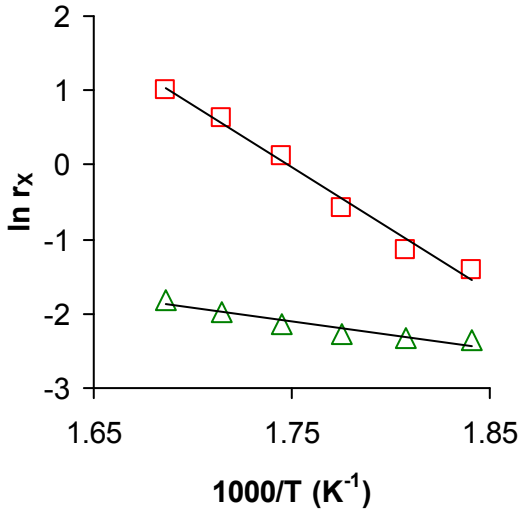

Figure A.III.9. Arrhenius plots for hydrogenolysis (□) and isomerization (△) of n-butane on catalysts CA2-2Pt

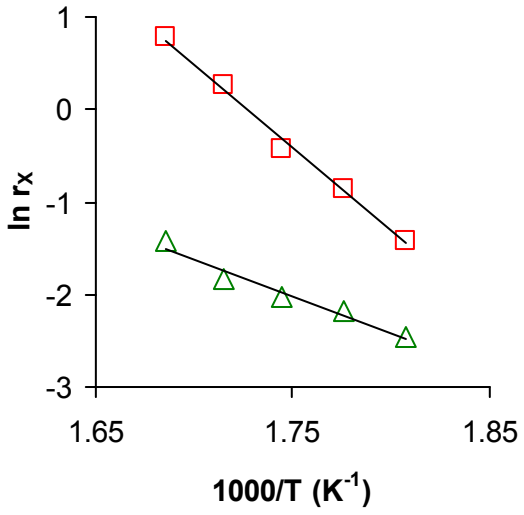

Figure A.III.10. Arrhenius plots for hydrogenolysis (□) and isomerization (△) of n-butane on catalysts CA3-2Pt

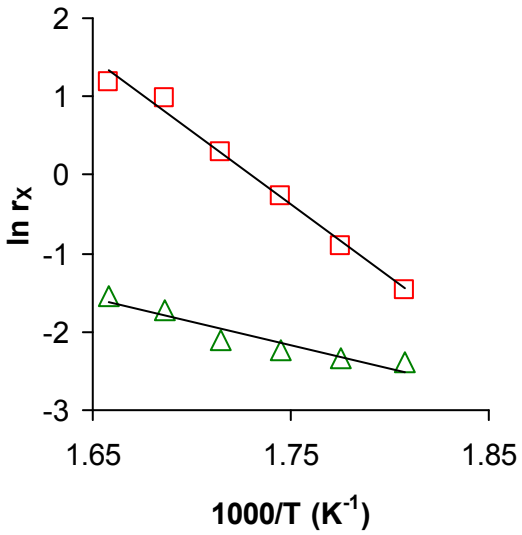

Figure A.III.11. Arrhenius plots for hydrogenolysis (□) and isomerization (△) of n-butane on catalysts P1-900-2Pt

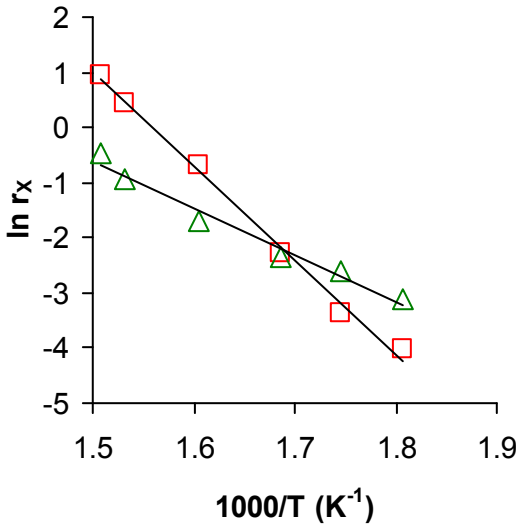

Figure A.III.12. Arrhenius plots for hydrogenolysis (□) and isomerization (△) of n-butane on catalysts P3-500-2Pt

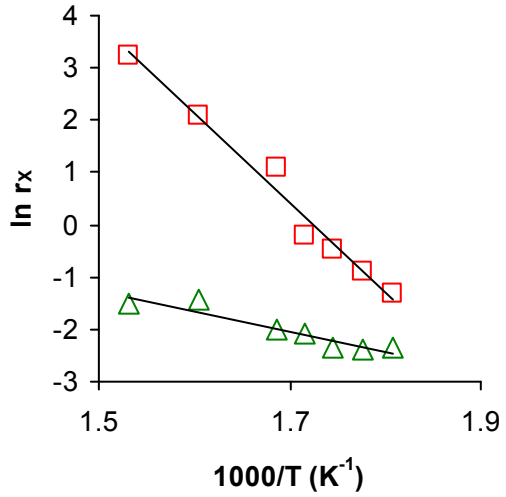

Figure A.III.13. Arrhenius plots for hydrogenolysis (□) and isomerization (△) of n-butane on catalysts P3-900-2Pt

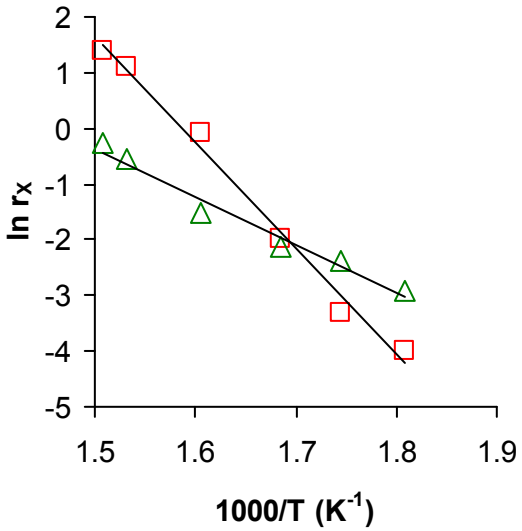

Figure A.III.14. Arrhenius plots for hydrogenolysis (□) and isomerization (△) of n-butane on catalysts POX-500-2Pt

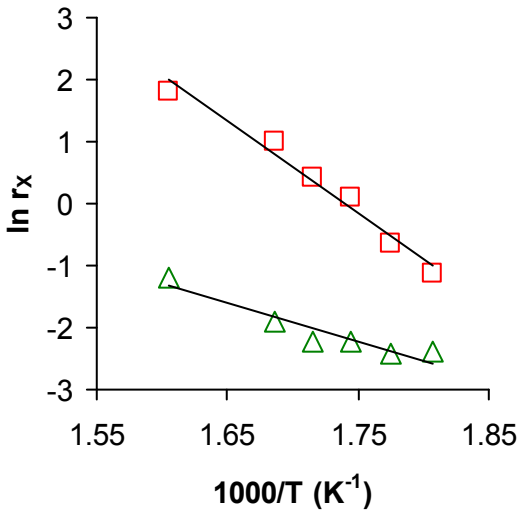

Figure A.III.15. Arrhenius plots for hydrogenolysis (□) and isomerization (△) of n-butane on catalysts POX-900-2Pt

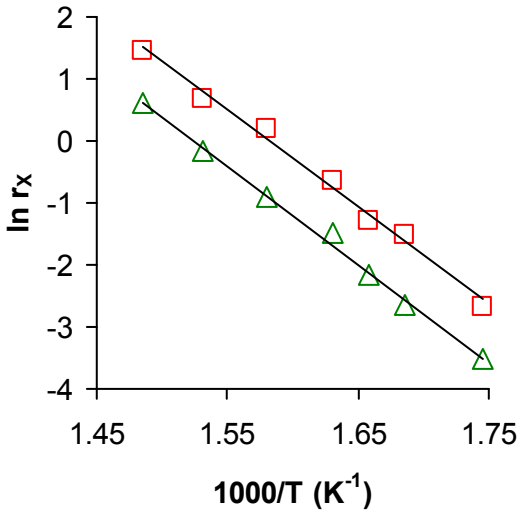

Figure A.III.16. Arrhenius plots for hydrogenolysis (□) and isomerization (△) of n-butane on catalysts BV46-2Pt